UNIVERSITY OF SZEGED

Faculty of Science and Informatics
Doctoral School of Chemistry
Department of Molecular and Analytical Chemistry

Development of advanced laser-induced breakdown spectroscopy methodologies for elemental mapping and qualitative discrimination analysis

Doctoral (Ph.D.) dissertation

Fernando Alexander Casian-Plaza

Supervisor:

Prof. Dr. Galbács Gábor

Szeged
2026

TABLE OF CONTENTS

1. INTRODUCTION

Laser-induced breakdown spectroscopy (LIBS) has developed rapidly over the past few decades and is now recognized as a versatile and powerful analytical technique for the quick analysis of solid, liquids, and gaseous samples. The widespread adoption of LIBS can largely be attributed to three key features: its relatively simple and robust instrument configuration, the ability to perform rapid analysis with little or no sample preparation, and its capacity to provide both qualitative and quantitative analytical information. Together, these features have made LIBS an increasingly important tool in both research laboratories and industrial applications.

In recent years, LIBS has increasingly entered into the fields of life sciences (biology and medical science). It is being explored as a novel tool for detecting pathogens and disease markers, for mapping the spatial distribution of elements in biological tissues, and for the qualitative classification of complex biological samples. At the same time, advances in materials science have also created a strong demand for analytical techniques that are sensitive, versatile and have high spatially resolution. LIBS fits these requirements particularly well, especially for inorganic and composite materials. Also, fundamental studies research has been aimed at exploring the processes of laser-matter interaction and signal formation, thereby improving the performance of the method.

Our Laser and Plasma Spectroscopy Research Group, led by Prof. Gábor Galbács has been active in the field for over 25 years and is continuously engaged in a number of diverse fundamental and application spectroscopy studies. I obtained my B.Sc. in Pharmaceutical Chemistry and Biology from the Autonomous University of Nayarit, Mexico, and was involved throughout my studies in research groups in the fields of pharmaceutical analysis and food chemistry. Afterwards, I worked at the Research Center for Food and Development A.C. in the research group of natural products. In 2021, I successfully applied for the Stipendium Hungaricum grant and became involved in Prof. Galbács's group while being a M.Sc. student, and later pursued the Ph.D. with a fully-funded grant from the Secretariat of Science, Humanities, Technology and Innovation (SECIHTI) from the government of Mexico.

Building on these, the work presented in this dissertation focuses on expanding LIBS in three complementary directions. First, I explored LIBS elemental mapping, including its advancement through nanoparticle-enhanced LIBS (NE-LIBS) to improve spatially resolved chemical imaging of complex samples. Second, I investigated how the use of fiber lasers can improve LIBS performance by offering enhanced flexibility and analytical sensitivity. Finally, I examined the potential of LIBS combined with machine learning approaches for the reliable detection and classification of contaminants in crops. Together, these studies contribute to the development of LIBS methodologies and broadening the range of its applications.

2. LITERATURE REVIEW

2.1 Essential aspects of LIBS

Laser-Induced Breakdown Spectroscopy (LIBS), also named laser-induced plasma spectroscopy (LIPS) can be considered as an upcoming, already fairly well-established technique of atomic emission spectroscopy in the field of analytical chemistry. Its popularity for the elemental analysis has grown enormously over the years since the beginning of this technique. Brech and Cross in 1962 employed a ruby laser to generate vapors from metallic samples which were excited using a spark source, leading to the detection of emission spark spectra [1]. The first appearance of laser-induced plasma (LIP) for spectrochemical purposes dates back to 1964, when Runge et al. employed a pulsed laser as emission source for quantitative spectrochemical analysis of nickel and chromium on steel samples [2]. It was not until the mid-1980s that such studies on the subject re-emerged due to the lowering cost of laser systems and the development of semiconductor photosensor arrays, such as the intensified charge-coupled device. These allowed for spectral measurements with high time resolution; along with a considerable reduction in the size of the instrumentation, which has eventually led to the development of portable LIBS equipments [3].

LIBS offers numerous advantages such as fast analysis speed, little to no sample preparation, multielemental trace detection (e.g. at ppm or even lower concentration levels), portable or standoff analytical capabilities, depth-resolved analysis, easy compositional examination of solids, liquids and gases, even in a non-contact manner. The amount of sample consumed by LIBS analysis is very small (ca. ng), thus the technique is often considered to be non-destructive (or micro-destructive). The spectra primarily provide information about the elemental composition of samples, but the chemical reactions occurring in the ablation plume also result in molecular bands, eventually influenced by the isotopic composition too, hence they are rich in analytical information [3-7].

The analytical performance of LIBS can of course be improved. The most common issues are matrix effects in the case of solids samples, not low enough limits of detection (LOD), and a relatively low reproducibility (10% RSD, typically). It has to be mentioned though that these are problems that other solid sampling atomic spectroscopy techniques, such as X-ray fluorescence spectroscopy (XRF) or laser ablation inductively coupled plasma mass spectrometry (LA-ICP-MS) also suffer from [8,9]. To address these limitations, numerous strategies have been developed. Among them, the most effective approaches include the double-pulse LIBS configuration, nanoparticle-enhanced LIBS (NELIBS), spatial confinement, femtosecond LIBS (fs-LIBS), and hyphenated instrumentation (e.g. Raman-LIBS) [10-13]. Considering the large amount of information in the fingerprint-like LIBS spectra, qualitative applications are also popular. Advanced statistical techniques and machine learning methods are often used for classification or identify complex sample types [14].

Because of its unique set of analytical features, LIBS is a kind of a superstar in analytical atomic spectroscopy [3]. The LIBS field is hot and produces a large number of publications every year in a wide range of application fields from biomedical and environmental analysis over industry-oriented analysis to archaeological studies or measurements under extreme conditions [15].

2.2. Fundamentals of laser-induced plasma spectroscopy

LIBS relies on the generation of a microplasma by a focused, pulsed laser beam interacting with the sample. By locally vaporizing and exciting material in gaseous, liquid, or solid form with a high-intensity laser pulse, the spectral emission produced can be used to infer the composition of the sample. The time evolution of the material ejected (ablated) from the sample has a profound effect on the analytical information obtained. When a laser pulse with an irradiance typically in the $\mathrm{GW \cdot cm^{-2}}$ range is focused on the surface of or inside a sample, it rapidly heats up the material locally, causing the ejection of a small amount of matter as solid particles, liquid droplets, and free atoms. Through interactions between the laser pulse and free electrons and atoms, a hot plasma is formed above or inside the sample. This plasma is a local assembly of atoms, ions, molecules, and free electrons that is overall electrically neutral. Charged species in the plasma act collectively, and the plasma is characterized by parameters such as electron density, degree of ionization, and temperature [5,16].

The foundation of LIBS lies in laser ablation, which serves as the initial step of the LIBS process. Laser ablation consists of three main processes: bond breaking and plasma ignition, plasma expansion and cooling, and particle ejection and condensation. The production of seed electrons is a critical step in plasma initiation. Breakdown occurs when the free electron density reaches approximately $10^{18}\ \mathrm{cm^{-3}}$, enabling strong optical absorption [3,6]. As LIBS is mostly used for the analysis of solid samples, here the main processes occurring during the plasma formation event on solids are reviewed briefly.

During plasma initiation, both the underlying mechanisms and the resulting plasma characteristics are highly dependent on the laser irradiance and the duration of the pulse. When using a nanosecond (ns) laser pulse with an irradiance below $10^{8}\ \mathrm{W \cdot cm^{-2}}$ and at a wavelength fairly well absorbed by the sample, the dominant process is thermal vaporization: the temperature of the target rises, and a clearly defined sequence of phase transitions occurs from solid to liquid, liquid to vapor, and finally from vapor to plasma. In the case of picosecond (ps) pulses with irradiance in the range of 10^{10}–$10^{13}\ \mathrm{W \cdot cm^{-2}}$, both thermal and non-thermal mechanisms such as Coulomb explosion contribute to the ablation process. For irradiances exceeding $10^{13}\ \mathrm{W \cdot cm^{-2}}$ with femtosecond (fs) pulses, Coulomb explosion becomes the primary mechanism responsible for bond breaking.

With ns laser pulses and irradiances on the order of 10^{7}–$10^{11}\ \mathrm{W \cdot cm^{-2}}$, several ablation processes may occur, which include melting, sublimation, vaporization, and ionization. The temperature at the target surface rises during the laser pulse, eventually leading to melting and vaporization of the material. The resulting vaporized material can be ionized by absorbing energy from the incoming laser radiation, giving rise to a plasma. In this regime, laser energy is predominantly absorbed via inverse Bremsstrahlung, a process in which free electrons absorb photons while colliding with heavier particles (ions and atoms). For ns pulses, the late part of the laser pulse can be absorbed by the laser-induced plasma, in a process known as plasma shielding. In contrast to this, for ps pulses the pulse duration is too brief for a significant absorption by the plasma. With fs pulses, plasma shielding is negligible, since the pulse ends before significant mass ejection or plasma formation can occur. In this case, electrons have insufficient time for repeated collisions, and energy is deposited directly into the material through nonlinear absorption and multiphoton ionization [17-19].

After the laser pulse terminates, the plasma plume continues to expand into the surrounding medium. During this expansion, the electron density and temperature of the plasma evolve dynamically. The nature of this expansion depends on several factors, including the quantity and properties of the ablated material, the amount of energy transferred to it, the laser spot size, and the characteristics of the surrounding environment (e.g. gas or liquid, pressure, etc.).

All these primary processes also affect particle formation, where nanometer-sized particles originate from the condensation of the vapor phase. Condensation begins once the vapor plume cools down to the boiling temperature of the material and ceases at the material condensation temperature. Additionally, liquid droplet ejection may occur due to steep pressure gradients within the rapidly expanding vapor plume, which exert forces on the molten surface [6]. A schematic representation of a nanosecond laser pulse interacting with a solid sample surface is shown in **Figure 1**.

The laser-induced plasma is a transient phenomenon with a typical lifetime of 0.1–100 μs, depending on experimental conditions. After several microseconds (up to a few tens of μs) the plasma plume slows down due to collisions with surrounding gas molecules, while the shockwave separates from the plasma front and continues to propagate at a velocity close to the speed of sound. Eventually, the plasma undergoes decay through radiative quenching and electron-ion recombination processes that results in the formation of high density neutral species within the post-plasma region. This decay phase concludes with the formation of clusters (dimers and trimers) through condensation and three-body collisions, followed by the thermal and concentration-driven diffusion of species into the surrounding gas.

Throughout this evolution, the plasma emits a background continuum that decays faster than the discrete emitted spectral lines of atomic and ionic species unique to each element. Thus, optimizing the delay of the spectral data acquisition, the characteristic spectral fingerprints enable elemental identification and quantification. Optimally, the goal is to generate an optically thin plasma in thermodynamic equilibrium with the same elemental composition as the sample [3,18,19].

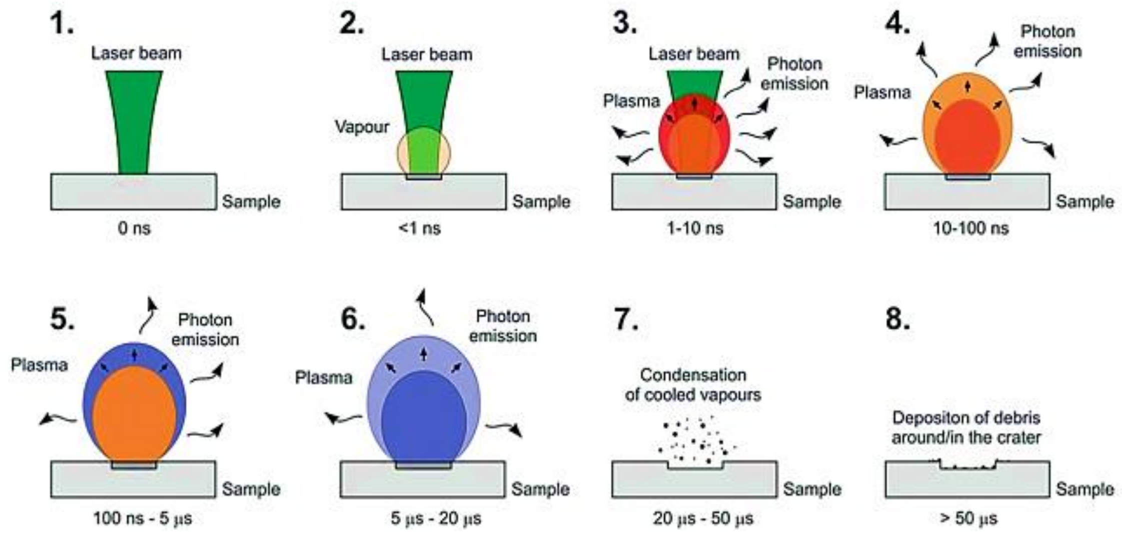

Fig. 1. Sequence of events following the strike of a focused nanosecond laser pulse on the surface of a solid sample. Times shown depict the temporal evolution after the start of irradiation of the laser pulse. Figure reproduced from reference [15].

Because of the short plasma lifetime and the dynamic nature of its emission, fast spectrometers synchronized with the laser pulse are essential for LIBS. A schematic overview of the temporal evolution of a LIBS plasma initiated by a single laser pulse is shown in **Figure 2**. After the termination of the laser pulse, the plasma plume undergoes rapid expansion and cooling over a timescale of several tens of microseconds. In the earliest stage of plasma formation, its emission is dominated by an intense continuum background, which overlaps the discrete atomic and ionic spectral lines. Therefore, LIBS measurements typically begin only after this background radiation has significantly diminished, and data collection continues for several tens of microseconds. At very short delay times (less than 1 µs), the plasma temperature and electron density are very high, often exceeding 20,000 K and $10^{19}\,\mathrm{cm}^{-3}$, respectively. Under these conditions, ion concentrations are high, and many excited states of atoms and ions are populated. As the plasma expands and cools, free electrons recombine with ions, leading to an increase in the concentration of neutral atoms, while electrons from excited states transition to lower energy levels. The cooling process continues until neutral atoms begin forming molecules, marking the effective end of the plasma phase, at which point the spectrometer collects little to no radiation [5,17,20].

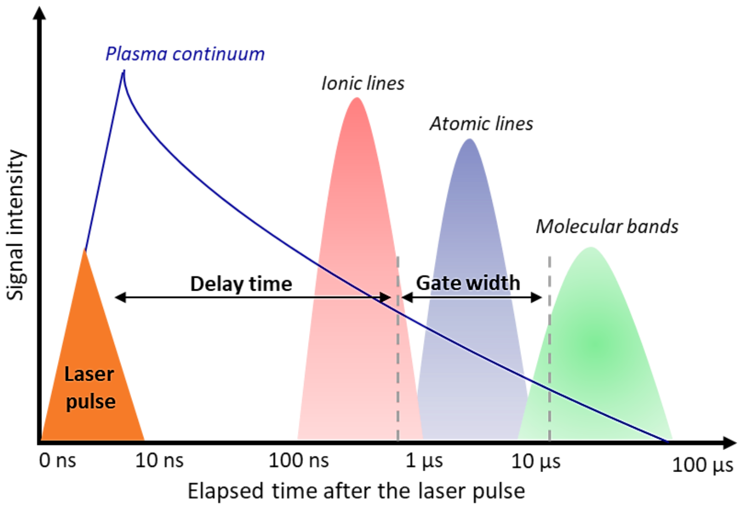

Fig. 2. A schematic of the time evolution of the light emission intensity from the continuum and species dominant in the laser induced breakdown plasma generated by a nanosecond laser pulse. The timing of the laser pulse and LIBS typical detection gating are also indicated.

However, fluctuations in pulse energies and the highly transient nature of the ablation process can introduce significant noise into the LIBS measurements. High noise levels increase LOD and LOQ, as these parameters are inversely related to noise intensity [5,9,19]. To mitigate these effects, the signal-to-noise ratio (SNR) can be enhanced either by decreasing noise (e.g., by averaging) or by boosting emission line intensity by suitable methodologies.

2.3. LIBS instrumentation

While the main instrumental components necessary for a LIBS system are clear, but a wide variety of experimental setups have been developed to date. The aim of this subsection is to describe the vital characteristics and requirements for the main components of LIBS systems. A generalized setup is illustrated schematically in **Figure 3**. The main components are:

- *A pulsed laser source.* The core of the setup in which produces the high-energy light pulses necessary to initiate plasma formation on the target surface.
- *A focusing optical system.* Using lenses/mirrors this subsystem directs and focuses the laser beam onto/into the sample.
- *A sample holder* (in an ablation chamber, if needed). This houses the sample in an inert gaseous environment, vacuum, or air.
- *A light collection system.* This is often composed of mirrors and optical fibers which collect the emission from the laser-induced plasma and transmit it to the detection system.
- *A spectrometer (detection system).* The collected light is spectrally dispersed, typically by a grating monochromator and the resulting spectrum is recorded by a detector, most commonly a charge-coupled device (CCD).

- *A gate delay generator*. This is an electronics device that synchronizes the operation of the spectrometer with that of the laser.

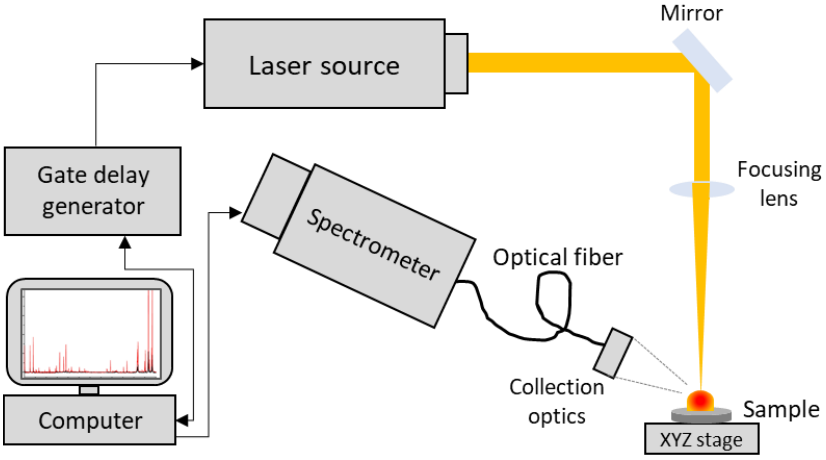

Fig. 3. A schematic of a general LIBS setup.

2.3.1. Laser source

A variety of laser types, spanning wavelengths from the infrared to the ultraviolet regions of the spectrum, have been employed in LIBS. These include solid-state lasers such as the ruby laser (693 nm, 20 ns pulse duration) and, most notably, the Nd:YAG laser (1064 nm and its harmonics, 5–10 ns), gas lasers such as the CO_2 laser (10.6 µm, ~100 ns) and the N_2 laser (337 nm, 30 ps–10 ns), as well as excimer lasers operating at 193 nm (ArF), 248 nm (KrF), and 308 nm (XeCl) with pulse durations of 10–20 ns [21].

Nanosecond pulsed solid-state Nd:YAG lasers serve as the standard workhorses in LIBS systems because they offer compactness, cost-effectiveness, high stability and durability, and can deliver high-energy, short-duration pulses with excellent beam quality. Most commonly used sources are actively Q-switched Nd:YAG lasers, which can generate powerful, short pulses (about 5-10 ns) with peak powers reaching several megawatts [21,22]. Typical specifications of Q-switched Nd:YAG lasers include pulse energies ranging from tens to hundreds of millijoules. For certain samples, the fundamental wavelength of the laser (1064 nm for Nd:YAG) may not be ideal for LIBS analysis. Therefore, it can be frequency-converted to shorter wavelengths such as 532 nm, 355 nm, and 266 nm by means of harmonic generation, employing nonlinear crystals (e.g., KDP, BBO, MgF_2) with birefringent phases [23,24]. In these Nd:YAG lasers, usually xenon flashlamps serve as the pumping source, which have lifetimes ranging from 20 to 50 million pulses, depending on the total energy delivered during discharge. However, because the emission spectrum of the Xe flashlamp overlaps only partially with the absorption spectrum of the Nd:YAG medium, only a limited portion of the absorbed pump energy is efficiently transferred to the upper laser level. Therefore, the conversion efficiency of electrical input power into laser output is less than 3%.

Recent advances in laser technology have also led to the increasing use of diode-pumped solid-state (DPSS) Nd:YAG lasers, which offer numerous advantages, including higher repetition rates, improved pulse-to-pulse stability, superior beam quality, enhanced durability, reduced size, and greater energy efficiency. These semiconductor laser diodes pump the laser crystal within a narrow spectral band in a way to maximize the pumping efficiency by minimizing energy losses, achieving an overall efficiency of 10-20%. DPSS lasers can achieve high pulse repetition rates (1 kHz or more). Although their pulse energy typically remains limited to a few millijoules, their beam quality allows them to generate very high intensities at the focal spot [21,25,26].

Another novel type of lasers is the fiber laser, which represents a great promise for LIBS, particularly in industrial and field-deployable applications. Unlike conventional solid-state lasers, fiber lasers use an optical fiber doped with rare-earth ions (commonly Yb, Er, Nd, Tm, or Pr) as the active gain medium instead of solid, rod-shaped crystal. The longer interaction length between the pump light and the doped medium in optical fibers significantly improves photon conversion efficiency compared to traditional solid-state laser systems [5] and improves heat dissipation. Structurally, a fiber laser typically consists of a doped fiber core, pump sources (semiconductor diode lasers), and fiber Bragg gratings (FBGs) acting as highly selective mirrors to form the laser resonator. Pump light is launched into the fiber either through end-pumping, where light enters directly through the fiber end face, or side-pumping, where light is coupled into the cladding using fiber couplers. These are double-clad fiber design, the pump light is guided through an inner cladding surrounding the doped core, while the laser mode itself propagates within the core [28]. Absorption of the pump light excites electrons to higher energy levels, and when a population inversion is achieved, stimulated emission occurs at a wavelength determined by the dopant species. FBGs selectively reflect light of this lasing wavelength, enabling multiple passes through the active medium and efficient amplification. This process produces a highly monochromatic, directional, and stable laser beam [18,21,27].

A particularly powerful and flexible configuration is the master oscillator power amplifier (MOPA) design. In this scheme, a low or medium power seed laser which may be a fiber laser, Q-switched solid-state laser, or a laser diode generates the initial pulse, which is then amplified by a doped fiber stage pumped by a secondary source such as a telecom-grade diode laser. This configuration supports high pulse repetition rates and scalable output power while maintaining good beam characteristics. The use of this telecom-grade pump diodes, are designed for continuous operation; which contributes to the robustness, reliability, and longevity of fiber laser systems [28-30].

Fiber lasers are highly versatile in terms of pulse duration and temporal behavior, capable of operating across a wide range; from continuous-wave (cw) output to ultrashort pulses in the fs range. Short pulses are generated using mode-locking techniques, achieving pulse durations down to ~50 fs, while Q-switching enables pulse durations in the nanosecond to microsecond range, ideal for LIBS applications. Their ability to deliver pulse energies up to the millijoule range combined with superior beam quality allows for high focal spot intensities, even if the total pulse energy is lower than that of conventional solid-state lasers.

These lasers offer several advantages such as high beam quality, compact size, robust, and low thermal load, reducing internal stresses and improving optical properties; also, maintenance-free, and do not need for precise alignment of free-space optical components. These features have driven the rapid adoption of fiber lasers in a wide range of applications, including welding, cutting, marking, telecommunications, surgery, and micromachining. However, the use of fiber lasers in LIBS spectroscopy is relatively recent, primarily because suitable fiber lasers with sufficient pulse energy for plasma generation on most solid materials continues to be an active area of research for quantitative analysis [30-32].

2.3.2. Optical system

Laser pulses in LIBS are typically focused onto the target surface using lenses or mirrors to achieve the high irradiance levels necessary for plasma generation. The simplest configuration involves a single focusing lens, most often spherical (or less commonly cylindrical), that concentrates the laser beam onto a small spot sufficiently intense to initiate a plasma. The focal length plays an important role in the focusing behavior. Short focal-length lenses (e.g. microscope objectives) are preferred when highly localized sparks or spatially resolved measurements are required, as they provide higher power densities at the focal point. However, ca. 20 mm working (focal) distance is required to keep the optics clean from ablation debris; if the ambient gas has lower than atmospheric pressure, this distance may need to be further increased. On the other hand, long focal-length lenses have the advantage that their depth of focus is larger, thus it is less important to set and keep the lens to sample distance accurately. Obviously, these lenses are used in stand-off LIBS configurations. These usually require higher pulse energies to maintain sufficient irradiance due to the larger focal volume [4,18].

Various optical materials are used for lenses, depending on the laser wavelength and the spectral region of interest. BK7 glass performs well in the visible and NIR ranges, while quartz is preferred for wavelengths below 340 nm. For IR lasers (e.g., CO_2); ZnSe, Ge, or NaCl lenses are required. To reduce reflection losses and maximize energy transfer to the sample, lenses are usually equipped with anti-reflection coatings, lowering reflectance to below 0.5%. Uncoated optics typically lose around 8% of the incident laser energy through reflections at both surfaces [5,16,22]. Reflective focusing optics, such as parabolic mirrors and Schwarzschild objectives are also often used. Reflective optics eliminate chromatic aberrations and are particularly advantageous for wide spectral-range measurements.

The light collection system in LIBS gathers the radiation emitted by the plasma and directs it to the spectral detection unit (e.g., spectrometer and detector). Depending on the experimental design, collection optics can either form an image of the plasma plume at the entrance slit of the spectrometer or simply collect and guide light via optical fibers.

Several geometric configurations are used for emission collection. Side-view (perpendicular) observation allows spatially resolved measurements by imaging specific regions of the plasma plume, providing information on emission intensity variation with distance from the target surface. Coaxial (on-axis) collection, where holed mirrors or dichroic mirrors are used, in which the collection axis coincides with the plasma expansion direction, is simpler and less sensitive to geometric misalignments. It is widely used when spatial resolution is not required. Although coaxial setups are more compact and well-suited for depth-resolved analyses, they can suffer from self-absorption effects, reducing calibration linearity. In contrast, side-view geometries generally achieve better signal linearity but may experience greater signal fluctuations due to plasma instability [33,34].

The use of fiber optics (FO) has become widespread in modern LIBS setups due to their flexibility and ability to guide light efficiently over long distances. A fused-silica optical fiber transmits light through total internal reflection, with an acceptance angle (e.g. approximately 26°). Fiber core diameters typically range from 50 μm to 1 mm. High-OH-content fibers are used for UV/VIS transmission, while low-OH fibers with less than 2 ppm water content are preferred for NIR operation due to reduced absorption losses [6,22,33,34].

Initially, FO in LIBS were used solely for collecting plasma emission, as coupling high-energy laser pulses into fibers without damage was difficult. However, advancements in high-damage-threshold fibers capable of transmitting irradiances up to 5 GW/cm^2 have enabled their use for laser pulse delivery as well. LIBS configurations now include setups using two separate fibers, one for delivering the laser pulse and another for collecting emission; or single-fiber systems that perform both functions [35,36].

2.3.3. Spectrometer

LIBS spectra are highly complex, featuring numerous emission lines that extend across a wide spectral range from the UV to the NIR region. Therefore, an optimal detection system must meet the following, demanding criteria:

- Wide spectral coverage
- High spectral resolution (better than 0.1 nm)
- High dynamic range and quantum efficiency
- Fast acquisition and synchronization ability to capture transient plasma emission at the μs timescale.

The fulfillment of these requirements is challenging and therefore a variety of spectrometer-detector combinations have been developed to balance resolution, sensitivity, and temporal response [37,38].

The Czerny–Turner optical arrangement is one of the most widely used in LIBS due to its versatility and compactness. Light passes through an entrance slit and is collimated by a concave mirror onto a single (holographic) diffraction grating. The grating disperses the light according to wavelength, and a second mirror focuses the resulting spectrum onto the detector plane [38,39]. This configuration provides moderate resolution and is often coupled with linear photosensor arrays (detector arrays) [40]. However, its spectral range is limited; achieving higher resolution typically reduces wavelength coverage. To mitigate this, multi-grating turrets or multiple detectors can be employed to extend the accessible spectrum.

In Paschen–Runge optical arrangements, a single concave grating acts as the dispersing element. The entrance slit, grating, and detectors are mounted along a Rowland circle, ensuring that each wavelength is focused onto a specific point along the circle where individual detectors (often photoelectron multipliers) are positioned. This arrangement allows for simultaneous detection of multiple spectral regions and valuable for multi-element analysis. However, these systems are generally bulky and limited in flexibility compared to modern array-based instruments [5,16].

The Echelle optical arrangement represents the most advanced and powerful configuration for LIBS applications. It uses two dispersing elements, a diffraction grating (echelle grating) and a prism; which separate the incoming light along two orthogonal directions. The echelle grating, is coarse with a high-blaze-angle diffraction grating. Due to this particular geometry, high spectral resolution is obtained by using large angles of incidence and high order of diffraction. At higher diffraction orders, the linear dispersion becomes so large that multiple consecutive orders must be utilized to cover a sufficiently wide spectral range; consequently, longer wavelengths from a diffraction order overlap with other ones causing to overlap with one another. As a result, in any given direction of the diffracted beams from the grating, radiation from multiple wavelengths, each corresponding to a different spectral order may be present, causing their spectral images to coincide on the focal plane. To resolve this overlap, a second cross-dispersing element is incorporated, typically a prism or a secondary grating positioned at a 90° angle relative to the echelle grating. This component separates the overlapping orders by dispersing them in a direction perpendicular to that of the primary grating, creating a high-resolution, two-dimensional pattern of wavelengths versus spectral orders (echellogram) [5,18,38]. Consequently, Echelle spectrometers require two-dimensional detector arrays placed at the focal plane to record this bi-dimensional dispersion. The collected emission signals are then processed and combined, aligning the rows from different orders into a continuous linear spectrum. This configuration allows simultaneous acquisition of a broad wavelength range (typically 200–1000 nm), together with its high resolution, makes it effective for analyzing alloys, well linear fitted calibration curves, improve of LODs, and suitability for measuring plasma temperature and electron density. Its wide dynamic range allows simultaneous measurement of spectral line intensities for both major and trace elements within the sample [41].

As it was alluded to above, modern LIBS spectrometers almost exclusively use photosensor arrays as they can record complete spectra with good timing accuracy. Charge-coupled devices (CCDs) are silicon-based devices composed of light-sensitive pixels that store and transfer photo-induced charges through shift registers for digitization. Free electrons produced in each pixel by incoming photons are gathered and held within the semiconductor layer located beneath that pixel. In two-dimensional arrays, at specified time intervals, the accumulated electrons are transferred sequentially from one pixel to the next within a column using a precisely timed driving voltage (the vertical shift register). At the bottom of each column, a horizontal shift register gathers one row of pixels at a time and moves the charge from each pixel to its neighbor in sequence. Finally, an amplifier at the output of the shift register converts these charge packets into a corresponding output voltage; this voltage signal is processed externally and converted into digital form [18,42,43]. Linear CCDs are commonly used in Czerny–Turner spectrometers, while two-dimensional CCDs are ideal for Echelle spectrometers [44]. CCDs provide better SNR, high spatial and spectral resolution but have limited gating capability (typically milliseconds), restricting their use in time-resolved LIBS.

Complementary Metal-Oxide–Semiconductor (CMOS) detectors have emerged as strong competitors to CCDs in LIBS instrumentation. The detector type used in CMOS sensors is the active pixel detector (APD), in which each pixel contains its own photodiode, amplifier, and readout circuitry. This design allows for non-destructive readout, random pixel addressing, and substantially faster frame rates compared to CCDs, since the charge does not need to be shifted serially across the entire array [45]. APD/CMOS detectors enable very fast gating, making them suitable for time-resolved LIBS where early plasma emission must be captured. They also support higher readout speeds, reduced power consumption, and easier integration with digital electronics.

Intensified CCDs (ICCDs) combine a CCD with an image intensifier, composed of a photocathode, a microchannel plate (MCP), and a phosphor screen. Their principle of operation relies on incoming photons enter the photocathode, where they are converted into electrons. These electrons are accelerated toward the MCP by an applied control voltage and undergo multiplication within the MCP. The MCP is composed of numerous fine glass capillaries bundled together, with their inner walls coated in a secondary electron-emitting material. As electrons travel through the channels, they collide with the walls, producing additional electrons in a cascade process similar to the PMTs. After exiting the MCP, the amplified electrons hit a phosphor screen, which reconverts them into photons. These photons are then directed to the detector sensitive surface (either a PDA or CCD) through a coupling lens or a fiber-optic taper [5,18,22]. This configuration not only offers the ability to multiply the number of the incoming photoelectrons but also a fast gating capability. Enabling high gain, and temporal evolution of plasma emission. ICCD-echelle combinations are widely used in LIBS systems, offering superior temporal and spectral resolution [46,47]. However, ICCDs are expensive, complex, and often produce lower SNR than non-intensified CCDs.

2.4. Analytical performance

LIBS has established itself as a powerful and versatile analytical tool in modern elemental analysis. Its capability for rapid, in situ, and multi-element detection, often without the need for complex sample preparation in a virtually non-destructive way since it requires only a minimum amount of material (typically ng to μg) for vaporization and atomization, making it suitable for analyzing delicate, hazardous, or valuable samples. LIBS analytical performance is typically evaluated in terms of its figures of merit used in analytical chemistry, which collectively define the reliability and applicability of LIBS in quantitative analysis. The typical LOD for the analysis of solids are in the low-ppm range, with a repeatability around 10% RSD on average. LOD values can reach below the ppb level when experimental parameters are carefully optimized or when signal-enhancement methods are employed (see the next section) [15]. LIBS is often criticized because of its poor signal repeatability; with complex or microheterogeneous materials the signal variability is indeed no excellent. Improvement in precision can be obtained through signal averaging over multiple laser shots, use of stable laser sources, and application of signal normalization methods to compensate for plasma fluctuations [3,5,15].

Achieving high accuracy in LIBS can be challenging due to matrix effects, self-absorption, and variations in plasma excitation conditions, which can alter the relationship between emission intensity and analyte concentration. Calibration strategies play a crucial role in improving accuracy; these include the use of matrix-matched standards, standard addition methods, and calibration-free LIBS (CF-LIBS) approaches. When properly calibrated, LIBS can achieve quantitative results with accuracy comparable to other atomic emission techniques, especially for solid materials [37].

Despite some intrinsic limitations, LIBS is a highly attractive analytical technique because of its speed, minimal invasiveness, and ability to analyze solid, liquid, and gaseous samples directly. Its multielemental capability and its highly collimated laser spot size, which can be focused onto a small area (300 µm or lower) creating a well-defined analytical spot for high spatial resolution analysis for elemental mapping, depth-profiling, and performing remote sensing in hazardous or inaccessible environments. The combination of these features, together with ongoing improvements in instrumentation, data processing, and calibration methodologies, continues to enhance the analytical performance of LIBS and expand its role as a reliable tool for both qualitative and quantitative elemental analysis [48,49].

2.5. Signal enhancement strategies

In order to improve the performance of LIBS, researchers have been experimenting with a number of approaches in recent years that can significantly enhance its sensitivity and precision (repeatability). In the following, some of the most relevant signal enhancements techniques mentioned in the literature and also investigated by our research group are described.

2.5.1. Double-pulse plasma generation

In contrast to conventional single-pulse LIBS, the double-pulse LIBS (DP-LIBS) technique employs two laser pulses with a controlled inter-pulse delay and a specific geometric arrangement to enhance overall spectral sensitivity. The inter-pulse delay is usually such that the event generated by the first pulse does not end by the time the second pulse arrives to the spot. The observed signal enhancement in DP-LIBS arises from several mechanisms, including improved laser-plasma coupling (through plasma reheating and extended plasma lifetime), additional sample heating and higher ablated mass, and modifications in the surrounding atmospheric conditions. The second laser pulse further elevates the plasma temperature and electron density, resulting in stronger spectral emission.

Depending on the direction and sequence of the laser beams, several geometric arrangements have been proposed to reach signal enhancement in DP-LIBS. These include various configuration for generating the two pulses. In the collinear configuration, two laser pulses travel along the same optical path and are focused on the same spot on the sample surface, separated by a controlled time delay. In contrast, orthogonal configurations involve one pulse directed perpendicularly to the sample surface and another propagating parallel to it. The orthogonal setup can operate in two distinct modes: the pre-ablation mode, where the first pulse travels parallel to the surface and focuses slightly above it to generate an air plasma that conditions the environment for the subsequent perpendicular pulse; and the orthogonal reheating mode, in which the first pulse ablates the sample, and the second, parallel pulse re-excites the resulting plasma to increase its temperature and prolong its lifetime [5,18,22].

Various other configurations have been explored, involving adjustments in beam geometry, pulse duration, laser wavelength, interpulse delay, and the relative energy of successive pulses. St-Onge et al. reported a 3- to 4-fold increase in the intensity of emission lines on an aluminum alloy, when using a DP burst instead of a SP of the same total energy by a Nd:YAG 1064 nm laser. The same author investigated DP-LIBS using different laser wavelengths was reported employing a combination of a 266 nm and 1064 nm Nd:YAG laser pulses on an aluminum target, with the same irradiance. The authors demonstrated that a sequence of UV and NIR pulses generates deeper ablation craters and produces stronger analyte signals than those achieved with a NIR–NIR pulse sequence [50].

A novel, well-developed approach technique is **multi-pulse LIBS** (MP-LIBS), that can be viewed as an extension of the DP-LIBS. In practice, MP-LIBS is only implemented using a collinear configuration with a single laser source, in which multiple consecutive pulses, at a same wavelength, duration, and energy are directed along the same optical path to enhance plasma excitation and signal intensity. Our research group has also conducted extensive studies in the area of MP-LIBS, where signal enhancement approaches by employing several laser pulses (up to 11), in the ns-range, separated by 20-40 µsec interpulses, with time-integrating detection were investigated on alloys. Resulting in significant improvement in all the analytical figures of merit with respect to DP/SP-LIBS [11,32,51,52].

2.5.2. Controlled gas atmosphere

The effect of atmospheric conditions (air, He, N_2, Ar, CO_2, etc.) on LIBS spectra generated from the sample surface increases sensitivity and the linear dynamic range on the measurement. Several advantages by performing LIBS at reduced pressures (below atmosphere) can result in enhanced spectra intensity, better spectra resolution, more ablated matter is formed and self-absorption is less, and more homogeneous craters. However, a too high or too low pressure is inadvantageous (too quick expansion leads to low plasma temperature; compression hinders plasma formation). Reduced pressure also increases resolution (less pressure broadening). The reduced pressure also influences the plasma lifetime, in which the plasma becomes less ordered with decreasing pressures and expands more towards the laser as pressure is reduced. It needs to be said that by applying a slightly reduced pressure (few mbar), the lifetime of a LIBS plasma is greater than that of a LIBS plasma created at atmospheric conditions. Also, the ambient gas quality matters because of the atomic mass, ionization energy, and heat conduction influences plasma parameters and hence LIBS signal. Usually argon is used, which increases sensitivity by a factor of ca. three [53].

2.5.3. Spatial confinement

Here, the laser-induced plasma is confined to a small size in a properly arranged cavity shape (cylinder, hemisphere, bowl-shape) made out of quartz, metal, or PTFE [54]. The enhancement is attributed to the reflection and compression of the shockwave and a more effective collection of plasma radiation due to the reflection from the chamber walls. The compressed plasma leads to an increased collision rate among the particles, resulting in an increased number of atoms in high-energy states, causing an increase in plasma temperature and density, hence an enhancement of emission intensity. The cavity size plays an important role for the enhancement, since it influences the dynamics of the plasma. Li et al., measured laser-induced Cu plasmas with a cylindrical cavity (2 mm to 10 mm) at different delay times; where an enhancement factor grew 5-fold at 11 μs delay time and a wall distance of 9 mm, at a fix pulse energy [55]. Yin et al., applied a cylindrical and bowl-shaped spatial confinement setup to minimize signal fluctuations during LIBS analysis of ambient air. They demonstrated that cylindrical confinement was effective in partially reducing signal fluctuations. However, when bowl-shaped confinement was employed, the plasma shape and position became more stable, leading to an even greater reduction in spectral fluctuations compared to the cylindrical setup [56]. A drawback of these techniques is the need for a thorough cleaning of the chamber walls between analyses, while a precise control of the gate delay and gate width are important.

Conversely, a magnetic field is used in the case of the magnetic confinement method. The magnetic field influences the movement of electrons and ions by the Lorentz force. This, slows down plasma expansion and hence reduces the size of the plasma. Consequently, the electron density and temperature of the LIP increase due to a higher collision frequency in the presence of an external magnetic field that results in the enhancement of optical emission [57]. Hao et al. achieved lower LODs for V and Mn in alloys when using ring magnets compared to both, a demagnetized magnet and no confinement. The magnetic field strength gradually increased along the magnet central axis, reaching a maximum of 4090 G. Under a ring-magnet confinement, both the electron temperature and electron density were significantly higher due to the combined effects of spatial and magnetic confinement.

2.5.4. Spark assistance

This low-cost method integrates a high-voltage fast discharge circuit with a conventional LIBS setup. Spark-assisted LIBS (SA-LIBS) can be performed under ambient conditions and its simplest form only requires a simple capacitor and a high-voltage power source. Additionally, it causes less damage to the sample surface because the laser pulse energy can be significantly reduced. As the applied voltage increases, the energy deposited in the spark discharge also rises, leading to an enhancement in signal intensity [58].

2.5.5. Nanoparticle enhancement

Metal nanoparticles (NPs), particularly those composed of gold and silver, have received significant attention due to their exceptional optical, electronic, and chemical properties; since the spatial confinement of their electrons determines the physical and chemical characteristics of NPs [59]. When light of a suitable wavelength interacts with a metallic NP, the oscillating electric field of the electromagnetic wave displaces the conduction electrons relative to the positively charged atomic lattice. This displacement creates regions of opposite charge on either side of the NP, generating an electrostatic restoring Coulomb force that pulls the electrons back toward equilibrium. As a result, the electrons oscillate collectively at a characteristic frequency. When the frequency of the incident light matches this natural resonance frequency, it will produce large oscillations of all of the free electrons in the NP, hence a strong resonance occurs, known as localized surface plasmon resonance (LSPR), which gives rise to distinctive optical features such as intense absorption and scattering bands in the visible and near-infrared regions [60-62]. The resonance frequency of these oscillations is determined by several factors, including electron density, particle size, shape, composition, interparticle distance, and the dielectric constant of the surrounding medium. This spatial confinement of electrons is what gives NPs their unique optical behavior.

For small NPs (smaller than or equal to the wavelength of the incident photon), the oscillation is confined within the entire NP volume. As a large number of electrons oscillate collectively within the NP, they generate strong electric fields in its immediate surroundings. These fields themselves interact with the electrons, amplifying the oscillations. This coupled excitation, between the oscillating electron cloud inside the particle and the oscillating electromagnetic field around it is known as a localized surface plasmon (LSP), producing intense, localize electric fields (see **Figure 4**). These fields can be amplified by several orders of magnitude higher than the incident field; especially at sharp edges, tips, or interparticle junctions, where the local geometry enhances the confinement of the electric field [63-65]. In this context, two electromagnetic fields are generated, one within the NPs (from the collective oscillation of electrons) and another, stronger field, surrounding them externally (the surface charges creates a dipole field).

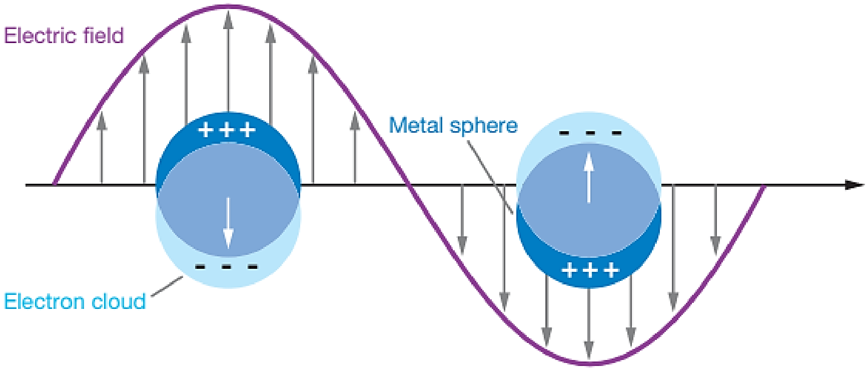

Fig. 4. Illustration showing the localized plasmon oscillations that occur in metallic NPs when they are exposed to incident light waves. Figure reproduced from reference [61].

These enhancement effects form the basis of surface-enhanced Raman spectroscopy (SERS), in which Raman signals are amplified by many orders of magnitude [66], or in surface-enhanced fluorescence spectroscopy (SEFS), for detecting bioactive molecules in the biological and environmental fields [67]. LIBS in not an exception, fundamental and applied studies have been ongoing for more than a decade with a method called nanoparticle-enhanced LIBS (NE-LIBS).

In NE-LIBS, a small droplet of a nanodispersion is deposited on the sample surface, covering an area where the laser spot will be focused. After the solvent evaporated, the NPs remain on the surface, altering its characteristics and significantly improving the absorption of laser energy. As a result, for metallic samples, the emission signal can increase as much as by two orders of magnitude [68].

Nevertheless, after the deposition of a NP colloidal solution onto the sample surface, NPs can organize themselves in many different ways. Some remain isolated, while others gather closely together to form small or large clusters. These diverse arrangements are unevenly distributed across the dried droplet, producing a coffee-ring effect (CRE). The characteristics of this effect depend on the hydrophobicity of the solution and the contact angle between the liquid and the substrate. The result is a heterogenous, mostly ring-like deposition. This complexity makes it challenging to accurately describe the laser-nanoparticle interactions during NE-LIBS [17]. Therefore, to understand and explain the observed sensitivity enhancement in NE-LIBS, it is essential to account for the different NP arrangements and their resulting plasmonic interactions.

As previously mentioned, LSPs are formed from the coherent oscillations of conduction electrons on the surface of a metallic NP after an oscillating electric field from the incident light (laser). However, NE-LIBS interacts with many NP assemblies, by coupling to each other. Coupling between LSPs takes place when NPs are brought sufficiently close so that their near electromagnetic fields overlap at the particle surfaces. This interaction produces new plasmonic modes with shifted resonance frequencies and leads to an even stronger enhancement of the surrounding electromagnetic field. When two NPs are separated by only a small gap (dimer), their near-field coupling minimizes far-field scattering and concentrates the electromagnetic energy within the narrow space between them. This strong coupling generates a large charge dipole across the gap, creating a localized region where the electric field intensity greatly exceeds the sum of the individual fields produced by isolated nanoparticles. This highly confined and amplified electromagnetic region is called a plasmonic “hot spot” [69,70]. An example showing the spatial distribution of the enhanced field in the gap between adjacent nanoparticles is shown in **Figure 5-A**. Where for a single NP the maximum electric field enhancement is located at the poles of the NP while for a dimer the maximum field enhancement is in the region in between the NPs.

Several authors have reported that the strength of the field enhancement in the hot spot is determined by the interparticle distance of the NPs to each other (see **Figure 5-B**) [70-74]. This indicates that the electromagnetic field enhancement becomes stronger as the charge density increases and decreases proportionally with the cube of the interparticle distance. Therefore, the degree of emission signal enhancement is highly influenced by the surface concentration of NPs, since it is directly dependent to the average interparticle distance of NPs deposited.

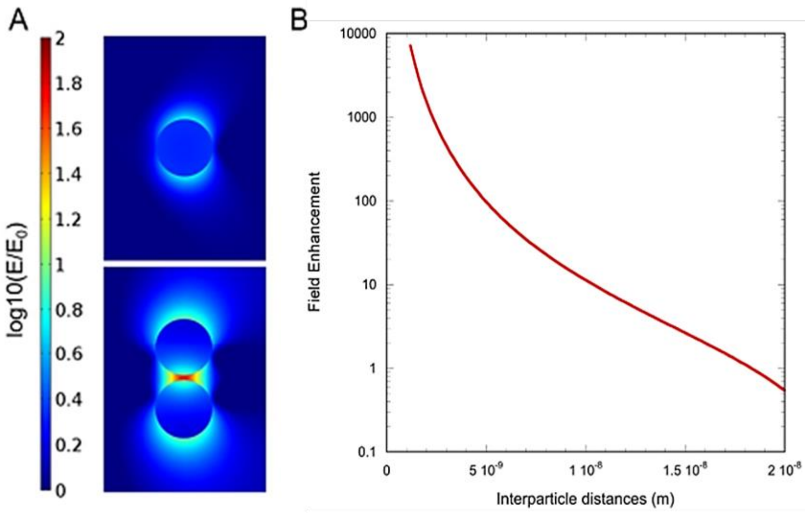

Fig. 5. A) Plots of the relative electric field enhancement of a 25 nm gold single NP and dimer, where |*E*| is the amplitude of the calculated electric field and E_0 is the amplitude of the incident electric field, polarized along the long axis of the nanostructure with propagation from the bottom towards the top. The area of strong enhancement (red zone) is called a hotspot [69]. B) NELIBS signal enhancement as a function of interparticle distance with 10 nm spherical NPs deposited on a titanium sample. Figure reproduced from reference [72].

Now we know that the NP concentration must be optimized for NE-LIBS in order to have an optimal interparticle distance. The control of NP surface concentration plays a critical role. De Giacomo et al, [75,76] studied the role of NP concentration with colloidal solutions by droplet deposition employing different surface concentrations on the sample and reporting the emission enhancement as function of surface concentration of NPs (**Figure 6**). It is shown that, the enhancement increases with NP concentration up to an optimal point, where the interparticle distance of the NPs allows for the most effective plasmonic coupling. Within this concentration range, maximum enhancement is maintained, indicating that once the optimal NP concentration is reached, further decreasing interparticle distances no longer improves the signal. Therefore, as the concentration continues to rise, NPs become too close to one another, causing the field enhancement in the hot spots to drop sharply due to electron tunneling effects. In addition, a high NP coverage can shield the sample surface from the laser beam, further reducing the signal. Hence, at higher NP surface concentrations, a significant decline in enhancement could happened. However, this trend can be applied for different NP sizes, which also the interparticle distance influence on the NP size [66,68,77], therefore, NPs of different sizes can achieve a maximum enhancement at different surface concentrations.

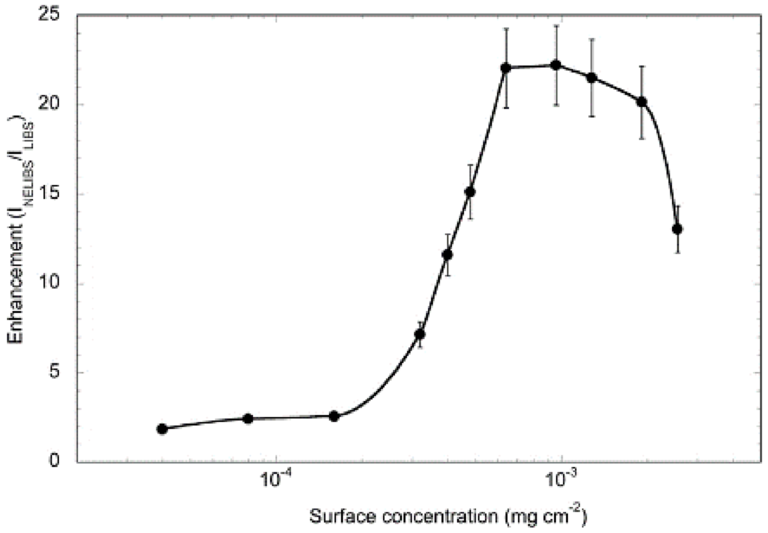

Fig. 6. NELIBS enhancement with respect to LIBS on titanium sample with 20 nm Ag NPs, illustrating the emission enhancement as a function of the NP surface concentration. Figure reproduced from reference [76].

It is also important to consider the effect of NPs on the sample properties during NE-LIBS. In a normal scenario, during LIB, plasma formation begins once the laser irradiance exceeds a critical value known as the breakdown threshold, which varies according to the physical and chemical properties of the sample material. To initiate this process, a sufficient number of free (seed) electrons must be generated to trigger optical breakdown and plasma induction. However, most of the laser energy in this interaction is consumed in vaporizing and ionizing the sample. In solids, the dominant mechanism responsible for producing these electrons is multiphoton ionization, where the sample simultaneously absorbs multiple photons from the laser pulse. The combined energy of these photons becomes sufficient to overcome the binding energy that holds electrons inside the sample or the ionization energy of its atoms, leading to the ejection of electrons [5].

On the other hand, the presence of NPs on the sample surface after laser irradiation, the electromagnetic field of the incoming radiation gets amplified due to the enhancement the LSPs induce. As a result, the laser-sample interaction is no longer direct; instead, it is primarily mediated by the NPs. Since metallic NP have a much lower breakdown threshold than bulk materials, they act as highly efficient electron sources and localized centers of energy absorption. Their presence increases the effective laser-matter interaction area, facilitating the generation of seed electrons, lowering the breakdown threshold. These effects create multiple plasma ignition points, lowering the overall energy required for ablation and leading to more efficient plasma formation and signal enhancement [68,71,74,78].

Nevertheless, for metallic samples, LSPs can also interact with the surface electrons of the metal, generating additional hot spots near the sample surface. Therefore, the enhancement mechanism differs for metallic and dielectric samples [68,72,75,78]. For metallic samples, the dominant mechanism for generating free electrons is field emission, rather than multiphoton ionization; the intense local field enhancement within the hot spots facilitates the instantaneous ejection of electrons even before the NPs are fully ablated by the laser pulse. These hot spots act as multiple plasma ignition centers across the laser-irradiated area, greatly reducing the breakdown threshold. In the case for dielectric samples (non-conducting), field emission does not occur, since the electrons generated by the NPs stay confined to the area surrounding each particle, leaving the sample bulk unaffected. As a result, ablation primarily targets the NPs themselves, occurring mainly at their contact points with the sample surface. This type of ablation happens because NPs have low thermal conductivity and, therefore, a much lower breakdown threshold compared to the bulk material.

NE-LIBS has gained significant attention in analytical chemistry due to its ability to enhance the sensitivity and overall analytical performance compared to conventional LIBS. With a minimal sample preparation, this technique has been effectively applied to trace elemental analysis of metals, alloys and biological materials; but mainly for localize analysis. It has shown remarkable potential for detecting trace (sub-ppm level) elements in alloys, lowering the LODs, with reliable calibration curves [68]. NE-LIBS can be applied for the elemental analysis of microdrops of dried solutions, enabling to quantify Pb at the ppb level, reaching absolute LODs in the picogram range [79]. It also has the ability to improve the detection of organophosphate and heavy metal residues, and macroelements on fruits and vegetables comparing it to LIBS, and also by obtaining enhanced-elemental maps of the distribution of the analytes in leaves [80,81]. In addition, Pálasti et al. designed an improved SERS substrate that enabled quantitative NE-LIBS analysis of liquid samples [66]. Also, NE-LIBS has been employed for analysis of glass and gemstone, which was possible to perform it without sample damage from the laser and preserving the sample [82].

2.6. Chemometrics

Machine learning is the study of techniques for the automated extraction of information from raw data. However, the study of methods (techniques) for extracting information from chemical data, design optimal experiments and enhance understanding of chemical systems is known as chemometrics [83-85].

The rapid development of machine-learning and the growing availability of advanced chemometric methods have greatly expanded the analytical potential of LIBS data processing. However, improper application of these methods can lead to misleading results, such as achieving high classification accuracy in the absence of real chemical or elemental differences in the samples or over-fitted models; obtaining improper classification results [37,86,86]. Also, sophisticated program algorithms may produce seemingly valid classifications that are, in fact, driven by irrelevant variables such as background noise or contamination rather than genuine compositional differences.

2.6.1. Data pre-processing methods

An important point of consideration is the use of spectral pre-processing methods prior to chemometric analysis; such as baseline correction, noise filtering, normalization, overlapping peak resolution and feature selection. Due to the fact that using the whole LIBS spectrum without adequate pre-processing; can result in overfitted models (e.g. capturing noise rather than meaningful signals) or can also lead to issues associated with high dimensionality of classification models [86-88]. A brief description of these data pre-processing approaches is provided below.

2.6.1.1. Spectral baseline correction

This process the plasma spectral background while preserving the essential analytical information. Several studies have suggested various methods for performing baseline correction. Gornushkin et al. [89] developed a polynomial algorithm, in which the spectrum is divided into groups, and local minima are identified within each group, along with a specified number of minor minima corresponding to pixels with the lowest intensities. The polynomial curve derived from both major and minor minima is then used to model the continuum background. Another method is wavelet transform, which uses a mathematical transformation that enables signal analysis in the frequency domain. The method involves convolving the signal with a specific function known as the mother wavelet, allowing the signal to be decomposed into its fast, medium, and slow varying components [87]. The Savitzky-Golay smoother is one of the most popular algorithms based on least squares, where a low order polynomial is fitted to a selected data interval, and the fitted value at the center of that interval is retained. The interval is then shifted one sample to the right, and the process is repeated until all the required smoothed values are obtained. Another baseline estimation method is asymmetric least squares (ALS), which relies on a penalty factor and a smoothing factor. It automatically finds a smooth baseline under the spectral peaks by penalizing deviations differently above and below a fitted line [90]. Simple polynomial fitting is another quick and effective way to estimate the background; it fits a low order polynomial curve to the baseline and subtracting it, but with low precision.

2.6.1.2. Noise filtering

Regarding the noise, LIBS spectra can include dark noise and background noise. Noise can be reduced by smoothing. The most common noise filtering methods are the Savitzky-Golay and fast Fourier transform, which uses a mathematical filtering that decomposes a spectral signal into its frequency components, removing unwanted high-frequency noise.

2.6.1.3. Overlapping peak resolution

This method is applied when the spectra exhibit spectral interferences. To overcome overlapping peaks (spectral lines), a curve fitting method can be applied, which separates overlapping spectral peaks into individual components using mathematical functions optimized through the Levenberg-Marquardt algorithm. Among the various models available, the Lorentzian and Voigt functions are the most commonly applied for peak deconvolution [87].

2.6.1.4. Data normalization

This method targets varying measurement conditions, such reducing signal fluctuations. It consists in a mathematical transformation of the data into a standardized form (divided by a factor related to a parameter). There are several normalization methods [9,91-93], but the most common ones applied in LIBS are the following:

- *Normalization to the background.* the intensity of interest emission line is divided by the background signal measured near that line; taken either from the intensity at a single wavelength or from the average intensity within a chosen spectral range.
- *Normalization to the total area* (total emission intensity). For each spectrum, the intensity of the analyte emission line is normalized by dividing it by the total integrated area of the spectrum across the entire wavelength range.
- *Normalization to an internal standard.* In this case the internal standard lines should be homologous to the analyte line originating from the same ionization state and elements with similar ionization energies to compensate for plasma variations. Their upper energy levels should be comparable, both lines must fall within the same spectral window, and their intensity ratio should be close to one to avoid detector saturation.
- *Normalization to the standard normal variate (SNV):* Is one of the most used approaches in LIBS to correct for scattering effects and intensity variations. It standardizes each spectrum by first subtracting the mean intensity of the spectrum (mean-centering), and then dividing by the standard deviation of the original spectrum (scaling). But also they can be used separated; it transforms each spectrum to have a mean $\mu=0$, and a standard deviation $\sigma=1$ [94-96]. When applied both functions are often named as autoscaling or standardization. However, this method can totally change the intensity relationship within the spectrum, thus it is important to carefully choose the most suitable scaling method, if any is to be applied.

2.6.1.5. Feature extraction

The aim of feature selection is to transform the high-dimensional spectral data into a reduced set of variables that makes the classification or regression task more manageable [83]. This process reduces data dimensionality by identifying and retaining only the most informative features, which are then used to build a model. The most used feature selection method is principal component analysis, for low-dimensional reduction of variables. It enables a condensation of meaningful spectral information into a smaller number of variables [97]. Another novel method proposed by Lohninger and Ofner [98] is the use of spectral descriptors, which define and extract specific information. Their usage addresses the dimensionality reduction and enhances the structure of the information within the data space, by decreasing the size of the space and transforming it so that only chemical information is encoded. In LIBS, they typically consist of spectral intensities or integrated spectral ranges that account for baseline variations. Other various feature selection techniques have been applied in LIBS, such as successive projection algorithm (SPA), stepwise selection (SW), analysis of variance (ANOVA), and PLS regression model [87].

2.6.2. Fundamental concepts of chemometrics

Chemometrics can analyze and interpret datasets where each object has multiple variables. A multivariate dataset represents objects along their features. An object can be a sample, a spectrum, or a chemical structure. An object is defined by a set of numerical features. A feature is a numerical variable that quantify specific properties of the objects, such as concentrations or intensities of spectral lines [94,95]. The data can be represented as a $n \times p$ matrix X, where each of the n rows corresponds to an object and each of the p columns corresponds to a feature. Therefore, each feature represents a coordinate, so every object can be visualized as a point within a p-dimensional feature space (**Figure 7**). The distance between points (objects) serves as an indicator of similarity of the objects. Hence, based on these distances, groups of similar objects (clusters) and unusual data points (outliers) can be identified.

There are different data analysis methods applied in chemometrics for multivariate data analysis, which can be classified into two groups: *unsupervised* (exploratory/clustering) where only an X-matrix is available and does not require the information about objects (class or sample names). The aim is to explore the dataset or to identify clusters to get an overview of the dataset. Some of the main tools are: Principal component analysis (PCA), k-means clustering, and hierarchical cluster analysis (HCA). The other method is *supervised*, where additionally to the main data set X, a y-vector (property) may be known for each object that defines the class membership of the objects, this can be a type of class or concentration (**Figure 7**). Supervised methods can be sub-divided in *calibration*, which establish a numerical relationship between x-variables (spectrum) and one or more dependent y-variables (e.g. concentration); the output is a regression model for prediction. Common techniques are multiple linear regression (MLR), principal component regression (PCR), partial least-squares (PLS) regression, and supported vector machine (SVM) regression. The other sub-division of supervised methods is *classification*, also a y-vector is given to the matrix-X, which determines which category or class a sample belongs to, based on its features. Typical methods are linear discriminant analysis (LDA), PLS-DA, soft independent modelling of class analogies (SIMCA), k-nearest neighbor (kNN), random forest (RF), and artificial neural network (ANN) [17,88,94-96,99].

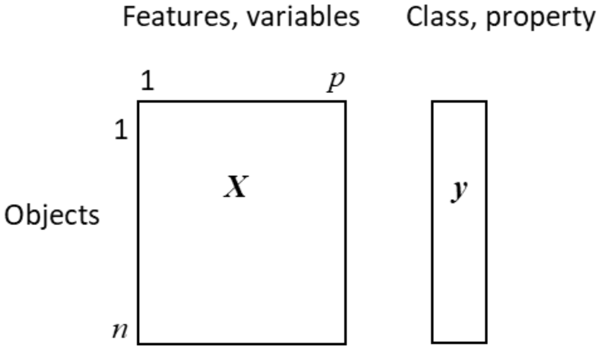

Fig. 7. n points (objects) in a p-dimensional (feature) space - matrix X and a property vector-y. A property may be a concentration or class membership of the objects.

Supervised methods employ label training data in an iterative manner to learn patterns and predict outcomes for new unseen data. The data is divided into a training set, to construct the chemometric model, which represents the unknown samples to be analyzed. It consists of distinct sample classes, each encompassing the expected spectral variations, such as differences in sample type or concentration range. And also a validation (testing) set, which includes data that were not part of the training set. These samples are treated as unknowns to evaluate the model performance. Ideally, the spectra in the validation set should come from samples entirely separate from those used for training. The final prediction results are presented in a confusion matrix, where the diagonal entries indicate the correct classification rates [94,95]. While the exact steps for building a chemometric model vary depending on the chosen method and application, the following flowchart outlines (**Figure 8**) the general stages of model development. The most common chemometric methods will be described below.

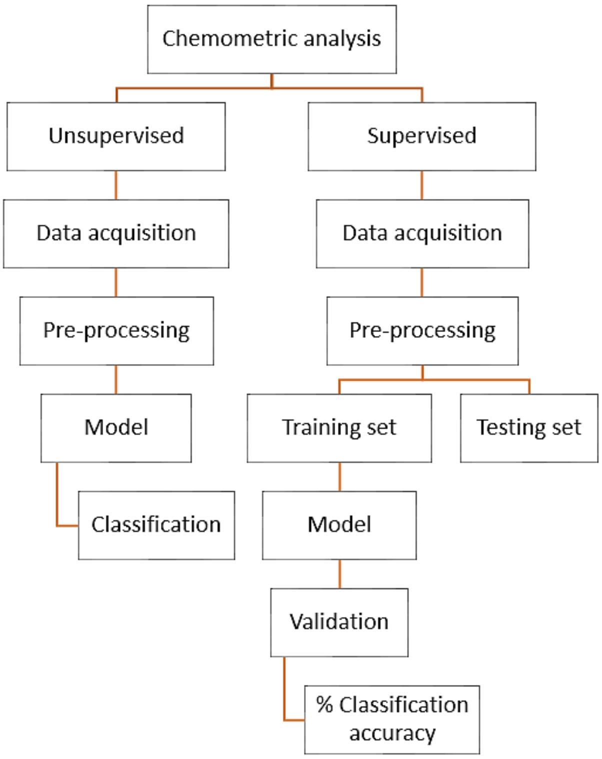

Fig. 8. Procedures involved in the development of chemometric methods. Figure adapted from reference [17].

2.6.3. Principal component analysis (PCA)

PCA is the number one method in multivariate data analysis. Is an unsupervised exploratory method for data visualization, detection of outliers, selection of variables, and data compression (dimension reduction). It simplifies complex datasets by transforming a large number of correlated variables into a smaller set of uncorrelated variables called principal components (PCs). Each PC represents a direction in which the data vary the most, with the first component capturing the greatest variance, the second capturing the next most variance while being orthogonal to the first, and so on. This transformation reduces the dimensionality of the data while retaining most of its relevant information, making it easier to visualize and interpret underlying patterns [94-97]. In analytical chemistry and LIBS applications, PCA is particularly useful for handling high-dimensional spectral data, where it helps identify similarities, groupings, or trends among samples. The resulting PCA output consists of scores, which show the position of each sample in a new coordinate system, and loadings, which indicate the contribution of each original variable (e.g., wavelength intensity) to the components.

2.6.4. Linear discriminant analysis (LDA)

LDA classification distinguishes between two or more predefined groups or classes based on their measured features. It uses class information to find directions that best separate the classes. The main concept is to project high-dimensional data samples onto a discriminant space that both reduces dimensionality and enhances class separability. In this new space, the projected samples are positioned to maximize the distance between different classes while minimizing the variation within each class, ensuring the best possible distinction among them. LDA is widely used to classify materials, such as identifying types of alloy, rock, or biological samples based on spectral data [87,94,95].

2.6.5. Partial least squares-discriminant analysis (PLS-DA)

PLS-DA is a classification method that integrates dimensionality reduction from PLS regression and linear discrimination (DA) into one algorithm, making it particularly effective for analyzing high-dimensional spectral data. Unlike PCA, which focuses only on variance, PLS identifies directions in the data that maximize the covariance between spectral variables and class labels. This process reduces the original dataset to a smaller number of latent variables (LVs) or factors that capture the most relevant spectral variation for class separation. The DA component then establishes a linear boundary in this reduced space to classify new samples. The performance of a PLS-DA model depends on the number of LVs chosen, too few may result in loss of critical information, while too many can lead to overfitting. Selecting the optimal number of LVs for a given classification task is typically done through cross-validation [87,94,95]. PLS-DA is a supervised discriminant analysis technique used to develop classification or quantitative prediction models.

2.6.6. Classification tree (CT)

CT is a supervised algorithm used to assign samples to predefined categories based on their measured features. It works by recursively splitting the dataset into smaller, more homogeneous groups according to specific decision rules derived from the input variables. At each node, the algorithm selects the feature and threshold that best separate the data into distinct classes, using statistical criteria such as Gini impurity, entropy, or information gain. The resulting model forms a tree-like structure where internal nodes represent decisions based on feature values, branches indicate possible outcomes, and leaf nodes correspond to final class predictions. CTs are easy to interpret and visualize, can handle nonlinear relationships, and require minimal data preprocessing. However, they can be prone to overfitting and may not generalize well to unseen data, which is why ensemble methods like RF are often used to improve stability [94].

2.6.7. Random forest (RF)

RF is a non-linear supervised classifier, it operates on the principle of ensemble learning, where a large number of decision trees are constructed, and their results are combined to produce a more accurate and reliable prediction. Each tree is trained on a randomly selected subset of the data (a process known as bagging) and considers only a random subset of features at each split, which helps reduce overfitting and increases model robustness. In classification problems, the final output is determined by majority voting among all trees, while in regression tasks, it is obtained by averaging their predictions. RF performs well with large, complex, and high-dimensional datasets, and can also provide information on feature importance, indicating which variables contribute most to the prediction [94,100]. The key parameters of RF are the number of trees in the ensemble and the number of features evaluated at each node split. Increasing the number of trees generally enhances performance, but this improvement tends to level off beyond a certain point, usually around 70 to 100 trees.

3. OBJECTIVES

The plan for my research activities is based on former results of our research group and addresses key analytical challenges in modern LIBS, such as improving sensitivity, enabling reliable qualitative discrimination and expanding laser source options. Guided by these challenges, the following objectives were defined for my work:

1. Development and optimization of a sample preparation method and measurement conditions for the reliable use of nanoparticle signal enhancement in LIBS mapping

2. Explore the potential of LIBS elemental mapping to quantitatively characterize nanoparticle distributions in polymer thin film nanocomposites.

3. Investigation of the applicability of fiber laser sources with tunable pulse shapes and high repetition rates to the improvement of LIBS analytical performance.

4. Assessment of the performance of machine learning evaluation of LIBS spectral data to solve qualitative discrimination analytical tasks relevant to the industry (e.g. identification of chemical contaminants on crops).

4. INSTRUMENTATION, MATERIALS AND METHODS

This chapter provides a general, brief overview of the instrumentation, materials and methods I used during my research. Further details on specific conditions and methods used to study particular aspects will be introduced at the beginning of each corresponding section discussing the results of the research.

4.1. Instrumentation

For most LIBS experiments, a commercial J200 LIBS/LA tandem system (Applied Spectra, USA) was used. This is equipped with a Nd:YAG Ultra 100 laser (Quantel-Lumibird, France), operating at 266 nm via fourth harmonic generation, with a 6 ns pulse duration and a repetition rate up to 20 Hz, with an adjustable pulse energy up to 20 mJ by mean of an optical attenuator unit. The laser beam can be focused onto the sample surface to a directly adjustable spot size between 40 to 220 µm in diameter. Aiming and documentation is helped by dual CMOS cameras, for high magnification and wide-field viewing. The sample can be moved via a motorized XY-stage with a 0.2 µm resolution and a Z-stage with a 0.1 µm resolution. The J200 system allows a flexible control of laser ablation sampling pattern via grid generation, line scanning or random point generation. The sample chamber contains gas mass flow controllers for Ar and He gas, that can be used to purge the chamber or as a direct carrier flow for bringing the ablated material into the ICP-MS if needed. In this LIBS system, the spectra are recorded by a 6-channel CCD broadband spectrometer with a spectral window of 185-1050 nm and a resolution of 0.07 nm. An integrated pulse delay generator allows for gate delay adjustment in the 50 nsec to 1 msec range. The system is fully integrated and controlled by Applied Spectra's Axiom LA 2.4 software and spectral data processing is done by the ClarityNeXt 1.0 data analysis software package provided by the manufacturer. Elemental maps recorded were evaluated by the ImageLab 3.20 (Epina GmbH, Austria) software.

In LIBS experiments performed at 532 nm and 1064 nm laser wavelengths, a stand-alone setup was employed, which included another Nd:YAG Ultra 100 Quantel laser source, but this unit is equipped with a frequency upconversion module. The laser light is focused on the sample by using a N-BK7 plano-convex quartz lens (f= 50 mm) and the plasma emission is collected at a 45° angle via a NA-matched quartz focusing lens. In experiments which required 532 nm or 1064 nm, or high-time resolution, an external spectrometer was used for the detection of LIBS emission. In such cases, we used a 400 µm core diameter optical fiber to connect the SMA905 fiber optic output ports of the LIBS setups to the 40 µm entrance slit of an Echelle spectrometer Aryelle 200 (LTB, Germany). This spectrometer is equipped with a gated ICCD detector-camera (iStar DH334T-18F-04, Andor Technology, Ireland), with a spectral range of 220-629 nm in the UV-NIR range and a spectral resolving power above 9000 and a resolution of 0.007 nm.

In experiments involving a fiber laser, a compact Trupulse Nano 5020 fiber laser (Trumpf, Germany) served as the laser source, with a maximum average output power of 200 W. It operates at a wavelength of 1062 nm and features 48 built-in temporal pulse profiles (waveforms), enabled by GTWave and PulseTune technology. These waveforms allow for adjustable pulse energies ranging from 0.35 to 4.96 mJ and pulse durations between 8 ns to 2000 ns. The system can reach pulse repetition rates of up to 4 MHz. Pulse temporal profiles were measured using a fast photodiode (DET10A, Thorlabs, USA) in combination with a digital oscilloscope (DS1102E, Rigol, China), detecting laser light reflected from a diffuser. Pulse energies were measured using a laser power meter (Gentec-EO, Canada). The laser output is collimated to a 10 mm diameter beam using the collimator head provided by the manufacturer. The beam exhibited multimode quality, with M^2 value around 4. The laser head was mounted vertically, and the beam was directed perpendicularly onto the sample surface using a 100 mm focal length plano-convex fused-silica lens (LA4380, Thorlabs, USA). In all standalone LIBS setups, a digital delay generator (TG5011, AIM-TTI, UK) was used to synchronize the spectrometer with the laser output.

Spray coating experiments were performed using a gravity-fed spray gun (200 µm nozzle, DU-30 K, Aircraft, South Africa) and 3 bar argon nebulization. Working distance was fixed at 25 cm.

Spark discharge-based NP deposition was performed using a custom-built system with a DN-160 stainless-steel vacuum chamber (KF-40 ports). Two horizontally aligned cylindrical electrodes were set 2.0 mm apart. Generated particles exited the chamber through a top port. Argon carrier gas was fed through a 2.85 mm inner diameter injector positioned midway between the electrodes and 4.25 mm from their common axis. The flow rate was 5.0 $L \cdot min^{-1}$, controlled by a mass flow controller (GFC16, Aalborg Inc., USA). Particle generation was performed at atmospheric pressure monitored by a pressure gauge (VD81, Pfeiffer Vacuum GmbH/Thyracont Vacuum Instruments GmbH). Spark discharges were produced with an 8 nF capacitor (450PM980, General Atomics, USA) charged by a high-voltage power supply (HCK 800–12500, FuG GmbH, Germany), generating a bipolar oscillatory discharge at 100 Hz. The aerosol passed through a tube furnace at 900°C (Carbolite Gero GmbH, Germany) for nano-aggregate compaction, and was then directed perpendicularly onto the target substrate using a low-pressure inertial impactor. Deposition time was controlled by a valve upstream of the impactor.

Magnetron sputtering deposition was done using a Quorum Q150RS Plus rotary-pumped coater (Quorum Technologies, UK), from high purity, 57 mm diameter, 0.1 mm thick gold target. The target-substrate distance was always set at 60 mm, and the substrate holder was rotated at 25 rpm to ensure an even deposition. In order to obtain several gold surface concentrations different sputtering currents, argon pressures, and sputtering times were varied. In some experiments in order to convert the deposited gold layer into NPs, thermal annealing was used by means of a muffle furnace (Thermolyne 62700, USA).

Determination of the surface concentration of gold deposited by spray coating, spark discharge generation, and sputtering was performed by ICP-MS (7700x, Agilent Technologies, USA). Dissolution was done using trace quality aqua regia solution freshly prepared. An integrated autosampler (I-AS) and a MicroMist pneumatic nebulizer equipped with a Peltier-cooled Scott spray chamber were used for sample introduction and argon as carrier. Gold concentration was monitored using standard stock solutions (Inorganic Ventures, USA) in the range of 0 to 100 ppb.

NPs size distribution on the substrate surfaces were characterized by scanning electron microscopy (SEM, S-4700, Hitachi, Japan) at 10 kV accelerating voltage and 10 µA beam current. For experiments involving depth profile measurements of ablated craters or thin film thickness measurements, a Dektak 8 (Veeco/Bruker, USA) contact profilometer was employed. The used stylus applied a constant force of 30 µN into the tip (radius: 2.5 µm, angle: 30°) against the samples.

4.2. Materials

Silicon wafers, diced to 10×10 mm, obtained from Micro to Nano (The Netherlands) were used as substrates in most experiments. 30 nm spherical gold NPs (0.05 $\text{mg}\cdot\text{mL}^{-1}$; Pelco NanoXact, Ted Pella, Inc., USA) were employed in spray-coating depositions. Cylindrical spark discharge electrodes used were made of gold (99.9% purity), whereas in sputtering, a high-purity gold sputtering target (99.99% purity), both of them supplied by Goodfellow (Cambridge Ltd., UK), were used. All experiments involving argon were done using 99.996% purity argon gas obtained from Messer Hungarogáz Kft., Hungary. Digestions prior to ICP-MS measurements were done using concentrated, trace analytical purity nitric acid and hydrochloric acid stock solutions (VWR Chemicals, USA).

4.3. Methods

In addition to the integrated instrumentation software modules, the list of additional software used includes the open-source ImageJ for the evaluation of SEM images, Origin 9.0 (OriginLabs, USA) for the visualization of experimental data, the open-source RStudio Desktop software package (v1.3) for chemometric data evaluation. Additional, in-house developed custom codes were also used which are based on the Chemometrics, MASS, RPart, Caret, PLS and Random forest packages of RStudio.

5. ADVANCED LIBS CHEMICAL MAPPING

LIBS has evolved from a technique for localized elemental analysis into a versatile tool capable of producing spatially resolved, detailed chemical maps of solid materials [101-104]. In this area, our research focused on improving the sensitivity, spatial resolution, and analytical reliability. Our innovations significantly expand the applicability of the method, enabling detailed chemical imaging across diverse materials (e.g. of environmental, industrial or biological origin) and support the development of more robust, high-resolution analytical methodologies.

5.1. Mapping of nanoparticle distributions in polymer thin film nanocomposites

5.1.1. Background

Polymer nanocomposite thin films (PNCTFs) play an increasingly important role in advanced technological applications due to their tuneable mechanical, optical, electrical, and thermal properties [105-107]. Embedding micro- or nanoscale fillers into a polymer matrix offers powerful means to tailor film characteristics, as the properties of the composite are strongly influenced by the concentration, geometry, interfacial behavior, and especially the spatial distribution of the added particles. With the growing interest in functional thin films as coatings, protective barriers, sensor layers, optical components, and energy-related materials [108-111]. However, the ability to control and accurately characterize NP distribution within polymer films has become increasingly important.

One emerging area that places particularly strict demands on PNCTF structure is laser-driven nuclear fusion research. Several recent projects have explored the use of polymer films as hydrogen-rich fuel targets for high-intensity femtosecond laser-driven fusion nuclear energy production experiments, with the use of acrylate adhesives or polyethylene polymers [112,113]. In these approaches, polymer thin layers serve as laser targets, and their composition, optical behavior, and ablation characteristics must be precisely engineered. A novel direction in this field involves doping the films with gold NPs to exploit plasmonic field enhancement, aiming to increase the local electric field strength under femtosecond irradiation and improve the efficiency of ion acceleration. The project Nano-Plasmonic Laser Inertial Fusion Experiment (NAPLIFE), in which our research group also takes part, is one such initiative, investigating a range of polymer matrices doped with gold nanorods as targets [114-115]. Apart from their engineered optical, mechanical, and laser ablation properties [116-117], PNCTFs must also possess a well-defined spatial distribution of NPs. The location, lateral uniformity, and arrangement of the NP fillers are often just as critical as the matrix composition itself. Consequently, there is a need for measurement techniques capable of accurately assessing NP distribution in polymer thin films, ideally over relatively large areas and with micrometer-scale spatial resolution.

This has motivated the search for analytical techniques capable of mapping NP distributions across areas of several square centimeters with micrometer-scale resolution, while providing quantitative information on NP mass or number concentration. Several established methods including scanning electron microscopy (SEM), transmission electron microscopy

(TEM), micro X-ray fluorescence (µ-XRF), and transmission optical microscopy (TOM), can provide valuable insights into NP location or film morphology [118-119]. However, these methods face practical limitations for PNCTFs, such as restricted field of view, limited information depth, incompatibility with polymer substrates, demanding sample preparation, or long acquisition times. Moreover, most are not well suited for mapping relatively large, non-transparent films mounted on solid substrates. LIBS elemental mapping offers a promising alternative for this task, providing micrometer-scale spatial resolution and the ability to interrogate micrometer-thick film layers. While LIBS has been increasingly applied to NP distribution studies in biological and environmental matrices [101-103], its use for polymer thin films, especially for quantitative NP distribution analysis has remained unexplored. Our study addressed this gap by developing a practical LIBS elemental mapping method focusing specifically on polymer nanocomposite thin films.

5.1.2. Experimental

Silicon chips (10×10 mm, Micro to Nano BV, Netherlands) served as the substrates throughout the study. PNCTF test samples were produced by depositing gold NPs on the substrate in a pattern- and concentration-controlled manner and coating them with a polystyrene (PS) thin layer. Gold NP deposition was achieved by magnetron sputtering followed by thermal annealing performed in a muffle furnace, at 550 °C for 20 min. The gold surface concentration was systematically varied by the sputtering current, argon pressure, and deposition time, achieving a more than two orders of magnitude concentration range. Gold surface concentrations were quantified by ICP-MS analysis, employing aqua regia dissolution. **Table 1** summarizes the sputtering parameters and corresponding NP surface concentrations. For experiments requiring patterned concentration gradients (**Section 5.1.4**), samples were produced using an 80 µm thick stainless-steel mask containing laser-cut rectangular apertures. The mask was kept on the Si wafer during sputtering so that only the open regions were exposed to gold. By employing several sputtering cycles, when some apertures were covered with steel plates, zones with different gold concentrations were produced.

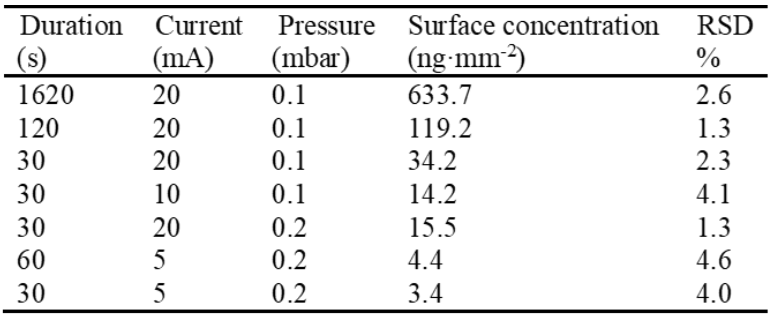

Duration (s)	Current (mA)	Pressure (mbar)	Surface concentration (ng·mm^{-2})	RSD %
1620	20	0.1	633.7	2.6
120	20	0.1	119.2	1.3
30	20	0.1	34.2	2.3
30	10	0.1	14.2	4.1
30	20	0.2	15.5	1.3
60	5	0.2	4.4	4.6
30	5	0.2	3.4	4.0

Table 1. Magnetron sputtering conditions and the corresponding gold nanoparticle surface concentrations (measured by ICP-MS) for the samples deposited on silicon wafers. Table reproduced from own publication [P3].

Polystyrene (PS) used for film fabrication was supplied by the Jülich Centre for Neutron Science (JCNS, Germany), synthesized by anionic polymerization with sec-butyllithium and having an average molecular mass of 110–140 kDa. A 5 wt% PS solution was prepared in analytical-grade toluene (VWR Chemicals, USA) and brought on the patterned and gold NP-decorated substrates by spin-coating (Model WS-650-23B, Laurell, USA). Different film thicknesses were produced by adjusting the spin-coating parameters. A rotation speed of 12,000 rpm for 30 s (acceleration 12,000 rpm s^{-1}) produced films ~147 nm thick, while 4,000 rpm for 30 s produced films ~218 nm thick. Film thicknesses were measured by contact profilometry using the scratch-depth method. Triplicate measurements on three independently prepared films gave RSDs of 5.5 % and 4.2 % for the ~147 nm and ~218 nm films, respectively. For simplicity, these will be referred to as 150 nm and 220 nm films in the text.

LIBS measurement were conducted using a J200 LA/LIBS system, as in most other LIBS experiments during the doctoral work. Spectrum collection was achieved by using a gate delay of 0.5 μs. Elemental maps were acquired using a stepwise raster with 100 μm, non-overlapping laser spots and a pulse energy of 13 mJ (fluence: 165.5 $J\cdot cm^{-2}$). Measurements were carried out under a constant argon stream of 1 $L\cdot min^{-1}$. Gold was quantified via the Au I 523.02 nm emission line. Other details of the related instruments are described in section 4 of this dissertation.

5.1.3. Optimization of measurement conditions

Before the actual determination of NP distribution in PS-gold PNCTF samples could be attempted, a detailed optimization of the experimental conditions and the assessment of the analytical performance had to be done.

A calibration curve was established using the Au I 523.02 nm emission line and the set of standard samples (**Table 1.**) prepared according to the procedure described in section 5.1.2. In this experiment, the PS coating was not employed. This gold spectral line, although it is not the most intense gold transition, was selected to avoid overlap with strong C and Si emissions and to prevent signal saturation, which frequently occurs with the more intense Au I 242.79 nm line. For constructing the calibration plot (**Fig. 9**), single-shot measurements in a 5×6 grid pattern were performed and the gold signal was averaged. By monitoring the analytical signal produced by follow-up shots delivered to the same spots it was established that the fluence used was sufficiently high to completely ablate in a single laser shot.

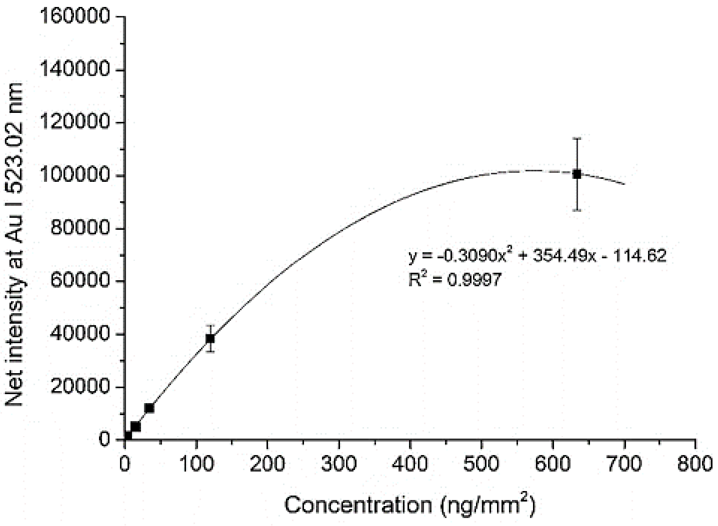

Figure 9. LIBS calibration curve for the mass concentration of gold NPs. Errors bars represent the repeatability calculated from 30 measurements each. Figure reproduced from own publication [P3].

The resulting calibration plot exhibited a monotonous, gradual increase in signal across roughly two orders of magnitude (up to 600–700 ng·mm^{-2}). At the upper end of the concentration range the curve flattens, most likely due to self-absorption caused by the high local gold concentration within the laser-generated plasma. Profilometry data indicated that in the most concentrated calibration samples, the ablated matter contained approximately 1.25 wt% Au. In atmospheric-pressure LIBS, concentrations in the 1-2 wt% range commonly result in partial signal saturation. Although mathematical corrections can sometimes restore linearity [120], such corrections were not applied here.

The limit of detection (LOD) was calculated to be 3.40 ng·mm^{-2}. This value is comparable to typical XRF detection limits for heavy elements such as Au, Hg, or Cr, which often fall between 1 and 10 ng·mm^{-2} [121,122]. LIBS offers the added advantage of detecting low-Z elements (Li, Be, B, etc.) with similar sensitivity, making the technique suitable for almost any NPs, not only gold. Our LOD and dynamic range are in line with recent LIBS-based quantitative gold studies, such as in [123,124], where their reported values are converted to surface concentration units.

The optimization of spatial resolution in mapping applications is very important. The spatial resolution is mainly determined by laser spot size (or rather, the ablation crater diameter). The spot size however cannot be infinitely shrunk, because eventually it is limited by the LOD. Although decreasing the spot size increases the fluence, which – in most cases – also increases the analytical signal in LIBS [125], but there is also less material in the focal spot area, which then lowers the signal. There also are additional considerations to make when NP distributions are to be determined. For example, at the microscopic scale, NPs are the equivalent of analyte “aggregates”, therefore the smaller the analytical spot size, the smaller is the chance of actually having sufficient amount of NPs for detection in the spot. This means that lower NP concentrations may be inaccurately determinable using smaller spot sizes. In our system I compared calibrations obtained with 40 µm and 100 µm spot sizes and it was found that the smaller spot produced roughly only half the sensitivity. Higher spatial resolution is therefore possible, but it is suitable primarily for higher concentration samples.

Another consideration involving laser fluence relates to shockwave effects during nanosecond LIBS ablation and is especially relevant with regards to thin films. In agreement with observations by Rehman et al. [126] and Wang et al. [127], increasing the fluence by reducing the spot size (e.g. from 100 µm to 40 µm at constant pulse energy) causes the ablation-affected zone around the crater to expand significantly, often to nearly twice the diameter. Such expansion eliminates any real gain in spatial resolution. Within this affected region, not only NP rearrangement or melting may occur, but also, UV-induced or thermal degradation, and even pressure-related delamination of the polymer film [128-130]. Considering these factors and the decreased mapping speed, the 100 µm spatial resolution represents a practical and well-balanced value.

I also studied the laser ablation behavior of the PS thin films. To this end, I applied a series of non-overlapping laser shots arranged in a 5×5 grid, mimicking the general conditions used during mapping, on gold NP-decorated silicon substrates covered with 150 nm and 220 nm PS films. The evolution of the Si I 288.15 nm and C I 247.85 nm emission lines during mapping sequence was monitored (**Fig. 10**).

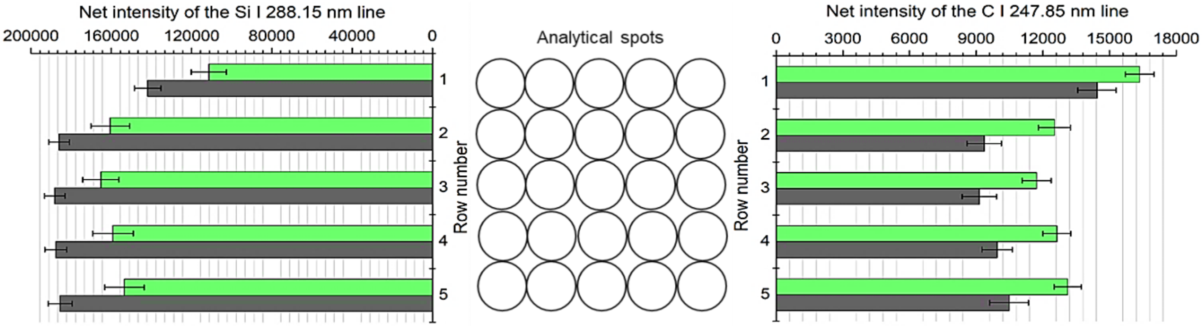

Figure 10. Evolution of net silicon and carbon emission intensities from gold NPs deposited on silicon substrates coated with PS films during LIBS mapping. The row numbers in the bar chart indicate the sequence in which the spots were ablated; within each row, ablation proceeded from left to right. Bars show the mean signal for each row, with error bars corresponding to the standard deviation. Results are presented for 220 nm and 150 nm PS films, depicted by green and grey bars, respectively. Figure reproduced from own publication [P3].

The data reveal that ablation in one row has a measurable effect on the immediately following row, but this influence does not propagate beyond the nearest neighbour. This is reflected in the fact that rows No. 2 to 5 gave rise to about the same signal levels for both Si and C. The Si intensity in the second row is about 20–25% higher than in the first row and then remains constant, which is consistent with partial polymer degradation or thinning around the craters formed in the first row, making it slightly easier to ablate the underlying Si substrate. In contrast, the C signal is highest in the first row by roughly 20–25%, then decreases in the second row and stabilizes at that lower level, likely due to the local removal of some of the PS film by the initial shots. This behavior is observed for both 150 nm and 220 nm films, with the magnitude of the effect varying with thickness. As expected, the thicker film generally produces lower Si and higher C emission for all rows.

The topography of the ablated features was characterized by contact profilometry, from which crater depths and diameters were obtained (**Fig. 11**). The cross-sectional profiles show that the crater rim is unusually elevated relative to the original surface level, the height of the sharp, ring-shaped rim (formed by re-solidified ablated material) actually exceeds the crater depth, which itself is roughly an order of magnitude larger than the PS film thickness. Together with the significant Si signals in **Fig. 10**, these profiles also confirm that the crater depths are larger than the film thickness, hence the ablation is quantitative in the focal spot. A slight inward curvature of the film surrounding the crater is also visible, implying that some polymer is removed in the vicinity of the impact site. The lateral extent of this affected zone is comparable to the crater diameter, which supports the conclusion drawn from **Fig. 10** that the PS film does not undergo large-scale delamination under these conditions, and that LIBS mapping of NP-loaded thin PS films remains feasible.

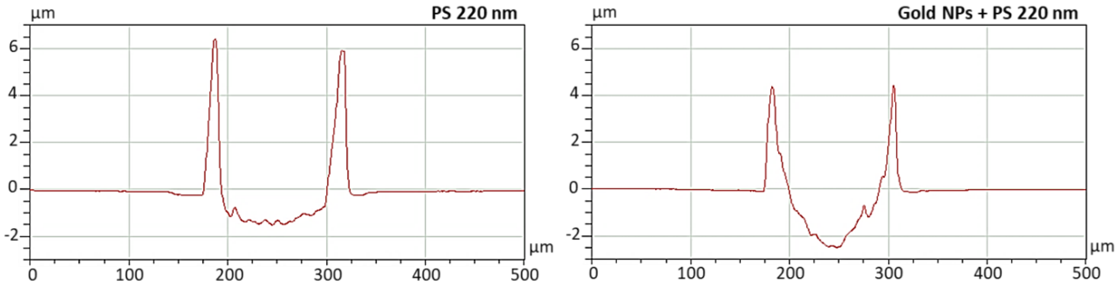

Figure 11. Cross-sectional depth profiles of an ablated crater on a 220 nm PS film without NPs (left) and with NPs (right), produced by a single laser shot employing a 100 µm spot size, obtained by contact profilometry. Figure reproduced from own publication [P3].

I further compared the ablation behavior of PS films with and without NPs and found that the presence of NPs increases the crater depth (e.g. 2.55 µm as opposed to 1.6 µm for the 150 nm film). This is most likely a consequence of the hotter plasma generated in the presence of metallic NPs, as is typical in NE-LIBS [72]. Overall, this indicates that the LIBS elemental maps are not significantly distorted by polymer degradation; only the first mapped row behaves somewhat differently, and this row typically lies outside the main region of interest in practical mapping experiments.

Even though no extensive delamination or severe damage of the polymer film is observed, the polymer layer can still be expected to supress the analytical Au signal at each spot, since a portion of the laser pulse energy is spent on ablating the PS itself. For this reason, I also investigated the gold emission as function of the PS film thickness. The results, presented in **Fig. 12**, clearly show that an increase in film thickness leads to a decrease in Au signal. The relationship is linear over the range studied; at 150 nm thickness, the signal is reduced by about 30%, while at 220 nm the loss is approximately 50%. Linear extrapolation suggests that, under the applied conditions, gold NP detection becomes unfeasible once the PS film thickness reaches around 425 nm. The linear dependence in the suppression plot also makes it possible to calculate a correction factor for a given film thickness, which can be used to estimate the unsuppressed gold signal.

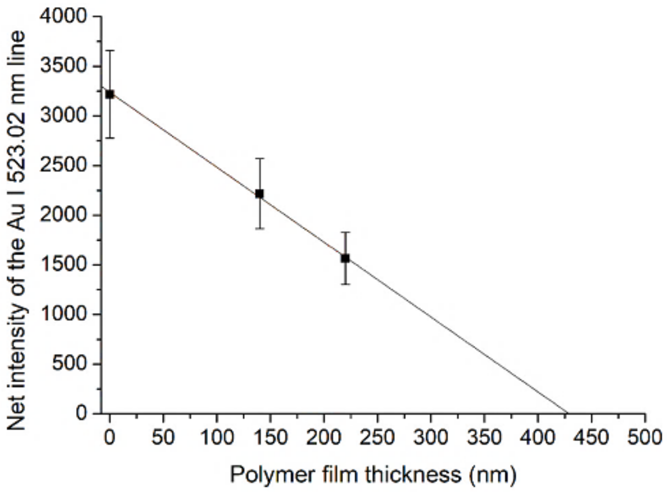

Figure 12. LIBS signal suppression of the gold intensity by PS layers of different thicknesses. Errors bars represent the repeatability calculated from 30 measurements each. Figure reproduced from own publication [P3].

5.1.4. Assessment of the performance

To demonstrate the analytical capability of LIBS elemental mapping for characterizing NP distributions in thin PS films, I applied the technique in two distinct measurement scenarios. In one case, the focus was on evaluating its suitability for determining the spatial distribution of particle number concentration; in the other, it was on the mapping of mass concentration distribution (gradient).

From physical chemistry it is well established that when a droplet of liquid dries on a non-porous solid surface, the dissolved or suspended material is deposited in a radially non-uniform manner, a phenomenon commonly referred to as “coffee-ring effect” [131]. This effect is governed by the non-uniform evaporation rate across the liquid-gas interface and by Marangoni flows driven by temperature gradients [132]. To visualize this ring-like NP deposition, a 5 µL droplet of an aqueous suspension containing 30 nm spherical gold NPs was deposited onto a silicon wafer, dried, and subsequently coated with a 150 nm thick PS layer. The spatial distribution of gold was then analyzed using the LIBS conditions described in the experimental section. The resulting elemental map is presented in **Fig. 13**. A qualitative inspection of the image clearly shows a ring-shaped deposition pattern, with some diffuse NP deposits also present inside the ring, particularly near the edge.

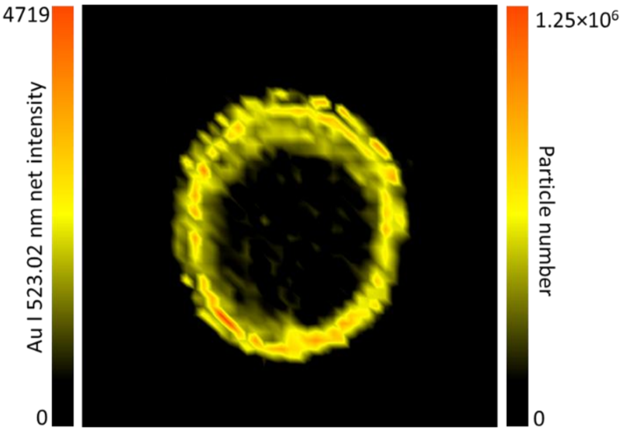

Figure 13. LIBS-based lateral number concentration distribution map of 30 nm spherical Au NPs deposited from a nanosuspension droplet and covered with a 150 nm PS film, recorded at 100 µm spatial resolution over an 8 × 8 mm area. The color scale is proportional to the number of particles per pixel (analytical spot); the total number of particles in the mapped region was 1.37×10^9. Figure reproduced from own publication [P3].

In this specific map, the NP size, and therefore their volume and density are known, allowing the LIBS signal intensities in the elemental map to be converted into a particle number concentration distribution. From these data, the total number of particles detected was estimated to be 1.37×10^9, which is in good agreement with the theoretical value of $1.05 \cdot 10^9$ derived from the certified particle number concentration of the original nanosuspension. The resulting relative deviation of about 30% is comparable to the uncertainty typically associated with routine NP number concentration measurement methods. It should be noted that the accuracy of the calculated number concentration is also affected by factors such as particle polydispersity and the precision of the density values used.

I further evaluated the performance of the method using samples that contained a well-defined patterned, lateral gradient in gold NP concentration (low, medium, and high concentration levels; see experimental section for preparation details and **Fig. 14**). The 10×10 mm Si substrates were coated with either a 150 nm or a 220 nm PS film, and LIBS elemental maps for gold were recorded. As illustrated in **Fig. 14** for the 150 nm film, the spatial distribution of the gold signal closely reproduces the designed pattern, indicating that the 100 µm spatial resolution is sufficient for sub-mm sized pattern reconstruction. The image also clearly reflects the different concentration levels. Since the true mass concentrations in each rectangular zone were known, I was also able to assess the accuracy of the quantitative determination. To this end, 30 signal intensities from random points from each of the three concentration regions were averaged, and converted to mass concentrations. As shown in **Table 2**, the measured concentrations agree well with the true values for both film thicknesses; the deviations are below 10% for all but the lowest concentration level, where the error is approximately 17%. It should be noted that all these concentrations lie near the lower end of the calibration range, and the lowest level is close to the LOD. Therefore, the observed accuracy is considered satisfactory and adequate for a wide range of practical applications.

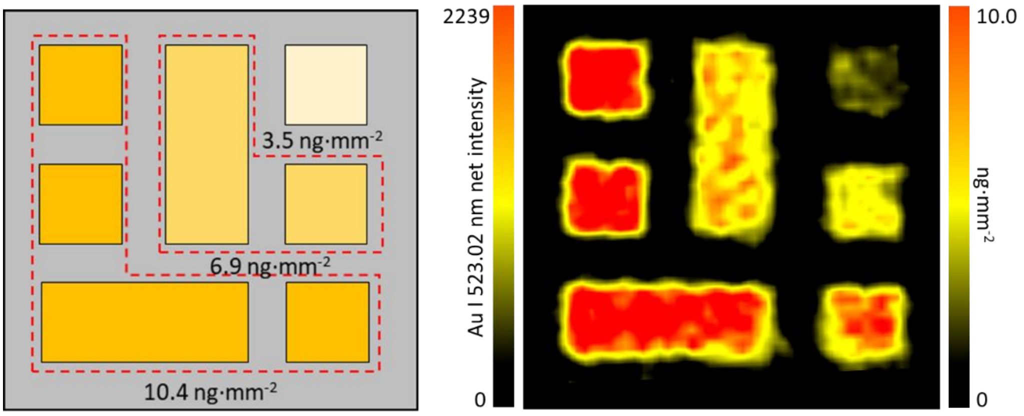

Figure 14. The drawing on the left depicts the designed mass concentration pattern of gold NPs in a 150 nm PS thin film. On the right, the corresponding LIBS elemental map calibrated in terms of mass concentration is shown. The map was acquired with a spatial resolution of 100 µm over an area of 8 × 8 mm. Figure reproduced from own publication [P3].

		150 nm PS film	**220 nm PS film**
Concentration level	True (ICP-MS) concentration	Measured (LIBS) concentration	Measured (LIBS) concentration
Low	3.5	4.1	4.1
Medium	6.9	7.7	7.4
High	10.4	10.0	9.8

Table 2. Comparison of gold NP mass concentration values (ng·mm^{-2}) obtained by LIBS elemental mapping to the true values for thin film samples patterned as shown in **Fig. 14**. Figure reproduced from own publication [P3].

5.2. Sensitization of elemental mapping by employing nanoparticle signal enhancement

5.2.1. Background

Improving the limits of detection remains one of the central challenges in laser-induced breakdown spectroscopy (LIBS), much like in other laser-based spectroscopic techniques where spatial resolution and sensitivity are intrinsically linked. Over the years, numerous enhancement strategies have been explored, including the use of double or multiple laser pulses, plasma-confinement arrangements, or post-ablation reheating approaches [15]; each offering different degrees of practicality and performance improvement. Among these methods, NE-LIBS has emerged as an especially appealing option because it can provide a signal enhancement as large as two orders of magnitude while requiring only the deposition of plasmonic metal NPs on the sample surface (in case of solid samples) or on the substrate surface (in case of liquid samples).

Extensive studies, particularly those carried out by de Giacomo and co-workers [68,72], have clarified many of the mechanisms responsible for the enhancement effect in NE-LIBS (as outlined in section 2.5.5). These effects are strongest when the substrate is conductive; these materials often exhibit enhancement factors in the range of 10–100, whereas insulating or semiconducting samples typically show only modest improvement. The surface concentration of deposited NPs and the laser fluence also strongly influence the magnitude of enhancement, and optimal conditions were established [76].

LIBS has become a widely used tool for elemental mapping across diverse fields [133]. Its attractiveness stems from its ability to record full hyperspectral information with trace-level sensitivity, while providing best spatial resolutions around 10-50 μm. Given these capabilities, integrating nanoparticle enhancement into LIBS mapping appears promising. Indeed, a handful of recent studies have applied NE-LIBS to imaging tasks involving metal samples and plant tissues [81,134]. However, experience accumulated so far has also highlighted several significant challenges. First, droplet deposition; the common method for preparing NE-LIBS samples produces highly inhomogeneous NP distributions characterized by aggregation patterns and coffee-ring structures. While acceptable for localized NE-LIBS analysis, such unevenness is incompatible with mapping, where the enhancement factor must be uniform across all analytical pixels to preserve true chemical information. Furthermore, droplet deposition cannot cover as large areas as required in mapping applications.

A second issue concerns the laser spot size. NE-LIBS typically benefits from relatively large spots (up to ~2 mm) because larger areas support stronger plasmonic coupling from many NPs simultaneously [77]. However, in elemental mapping, large spot size translates to poor spatial resolution, thereby even eliminating certain applications (e.g. granular rock analysis, bioanalysis with cell-resolution, etc.). Thus, a compromise must be found. Additionally, the dependence of enhancement on the electrical and optical properties of the sample introduces further complications; such as the analyte intensity becomes influenced not only by its local concentration but also by matrix-dependent variations in laser-material interaction. This can distort intensity-scaled maps and complicate any attempt to produce quantitative concentration images unless matrix-matched calibration is performed [103]. Finally, optimizing enhancement parameters such as NP size, laser wavelength, and temporal detection settings; is more demanding in NE-LIBS mapping because samples are often unique and cannot be re-measured. Spatially varying enhancement across heterogeneous materials can also make optimization relative rather than absolute.

Recognizing that these challenges have not been adequately addressed in the NE-LIBS literature, I systematically examined three NP deposition methods, spray coating, spark discharge generation (SGD), and magnetron sputtering, and evaluated their suitability for NE-LIBS mapping relative to the conventional droplet approach. I further investigated the influence of laser spot size, wavelength dependence, and detector timing on the enhancement effect, and demonstrated NE-LIBS mapping performance in two applications: i) a rock sample and ii) paints discrimination.

5.2.2. Experimental

The substrates used for NP deposition were 10×10 mm silicon wafer pieces (Ted Pella, Inc., USA) and soda-lime glass microscope slides (Epredia, Germany). In all deposition experiments, gold nanoparticles were produced. Spray coating was performed using commercial spherical gold NPs and the surface concentration was controlled by the spraying time, varied in the range of 10 to 100 s. SDG-based NP deposition was carried out in our laboratory-built system using pure gold electrodes. The deposition times used were varied and controlled by an on/off valve before the impactor. Further details of our spark discharge setup can be found in e.g. [135,136]. Magnetron sputtering deposition was performed using a rotary-pumped coater, on glass microscope slides as substrates. the applied current was 20 mA and the argon pressure was 0.1 mbar. Sputtering time was varied in a range from 60 to 360 s. The sputtering-deposited gold thin film was subjected to thermal treatment in a muffle furnace [137] which resulted in the formation of "quasi-spherical" NPs.

The size distribution of the deposited gold NPs and their laser ablation behavior were examined using scanning electron microscopy (SEM). The total gold surface concentration ($\mu g \cdot cm^{-2}$) was measured by ICP-MS after dissolving the samples in freshly prepared aqua regia. Calibration was performed using 0-100 ppb Au standards and analytical signals measured at the ^{197}Au isotope.

All LIBS measurements were performed using our J-200 LA/LIBS system, already described. Plasma light was collected employing a 0.5 µs gate delay and 1 ms gate width. Experiments were carried out under constant argon flow with a rate of 1 $L \cdot min^{-1}$. NE-LIBS scanning/mapping measurements were acquired using stepwise, non-overlapping 200 µm laser spots sizes., although a 60 µm spot was tested in one experiment. Pulse energies between 10 and 18 mJ were applied, corresponding to fluences of 31-56 $J \cdot cm^{-2}$. LIBS measurements requiring high temporal resolution were carried out using an echelle spectrometer (Aryelle 200, LTB). Plasma emission within the J-200 LIBS system was collected using a fiber-optic light collection module custom-built for our laboratory by ASI Inc. The setup employs a 400 µm core fiber to guide the light to the 40 µm entrance slit of the echelle spectrometer. The detector gate width was set at 1000 ns while the gate delay was varied from 0 to 5 µs.

The standard gold NPs suspension, spray coating, sputtering, SDG system, muffle furnace, ICP-MS, LIBS system, and the echelle spectrometer specifications and data evaluation methods, were already described in section 4 of this dissertation.

In geology-related experiments, a monzogranite type granitoid rock originating from the Mórágy Hills in the Eastern Mecsek Mountains (Hungary) was used. The rock was sectioned with a diamond saw (DiscoPlan, Struers, Denmark) to obtain a 20×20 mm surface, which was then polished using a LaboPOL-35 system (Struers, Denmark) with 500- and 1200-grit MD-Piano diamond disks. Final smoothing was achieved with an aqueous SiC abrasive suspension (Buehler, USA), after which the sample was thoroughly rinsed with high-purity deionized water and analytical-grade ethanol and set to dried.

For the paint discrimination studies, five commercial, black, heat-resistant automotive paints (rated for 600-800 °C) were selected. Each paint was applied to 20×30 mm stainless-steel plates from a distance of approximately 30 cm. Three layers were sprayed, allowing 15 minutes of drying time between coats. After each coating, the samples were baked at 160 °C for one hour in an oven (Memmert, Germany). To ensure that the steel substrate would not be exposed during LIBS analysis, depth-resolved test measurements were performed using the same laser settings later applied in the mapping experiments, monitoring the spectra to confirm sufficient paint thickness.

5.2.3. Morphology of the deposited NP layer

SEM imaging was used to evaluate the nanoparticle layers produced by the three deposition techniques, both in terms of deposition uniformity and the morphology and size distribution of the resulting Au NPs.

Spray coating resulted in the formation of large, ring-shaped features, within which NP clusters of irregular shape and variable size were evident. As shown in **Fig. 15**, the deposited structures were highly non-uniform at the microscopic scale. Similar patterns have been described previously [138] and are known to arise when the substrate is only partly wetted by the suspension. During drying, suspended particles migrate toward the droplet perimeter and accumulate there, producing a solid outer ring with dispersed “islands” inside. This migration is driven by an outward flow generated as the solvent evaporates. Although spray coating delivers many microdroplets to the substrate, the resulting nanoparticle distribution is too uneven to be suitable for NE-LIBS mapping applications.

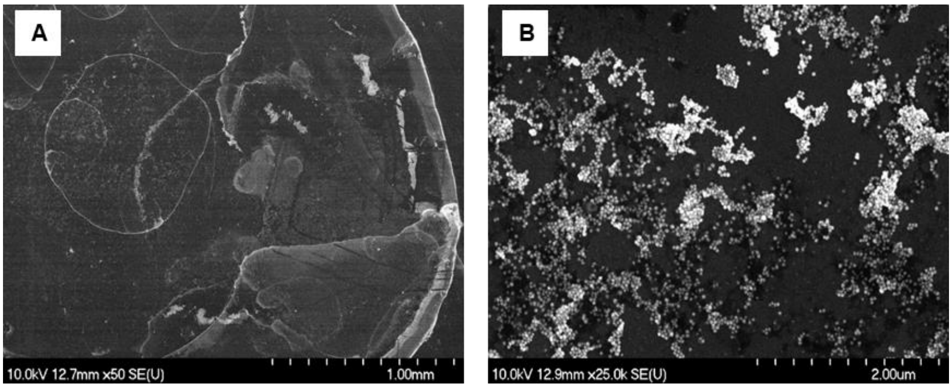

Figure 15. SEM images of Au NP deposits generated by spray coating. Figures A and B depict separate substrate areas captured at different magnifications**.** Figure reproduced from own publication [P1].

SDG produced a more homogeneous distribution than spray coating, with less aggregation. The deposited gold particles were generally spherical, well separated, and showed consistent spacing. Two SDG aerosol delivery modes were tested: with an orifice to focus the nanoaerosol and one without any focusing. As expected, using the orifice created a more concentrated deposition in the center which gradually thinned out toward the edges **(Fig. 16a**), whereas omitting the orifice produced even distribution across the entire substrate (**Fig. 16b**), although at a much lower overall surface loading. Longer deposition produced more aggregates, but these were numerous small clusters rather than a few large ones. The mean particle size remained roughly constant at 22 nm across different deposition durations.

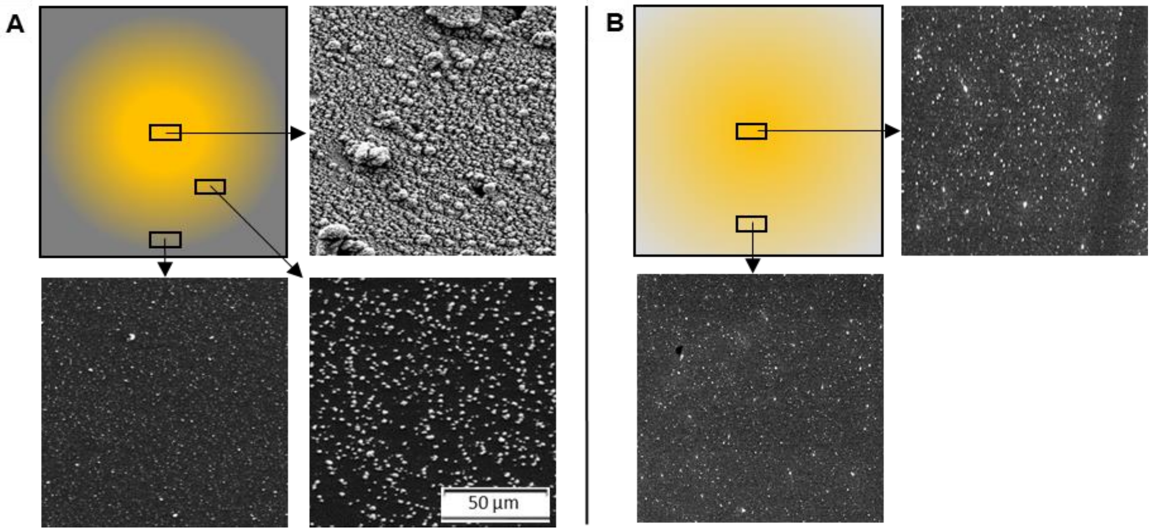

Figure 16. SEM images of gold NPs deposited by SDG on a silicon wafer (1000 s deposition). The panels illustrate the difference in NP distribution when using an aerosol-focusing orifice (A) and when depositing without the orifice (B). Images were taken at the same magnification. Figure reproduced from own publication [P1].

In magnetron sputtering, energetic plasma ions collide with the gold target and eject atoms that condense on the substrate to form a thin film. SEM images (**Fig. 17**) show this film as a granular layer with closely packed nanoislands rather than discrete particles. A 20-min heat treatment at 550 °C converts this layer into quasi-spherical NPs through film breakup, stress relaxation, and surface diffusion [137,139]. The resulting particle sizes depend on sputtering time and range from roughly 10 to 50 nm. Among the examined deposition methods, sputtering followed by thermal treatment produced the most suitable NP morphology for NE-LIBS mapping. For simplicity, I will refer to this combined process as sputtering.

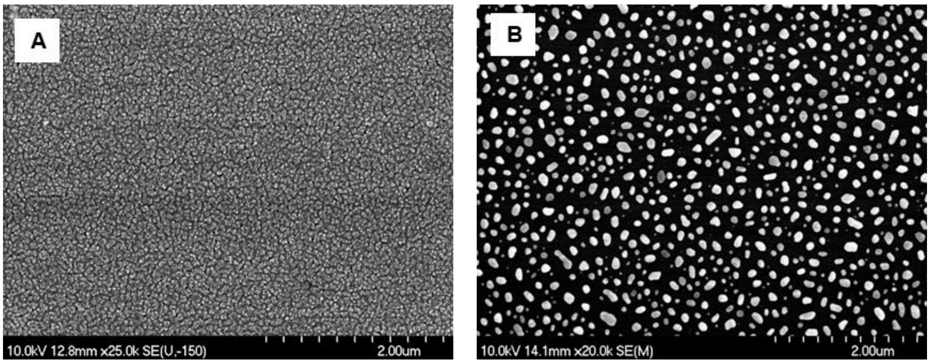

Figure 17. A) Gold-coated glass sample after 240 s of sputtering, prior to thermal treatment. B) The same sample following 20 min of annealing at 550 °C. Figure reproduced from own publication [P1].

5.2.4. Nanoparticle surface concentration and inter-particle distances

Previous experimental and theoretical studies indicate that achieving NE-LIBS signal enhancement requires metal surface mass concentration of roughly 1-3 µg·cm^{-2} and inter-particle distances (IPDs) similar to NP diameter to ensure efficient plasmon coupling [75,76].

With this in mind, I evaluated how well each deposition method allows control over these key parameters.

To determine surface mass concentration, all sides and the backside of the silicon wafers were masked so that only a 10×10 mm area remained exposed during deposition. After coating, the masks were removed, the deposited gold was dissolved in aqua regia, and the solutions were analyzed by ICP-MS. The results are presented in **Fig. 18**. As shown, all three deposition methods allow the surface concentration to be tuned simply by adjusting deposition time, with nearly linear relationships between concentration and time. Among them, sputtering provides the most precise control. Importantly, each technique is capable of achieving the desired mass-concentration range of a few µg·cm^{-2} needed for effective NE-LIBS enhancement.

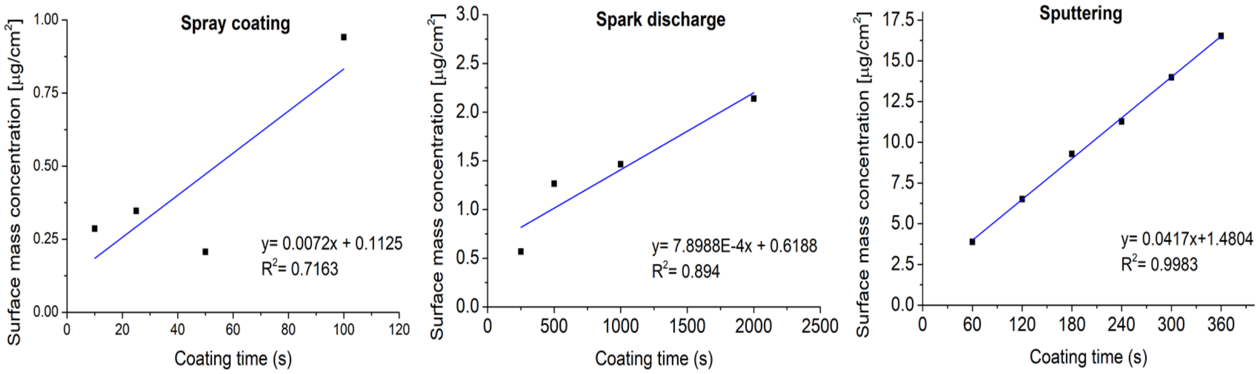

Figure 18. Surface mass concentration of deposited gold NPs as a function of coating time for the different deposition techniques determined by ICP-MS. Figure reproduced from own publication [P1].

Among the three deposition techniques, spray coating would in principle offer the most precise control over NP size, since the process does not alter the diameter of the deposited particles. However, the strong aggregation and pattern formation produced by this method makes the reliable estimation of IPDs impossible. Despite the absence of thermal stress on the sample, the pronounced inhomogeneity of the deposits renders spray coating unsuitable for NE-LIBS mapping.

In the SDG deposition, with the focusing orifice in place, the average IPD decreased from 62.2 nm to 30.0 nm as the deposition time increased from 250 to 2000 s, while the particle diameter remained constant at 22 nm. This means that optimal NP to IPD ratios can theoretically be achieved, but only in a restricted central region where the aerosol beam is most concentrated. Homogeneous deposition was attainable only when the orifice was removed, although this required impractically long deposition times (often exceeding 60 min). Furthermore, coating larger substrates (several cm^2) is challenging with SDG. An advantage is the absence of thermal load on the sample.

In the case of sputtering, both NP size and IPD was found to depend strongly on the coating time. Beyond 360 s, the particle morphology became irregular, but in the 10–240 s range the NP diameter increased from 8.87 to 51.49 nm while maintaining a spherical shape. At the 240 s deposition time selected for subsequent experiments, the average NP diameter was

51.5 nm and the mean IPD was 86.7 nm. These values are within the range required for effective NE-LIBS enhancement [72,76]. Sputtering also enables the coating of large substrates. Its main drawback is the need for a 550 °C post-annealing step, which restricts its use to thermally stable samples.

Overall, sputtering provided the most favorable and controllable NP size distribution for NE-LIBS mapping and was therefore adopted for all subsequent experiments.

5.2.5. Laser ablation behavior of the nanoparticle layer

In addition to other requirements, NE-LIBS theory emphasizes the need for using large laser spot sizes while maintaining fluences in the typical LIBS regime (tens of $J \cdot cm^{-2}$). Large spots allow thousands of NPs to be excited simultaneously, promoting efficient plasmon coupling through the strong local electromagnetic field. In practical NE-LIBS applications, this often requires millimeter-scale spot sized and laser systems capable of delivering pulse energies above 100 mJ [72,77]. This disadvantage is somewhat offset in localized NE-LIBS analysis though as it simplifies the NP deposition procedure. This is because pre-shots from the same laser can first create a sufficiently large ablation crater that serves as a target for depositing a small droplet of NP suspension (e.g., 1 µL). Therefore, the crater confines the droplet during drying, prevents spreading, and effectively concentrates the NPs in the desired region [68,72].

High spatial resolution is essential in elemental mapping, which conflicts with the large laser spot sizes typically recommended for NE-LIBS. Using very small NPs to compensate for this is not viable, as they offer fewer electrons for plasmon formation. Also, maintaining nanometer scale IPDs is impractical, and the size distribution of ultra-small NPs are broader since they tend to be less spherical, and they may be re removed more rapidly during ablation. These factors greatly reduce the achievable signal enhancement. High resolution mapping also requires highly uniform NP layers. Thus, a compromise between resolution, enhancement, and practicality is necessary. In my view, spot sizes of 100-200 µm paired with NPs of a few tens of nanometers provide a workable balance, especially if the nanocomposite films are used as laser targets.

Even with suitable spot sizes and homogeneous NP deposition, the laser-NP interaction must be evaluated to ensure that NE-LIBS can produce reliable maps. Line-scan (continuous) mapping is not feasible because overlapping craters would remove the NPs before the next pulse. Only stepwise, non-overlapping shots can be used, and it must be confirmed that the ablation shockwave does not laterally displace the NPs, which would affect the minimum mapping step size. To assess this, gold sputtered NP-coated silicon substrates were exposed to adjacent single laser shots at different fluences, and SEM imaging was performed. As shown in **Fig. 19b**, the crater interior and rim consist of molten and resolidified material, while regions further from the rim retain the original NP layer (**Fig. 19c**). A narrow band surrounding the rim exhibits a higher NP density, indicating that the outward shockwave redistributes NPs into this zone (**Fig. 19a**). This band was a few tens of µm wide under those conditions. Because this displaced-NP region enlarges the area affected by each pulse, the effective spatial resolution in NE-LIBS mapping is the sum of the diameter of the ablation crater with the molten rim plus the width of the compressed NP band. Further study of the effect of pulse energy and laser spot size, and closely adjacent shots is required to precisely quantify this limit.

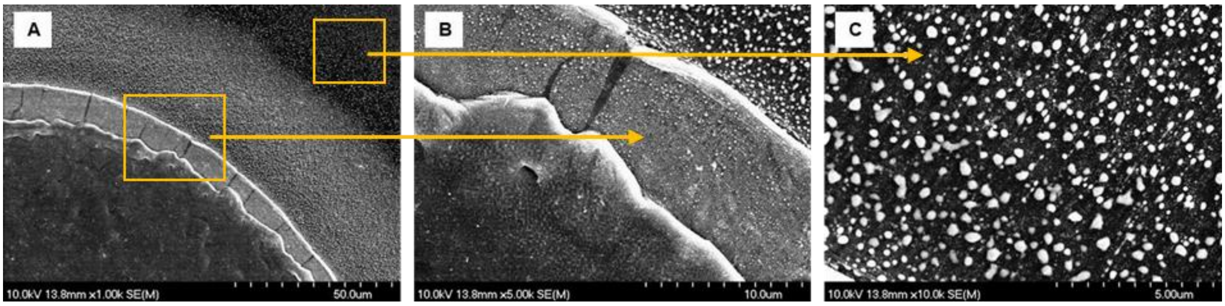

Figure 19. SEM images at different magnifications showing sections of an ablation crater and its surroundings on a silicon substrate coated with sputter-deposited gold NPs. The orange boxes in image A) highlight the regions enlarged in images B) and C). The laser fluence employed was 31.83 J·cm^{-2}. Figure reproduced from own publication [P1].

To assess how laser parameters influence NP redistribution, I varied the laser spot size (60 and 200 µm) and pulse energy (5, 10 and 15 mJ) and examined the resulting laser ablation behavior under non-overlapping step-scan mapping conditions. Representative SEM images are shown in **Fig. 20**. A key observation is that the width of the “compressed” or “rearranged” NP band surrounding each crater depends strongly on laser fluence; this band becomes noticeably wider, both in absolute size and relative to the crater diameter when using the smaller 60 µm spot size. This behavior clearly reflects the stronger shockwave effects at higher fluences.

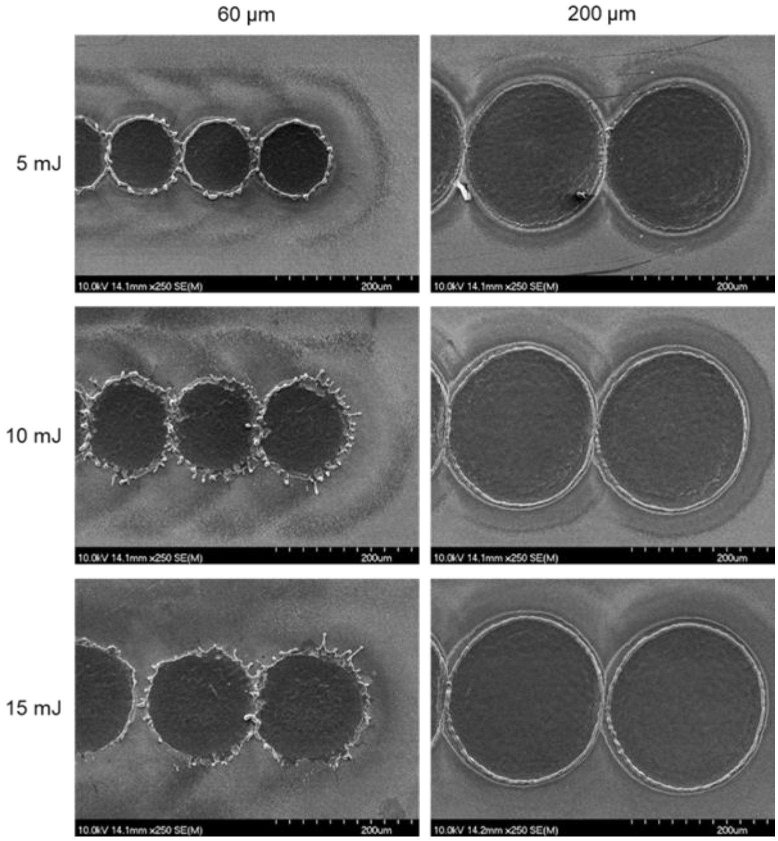

Figure 20. SEM images of craters on sputtered Au-NP-coated silicon produced with various laser energies and spot sizes. Adjacent images show laser ablation at fluences differing by one order of magnitude. Figure reproduced from own publication [P1].

Rehman et al. [126] and Wang et al. [127] have shown that shockwave propagation in ns laser ablation increases nonlinearly with fluence, with velocity scaling roughly with the cubic root of the fluence. Given the ~11-fold higher fluence of the 60 µm spot, a more than two-fold increase in shockwave travel distance is expected, matching this observation that the ablation affected zone is 2-2.5 times wider than in the 200 µm case. The compressed NP band grows with pulse energy for both spot sizes, making small spot sizes unsuitable for NE-LIBS mapping because the effective resolution becomes far inferior to the nominal spot diameter. At lower fluences, the width of the compressed band remains quite small (around 20 µm) compared to the 200 µm spot diameter; therefore a spatial resolution of ~175 µm remains feasible. Step-scan experiments showed no cumulative disturbance from adjacent shots, confirming that NE-LIBS mapping is practical with 5-15 mJ pulses if ca. 175-200 µm spot sizes are used. Finally, “true spatial resolution” should be based on the actual crater size, not the optically set spot diameter, since LIBS typically produces larger craters at high fluence. Only step-scan mapping accurately reflects this. Based on this optimization, ~200 µm represents a realistic spatial resolution for NE-LIBS under the conditions used.

5.2.6. Signal enhancement

As noted earlier, NE-LIBS signal enhancement (SE) (defined as the ratio of the net emission intensity with and without NPs), depends strongly on several experimental factors, including laser parameters, NP properties, and the characteristics of both the sample and substrate, many of which influence one another. In this study, I examined how selected parameters affect SE for soda-lime glass samples coated with gold NPs prepared by the sputtering-based deposition method.

Laser fluence influences not only NP-layer ablation but also the magnitude of the SE. As reported by De Giacomo et al. [76], SE typically shows a maximum with fluence due to nonlinear electron-excitation processes, resulting in the generation of hot electrons and effective charge separation. My results (**Fig. 21**) confirm this behavior, although both LIBS and NE-LIBS signals rise with fluence, NE-LIBS increases more rapidly up to an optimum of ~30-32 $J \cdot cm^{-2}$ (ca. 5 $GW \cdot cm^{-2}$ irradiance), consistent with literature values (3.5-4 $GW \cdot cm^{-2}$) for metallic samples [76] The decline of SE at a certain point is attributed to faster NP evaporation at higher fluence, which diminishes their contribution to enhancement.

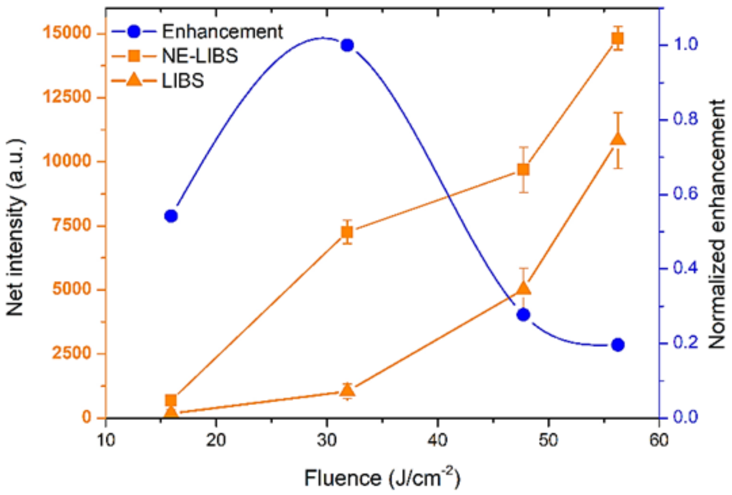

Figure 21. Influence of laser fluence on NE-LIBS signal enhancement for the Si I 288.15 nm line on glass using 266 nm laser pulses (conditions e.g., 200 µm spot size, integrative detection, are the same as those used throughout this section). Error bars are standard deviations from three repetitions. Figure reproduced from own publication [P2].

Detector gating strongly influences LIBS signals because plasma emission is highly transient, following the evolution of the temperature and electron density in the plasma. In NE-LIBS, optimizing gate delay and gate width is particularly important, as NPs have a brief lifetime during laser ablation; consequently, the highest SE occurs at very early times (when short gate delays and widths are used). As shown in **Fig. 22a**., SE reaches its maximum for gate delays below ~1 µs when short gate widths (e.g., 1 µs) are used, with neutral lines exhibiting slightly longer optimal gate delays than ionic lines, consistent with previous reports [75]. On the other hand, longer gate widths significantly reduce the achievable SE. **Fig. 22b** illustrates this, while fast gating achieves maximum SE values of 20-27 (depending on the emission line), integrating the full plasma lifetime results in SEs of only 6-9. This is due because most routine LIBS instruments employ CCD detectors with ms-range integration times, this explains why many studies report only single-digit SE values rather than the much higher enhancements seen with optimized fast-gated detection [66,81].

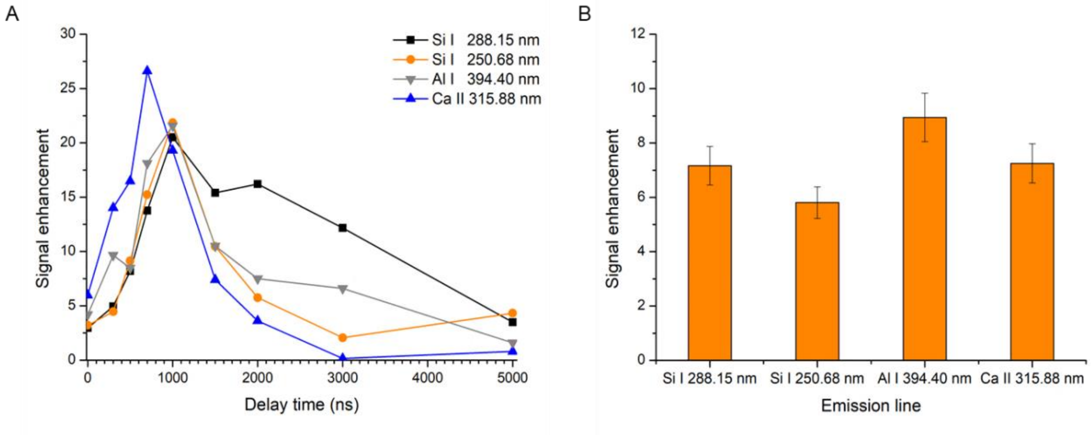

Figure 22. Influence on detection gating on NE-LIBS signal enhancement for selected elemental lines in glass. A) Fast gating (1µs gate width, variable µs-range gate delay). B) Time-integrated enhancement corresponding to

CCD-based LIBS systems with ms-range gate width. Experimental conditions are the same as those used throughout this section. Error bars are standard deviations from three repetitions. Figure reproduced from own publication [P2].

In ns-LIBS, plasma formation depends strongly on the sample absorption at the excitation wavelength, while in NE-LIBS the laser pulse also drives localized surface plasmons in metallic NPs. Although wavelength-LSP resonance is beneficial in NE-LIBS, but it is not essential for significant SE [76]. Moreover, tunable lasers sources are uncommon in LIBS, thus fine tuning the laser wavelength to LSP resonance is more of a theorical than practical option. Using identical conditions except for wavelength, I evaluated NE-LIBS performance at 266, 532, and 1064 nm on gold-sputtered glass. The calculated SE values are shown in **Fig. 23**. A consistent decrease in SE with increasing wavelength was observed, in agreement with earlier studies [72,140]. Because soda-lime glass absorbs minimally at 532 and 1064 nm but more strongly in the UV, plasma formation is easier and LIBS intensities are higher at 266 nm. Meanwhile, the 51 nm diameter Au NP used in this experiment have a broad LSP absorption peak (FWHM ca. 80 nm) near 550 nm [141]. If wavelength-LSP resonance dominated the enhancement, the highest SE would appear at 532 nm, yet the opposite trend is seen. The approximately λ^{-1} behavior aligns instead with the Keldysh parameter wavelength dependence [142], suggesting that, in the fluence regime used, there is no shift in the ionization mechanism (the transition from $\gamma > 1$ to $\gamma < 1$ does not occur). Overall, **Fig. 23** indicates that 266 nm wavelength produces slightly higher SE (25-50% more) than 532 or 1064 nm, the latter wavelengths offer higher available fluence due to reduced harmonic-conversion losses. This offers more flexibility for optimizing NE-LIBS performance at the fundamental and second-harmonic wavelengths. In practice, all three wavelengths can therefore offer comparable analytical capability for NE-LIBS mapping.

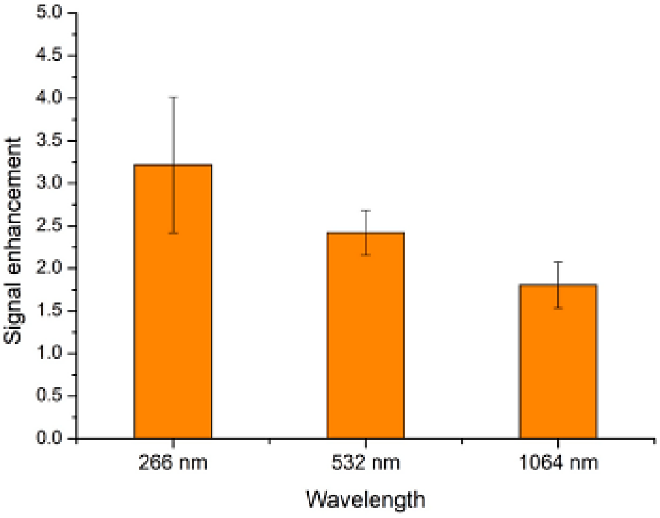

Figure 23. NE-LIBS signal enhancement for the Si I 288.15 nm line as a function of laser wavelength on a glass sample. Measurements were acquired in integrative mode at a constant fluence of 31.77 J·cm^{-2}, with all other same conditions used throughout this section. Error bars are standard deviations from three repetitions. Figure reproduced from own publication [P2].

To evaluate the repeatability of SE across the sample, stepwise line scans were performed on a glass substrate coated with sputtered Au NPs. The Si I 288.15 nm emission line was recorded along a scan line extending beyond the coated region, allowing the non-sputtered glass to serve as a reference for enhancement. As shown in **Fig. 24**, a SE of approximately 7-8 was obtained using integrative detection. Repeatability was good, with relative standard deviations of 5-10% across five replicate scans. The stable signal level within the coated zone indicates that the NP layer exhibits sufficient homogeneity for NE-LIBS mapping.

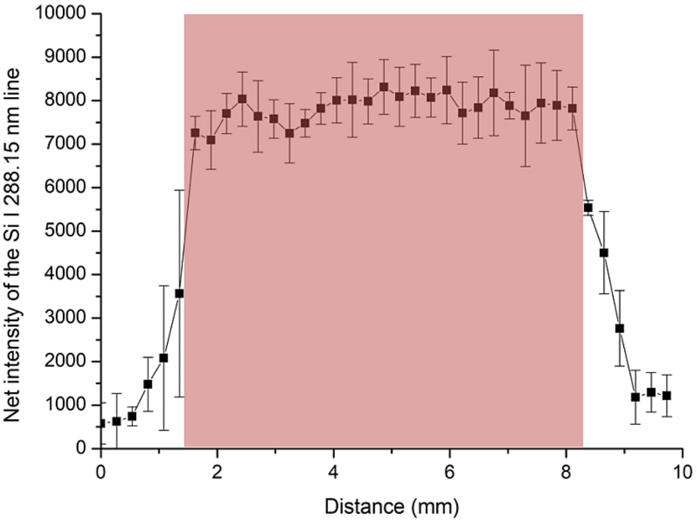

Figure 24. Stepwise line scan across a glass substrate coated with sputtered Au NPs. The central, sputtered region (shaded area) was defined using a 6.5 mm-wide mask during deposition. Experimental conditions match those used throughout this section. Experimental conditions are the same as those used throughout this section. Error bars are standard deviations from five repetitions. Figure reproduced from own publication [P1].

5.2.7. Applications of NE-LIBS mapping

The preceding experiments demonstrated that magnetron sputtering followed by thermal treatment provides a practical and effective sample preparation strategy for NE-LIBS elemental mapping. The approach has two main constraints: i) the attainable spatial resolution is limited by the required 200 µm laser spot size, and ii) the method is restricted to materials that can tolerate the 550 °C annealing step. In the following sections, I demonstrate its applicability to geological and industrial samples.

LIBS elemental mapping of geological materials has gained significant attention, particularly for the study of the distribution of light elements such as Li and Be, which are critical in many industrial applications. LIBS enables rapid, spatially resolved prospection of elemental distributions within mineral grains [143-145]. In order to utilize this, a monzogranite type granitoid sample from the Mórágy Hills was prepared by cutting, grinding, and polishing, followed by the sputter-deposition procedure described earlier. A 20×20 mm area was subjected first to conventional LIBS mapping. The surface was then lightly repolished (removing around 15-20 µm thick layer), and coated again with Au NPs for NE-LIBS mapping. Mapping was performed in step-scan mode using non-overlapping 200 µm spots, 10 mJ pulse energy, 0.5 µs gate delay, and 1 ms gate width, while continuously flushing the chamber with argon. Elemental images were generated by integrating selected emission lines. Representative LIBS and NE-LIBS maps for Li I 670.78 nm and Mg I 518.36 nm are shown in **Fig. 25**. As expected, biotite grains, visible as dark regions in the microscope image show a higher amount of Li and Mg relative to other surrounding mineral grains (feldspar, quartz, and amphibole) [144]. The correspondence between the optical image and the NE-LIBS maps indicates that the NP deposition was uniform and did not disrupt the mineral microstructure. With ms-range gating, SE factors of three for Li and two for Mg were obtained. Although modest, these enhancements improve detection sensitivity and support more reliable quantitative mapping. As demonstrated in the next section, the improved signal can also enhance classification tasks, such as distinguishing mineral grains or compositional zones within a sample.

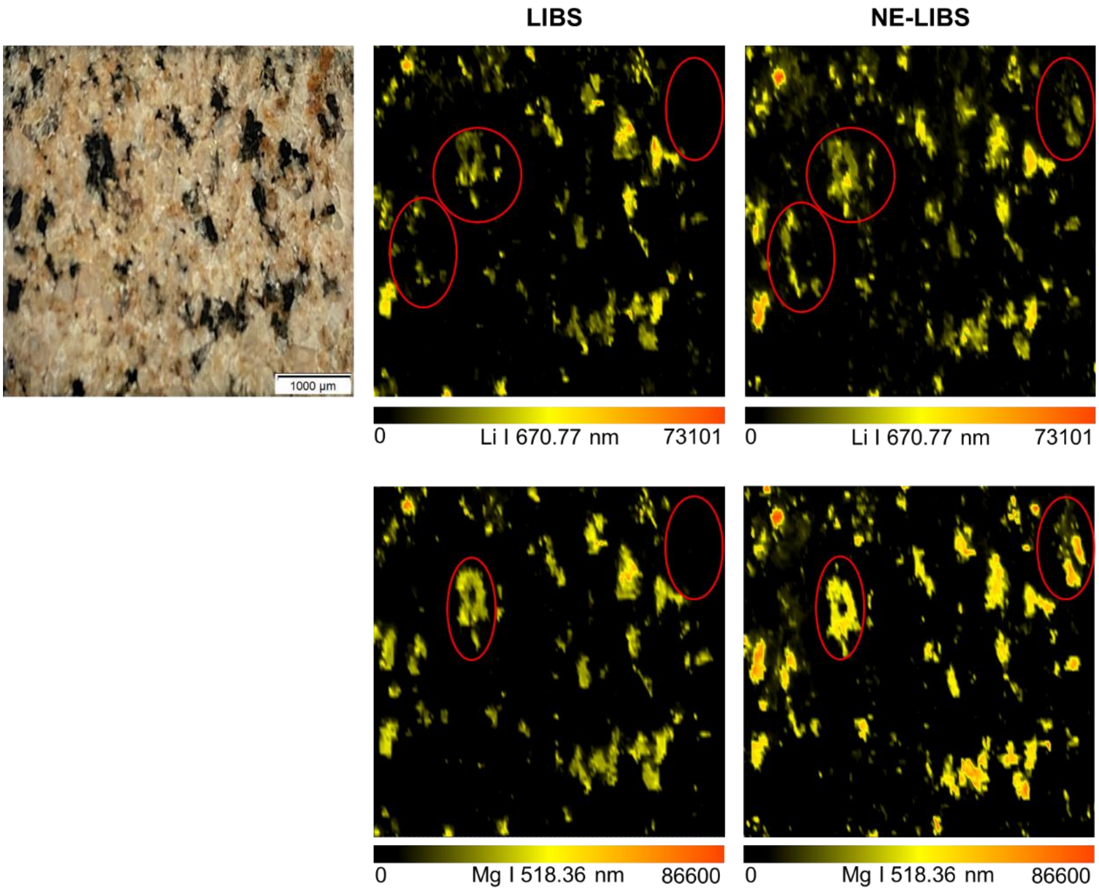

Figure 25. Microscope image (left), as well as Li (top row) and Mg (bottom row) LIBS elemental maps recorded with and without NPs. Figure reproduced from own publication [P2].

A particularly promising application of NE-LIBS mapping is the spatial classification (or identification) of distinct material zones within a sample using chemometric methods of the hyperspectral data generated. While LIBS has previously demonstrated such capabilities [146,147], but according to its concept, I hypothesized that the added SE (signal-to-noise ratio improvement) provided by gold NPs would further enhance classification accuracy. To test this concept, I analyzed five commercial black thermo-paints (labeled A-E), commonly used on automotive components exposed to high temperatures. Each paint was sprayed onto stainless steel substrates. Preliminary tests confirmed that the paint layers were sufficiently thick to prevent substrate ablation. Visually, the paints were nearly indistinguishable, exhibiting only very subtle differences in shade; an ideal scenario for evaluating classification performance. Two sample sets were prepared, one for conventional LIBS and one for NE-LIBS. For each paint, 50 spectra were collected from different positions under identical measurement conditions.

Classification accuracy was assessed using PCA and LDA. In each iteration, data were randomly divided into training and validation sets using a 7:3 ratio. As shown in **Fig. 26**, PCA scatterplots reveal that spectral clusters for paints A, B, and D overlap extensively in the LIBS case but separate distinctly when NE-LIBS spectra are used. LDA provided similar visual improvement and enabled quantitative accuracy evaluation through confusion matrices. Across ten randomized runs, NE-LIBS achieved a validation accuracy of 98.0 ± 1%, compared with only 84.0 ± 2% for LIBS. These results demonstrate that NE-LIBS significantly enhances spatial classification performance, likely due to improved spectral contrast and reduced noise. Please note that preparing a clean, well-defined patterned sample from the spray-paints was not feasible; thus, this experiment serves only as a proof of concept demonstrating the advantages of NE-LIBS for spatial classification. To further illustrate the improvement in classification accuracy, **Fig. 27** represents a virtual pattern in which confused pixels are distributed proportionally as found in the LDA confusion matrices.

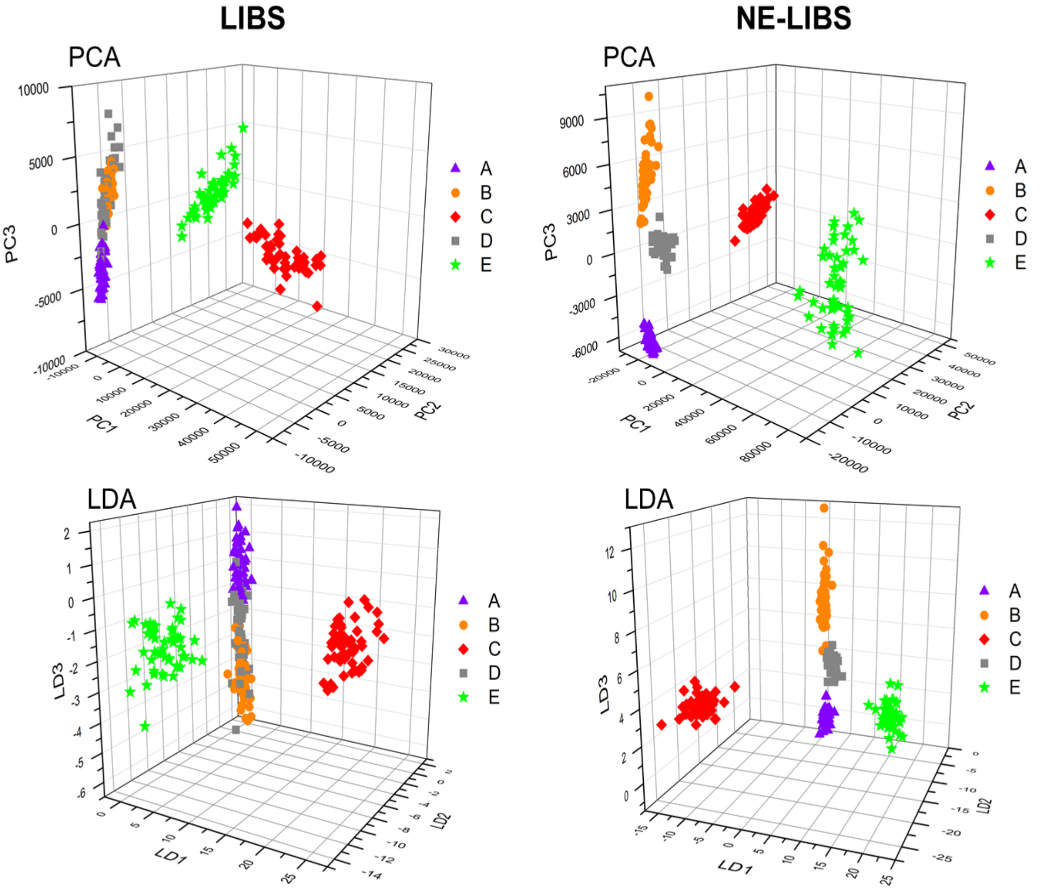

Figure 26. Comparison of the classification for five black paint samples using LIBS and NE-LIBS hyperspectral data using PCA and evaluation. Figure reproduced from own publication [P2].

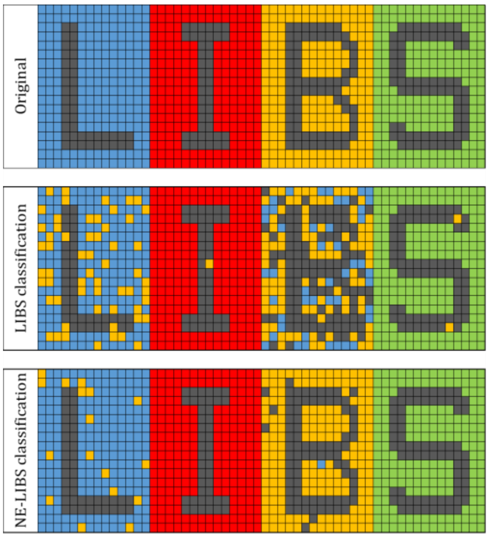

Figure 27. Virtual patterns with confused pixels in proportions corresponding to the obtained LDA confusion matrices for the discrimination experiment with black paints. The picture is meant to illustrate the improvement in classification accuracy. Figure reproduced from own publication [P2].

5.3. Study of the distribution of trace elements and nanoparticles in plants

5.3.1. Background

LIBS has become a valuable tool for studying elemental distributions in plant tissues. Its ability to provide multielemental, spatially resolved information, although with some laborious sample preparation, makes it especially suited for investigating nutrient transport, trace element dynamics, and metal uptake in developing plants (seedlings). Thus, allows researchers to visualize how essential elements (e.g., Ca, K, Na) and trace metals or contaminants accumulate in specific anatomical regions such as roots, stems, and leaves. This capability is particularly relevant for studies on plant nutrition, phytoremediation, and environmental stress responses. In recent years, LIBS mapping has also proven useful for monitoring the bioaccumulation and translocation of engineered nanoparticles, providing insights into their interactions with plant tissues and potential ecological impacts [104,148-150].

In the experiments discussed in this chapter, I focused on the LIBS analysis of tomato seedlings, primarily with regard to trace element distribution mapping, for environmental and plant-biological applications. Particular emphasis was placed on the behavior and bioaccumulation of ZnO NPs on zinc deficient tomato. Zinc is the second most abundant transition metal, is vital for all living organisms, yet Zn-deficient soils are common worldwide, including in Hungary. In this study, I collaborated with the Department of Plant Biology of the Institute of Biology of the University of Szeged, in a study which examined how ZnO NPs of different sizes influence the development of *Solanum lycopersicum* L. cv. Mano grown in a Zn-deficient nutrient solution.

Plants acquire most of their zinc from soil, where Zn^{2+} may constitute up to half of the soluble Zn pool [151]. However, Zn availability is often limited by factors such as low soil Zn levels, high pH, excess phosphorus, or flooding, leading to Zn deficiency. Sensitive plant species respond with reduced organ growth, chlorosis and limited leaf development [151,152]. Zn shortage also reduces water uptake and disrupts tryptophan synthesis, lowering production of essential phytohormones. Additionally, Zn deficiency enhances the formation of reactive oxygen species (ROS), such as $^{\bullet}O_2^-$ and H_2O_2, by stimulating their enzymatic formation while simultaneously limiting detoxification [153].

5.3.2. Experimental

Seeds of *Solanum lycopersicum* L. cv. Mano were obtained from Rédei Kertimag Zrt. (Hungary). Seeds were surface-sterilized in 5% (v/v) NaClO for 10 minutes. Two sizes of ZnO NPs (8 nm and 45 nm) were used as seed-priming agents in a concentration of 100 mg/L. For the nano-formulation, ZnO powders were suspended in distilled water; because the initial mixtures contained large aggregates, the suspensions were sonicated twice for 30 minutes to improve dispersion, and the pH was adjusted to 5.7-5.8. For the bulk Zn treatment, $ZnSO_4$ was dissolved in distilled water, the pH was adjusted similarly, and solution volumes were set to obtain a final concentration of 100 mg/L $ZnSO_4$.

Seeds were then primed in the respective ZnO NP or $ZnSO_4$ solutions for 24 h in 15 mL tubes and kept in the dark. After priming, seeds were placed on filter paper moistened with distilled water in Petri dishes and incubated for 4 days in a growth chamber. Germinated seedlings were then transferred to 1 L containers filled with nutrient solution either containing Zn or without Zn. Plants were grown for three weeks under controlled greenhouse conditions: photon flux density of 150 µmol m^{-2} s^{-1}, a 12/12 h light-dark cycle, relative humidity of 45-55%, and a temperature of 25 ± 2 °C.

5.3.3. Method development for the LIBS elemental mapping of plant samples

Preparing plant tissues for LIBS mapping presents key challenges; mainly converting elastic, uneven surfaces into sufficiently planar samples. Achieving planarity is essential because the depth of field in tightly focused LIBS systems is very small, typically less than 50-100 µm. Several approaches to prepare plants prior LIBS analysis have been studied [104,154]. The preparation of histological cross-sections from the plant tissue could, in principle, provide a flat surface, this approach requires cutting equipment capable of producing a fresh, horizontal plane on the resin/paraffin embedded tissue. In practice, this would involve cutting the embedded block with a microtome until the appropriate depth is reached (within a few tens of µm), from which thin sections could be prepared. This is a very time-consuming procedure which requires a detailed optimization for various plant tissues [155]. Another approach is to analyze fresh plants directly. However, their high water content significantly reduces LIBS signal and makes it impossible to repeat measurements on the same sample [156].

An easy way to go is to fix the sample onto double-sided adhesive tape to glass slides. Since they can fix well the plant, as they provide an immediately flat surface once attached to a microscope slide and allow easy positioning. However, in mapping studies it was observed several drawbacks. Since the entire tape surface is adhesive, ablation debris falling back onto exposed areas readily adheres to it. Hence, in subsequent laser shots, this debris can be re-ablated, causing the recorded spectra to contain signals not only from the tape but also from redeposited plant material. The resulting elemental maps may display artifacts such as “tails” or “halos” around ablation points caused by the local melting and slight burning of the tape, compromising spectral quality and map accuracy [157]. Additionally, the adhesive tapes produced a highly complex spectrum rich in many of the same elements targeted for analysis. As a result, reliable mapping of Na, Zn, Ni, K, Li, Pb, Cd, Ca, and similar elements becomes impossible, since the strong background emission from the tape obscures the true signal from the sample [158].

The fourth possibility is the method applied and further developed in this study. It includes the embedding the dried samples in epoxy resin onto a substrate slide. Research-grade epoxy/resin formulations are commonly used for embedding medical and histological samples, and they can likewise be applied to plant tissues. A key advantage over double-sided adhesive is that epoxy not only supports the sample from below but also surrounds it laterally, providing more stable fixation. This added stability reduces fragmentation of both the sample and the mounting medium during ablation. However, working with resins requires greater care during preparation. The resin plus hardener (optional, this creates epoxy) must be applied to the substrate as a thin, level layer. After application, a brief pre-drying step is necessary to allow partial hardening; otherwise, the sample may sink into the resin, causing it to cover the tissue surface and interfere with subsequent measurements. When properly prepared, resin offers a more robust and cleaner fixation alternative for LIBS mapping of plant samples [148].

Plant materials also require careful dehydration and flattening prior to LIBS analysis. Once dried, plant tissues preserve the elemental composition of the fresh material, although concentrations appear higher due to water loss. An often overlooked but critical detail is the choice of filter paper used during pressing, since fine root hairs from the plant readily adhere to paper fibers, making it difficult to remove the plant without damage. In this experiment, the tomato seedlings were carefully removed from the Petri dishes and their roots were rinsed with Milli-Q water to remove residual growth medium. The studied plants are shown in **Fig. 28**. Seedlings were then flat-pressed 14 days using an object holder press (Kulzer GmbH, Germany) between layers of analytical filter paper sheets and polyethylene films to avoid any cross-contamination.

Figure 28. Tomato seedlings. From left to right: Control, $ZnSO_4$ treatment, 8 nm ZnO NP treatment, and 45 nm ZnO NP treatment.

Choosing a suitable resin and a suitable substrate for fixing the sample was important for us, since the material and composition of the resin and substrate are analytically sensitive factors. Much of the recorded spectrum originates from the resin itself; thus, it is essential to use a medium with a simple trace elemental composition that avoids the analytes of interest. Also the substrate composition must not interfere with the elemental mapping, since laser shots will reach the substrate surface eventually. These effects will contribute to the spectral background, so materials with minimal emission lines and minimal contamination should be selected. For most purposes, a silicon wafer should be good, as it is clean and very smooth.

The chosen resin was Technovit 7200 VLV (Kulzer GmbH, Germany), a one component, light-curing glycol-methacrylate embedding resin widely used for stabilizing biological and composite samples prior to microscopic or spectroscopic analysis. Its low temperature, photo-initiated polymerization minimizes thermal stress, while its excellent infiltration properties allow reliable embedding of both soft tissues and harder mineralized structures [159,160]. Once cured, the resin forms a hard, dimensionally stable block. Its LIBS spectra was monitored and found to be relatively a clean spectral background, with only C, H, and O as its main components.

As it was alluded to before the sample surface has to be leveled as much as possible. If it is not done properly, the sample surface will be out of focus during scanning and the LIBS signal will be gradually smaller and smaller towards the edges of the sample. One solution is to level the sample during embedding preparation as much as possible. Hence, to improve sample planarity and ensure the formation of a thin, uniform resin layer, the embedding procedure was combined with the EXAKT 402 (Kulzer GmbH, Germany) precision adhesive press. This device applies a uniform, adjustable laminar pressure across the sample during the early curing phase, ensuring that the resin forms a flat, controlled-thickness layer and preventing the plant from sinking or bending within the resin.

The final, developed protocol consisted of the following steps. A microscope slide was covered with a transparent tape (this will be the second slide). This slide was positioned under the acrylic block of the device in order to be fixed by the applied vacuum. Afterwards, 2-3 drops of resin were added onto the middle of a previously cleaned silicon slide. Then, the plant was carefully placed on top of this and allowed the resin to be spread within the plant for a few seconds. 3-4 more drops of resin were added and 300 µm aluminum spacers were put on both sides of the slide; these determined the thickness of the embedded block. Afterwards, the prepared sample was placed on the stage of the adhesive press, just below the second slide. Then slowly and precisely the prepared sample and second slide were joined with the help of a fixed weight of the press. Afterwards, the sample was exposed to light; this resin has the advantage to provide an even adhesive layer that would not polymerize until exposed to blue light. This way, any bubbles in the adhesive layer could be dealt with before becoming permanent. The transparent acrylic block allows to see the spread of the resin and view any bubbles that may arise prior to beginning polymerization. The polymerization step takes 15 min.

Another point to consider is the number of layers needed to completely ablate the sample. The biological specimen (even if they are flat-dried) will be thicker than the depth of a single-shot ablation crater, which mean that the embedded block will have to be mapped in multiple layers. Since typical ablation craters are on the order of tens of microns, and considering that the final embedded plant has a thickness of 300 µm, this means that the minimum number of layers will be ten or more. To estimate the number of layers, an experiment was done, first by casting the resin in the same thickness that was used for the plant embedding using the silicon slide. Repeated laser shots using 10 mJ pulse energy were delivered on the same location, varying the spot size from 40 µm and 100 µm. The number of shots were counted until a steady signal at the Si 288.16 nm emission line was detected; indicating that laser has reached to the "bottom" of the resin (**Fig. 29**).

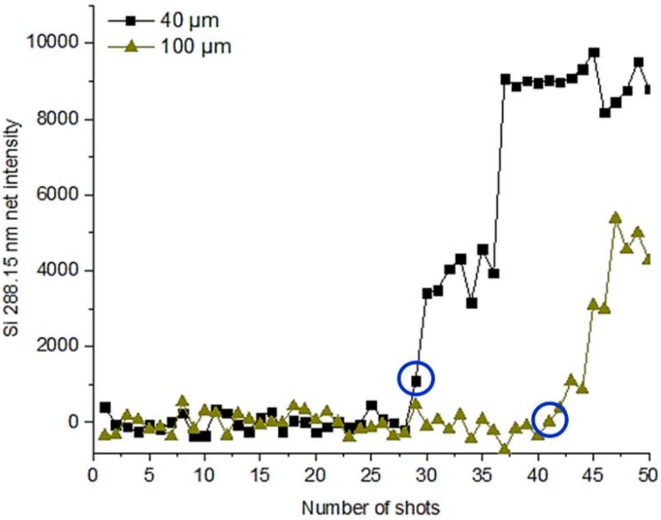

Figure 29. Silicon emission line as function of number of shots employing 40 µm and 100 µm laser spot size on the 300 µm thick embedded resin. Pulse energy 10 mJ, repetition rate 1 Hz.

As can be observed, the number of laser shots required to reach the total thickness of the embedded resin was 28 and 41 for the 40 µm and 100 µm spot sizes. Considering the total thickness, this meant that each ablated layer removes, on average, 10.7 µm and 7.3 µm per layer of resin for the 40 µm and 100 µm respectively. It is worth considering however that the ablation process also leaves behind a significant amount of debris, and subsequent ablation layers reablate this debris. This suggests that the complete removal of the debris between the layers may be necessary.

Another, more detailed experiment was also conducted using an embedded plant and performing a full area mapping, employing a 40 µm spot size. This time, after each ablation layer, the debris was removed from the surface. The sample holder was taken out without removing the sample and a blow of pressurized air was applied to remove the generated debris from the resin and plant, "touchings" of cellotape were also around the edges of the ablated area, avoiding plant parts. Cleaning of the ablation cell was also performed at the same time, considering that the top quartz window on the ablation cell can get dirty during mapping. This poses a problem because these deposits can absorb laser light, which not only decreases measurement sensitivity, but also can cause pits and stains. The ablation top window was removed after each second ablation layer and cleaned with analytical purity isopropanol and acetone using cotton-swabs and lint-free cleaning wipes (Kimwipes).

During this mapping experiment, Si, Na and Ca emissions were monitored. Results are shown in **Fig. 30**. One of the striking observation that can be made is that the simultaneous evolution of the Na and Ca signal, which indicates the analysis of the plant tissue, occurred much earlier, peaking in around the second and third layers. Following this, these signals decayed and practically disappeared by the seventh and eight layers. The Si, which is also present in plants, at lower concentrations than Na and Ca, was also detected in the early layers, but it peaked in the seventh layer, when the silicon substrate was reached. Therefore it was concluded that the application of seven ablation layers is sufficient for mapping plants embedded in a 300 µm thick glycol-methacrylate resin, if cleaning of the sample surface is employed.

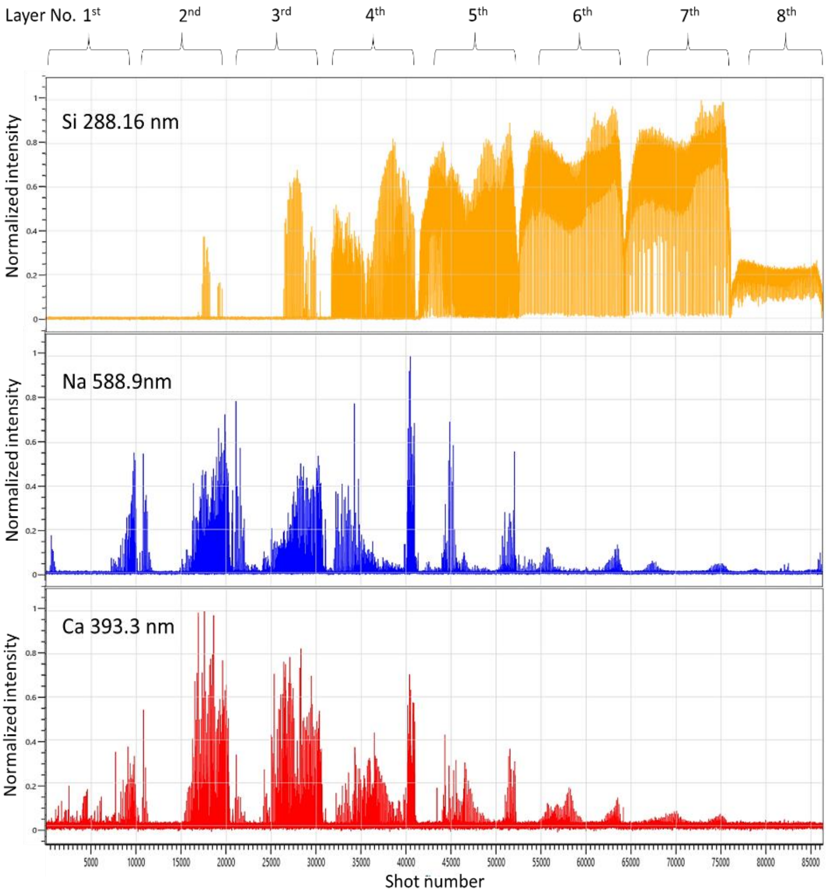

Figure 30. Number of layers as function of the Si, Na and Ca emission lines. x-axis represents the number of shots, y-axis represents the normalized intensity according to the indicated emission line. On the top, the respective number of layers are indicated for each stepwise-scan.

Finally, the elemental maps of all treated tomato plants were collected by the above procedure. The embedded plants were photographed using an optical microscope and LIBS measurements were performed using a J-200 LIBS system, employing a 10 mJ pulse energy, 40 µm spot size (~125 µm spatial resolution), 1.05 ms integration time and 0.5 µs gate delay. Stepwise scanning was carried out across the entire plant surface (approximately 15-20×50-60 mm) without overlapping spots, collecting a single-shot LIBS spectrum at each position. Seven ablation layers were recorded per plant in order to ablate the whole plant sample; spectra from each vertical position were then summed to obtain enough spectral data for subsequent processing and map generation. Zinc elemental maps were created from the net intensity of the Zn I 472.21 nm emission line. Generated maps can be seen in **Fig. 31**. These maps provide a clear visualization of the spatial distribution of major elements within the tomato seedlings and demonstrate that the sample preparation and mapping procedure preserved both structural integrity and chemical information. The Na maps reveal strongly localized accumulations, mainly along the primary root and occasionally near the root tip, reflecting the natural mobility of sodium and its uptake dynamics from the growth medium. In contrast, Ca shows a more continuous distribution across the entire root system, outlining major anatomical features and indicating its role as an immobile structural nutrient in cell walls. When comparing different treatments, seedlings primed with ZnO NPs appear to exhibit altered Na and Ca patterns, suggesting treatment-dependent effects on nutrient uptake and internal translocation, while Zn-deficient plants generally display weaker elemental signals consistent with reduced growth and nutrient transport.

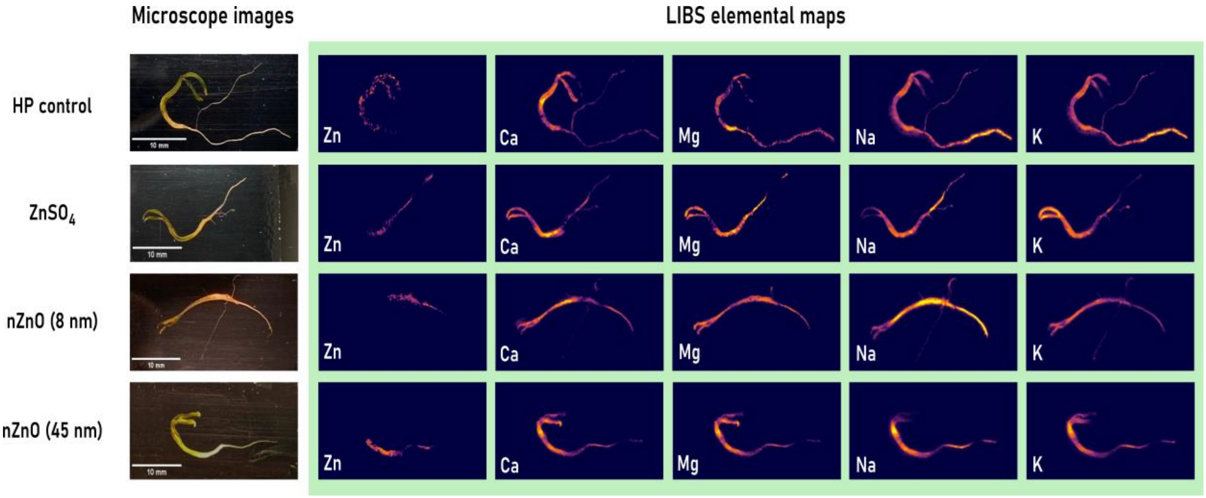

Figure 31. LIBS elemental maps demonstrating the in-planta distribution of selected elements in *Solanum lycopersicum* L. cv. Mano seedlings cultivated with 0 (Control) and 100 mg·L^{-1} of 8 nm or 45 nm ZnO NPs for 21 days. The pixel color in the maps shows the net emission intensity of the given spectral line of the element, which is proportional with the concentration (e.g. deep blue corresponds to a very low concentration, and light yellow corresponds to a high concentration). Figure reproduced from own publication [P10].

6. BOOSTING LIBS PERFORMANCE USING A FIBER LASER

Nanosecond-pulsed fiber lasers based on the master oscillator power amplifier (MOPA) architecture were primarily developed recently for industrial use. Modern MOPA fiber lasers allow extensive tuning of pulse duration, pulse shape, pulse energy distribution, and pulse repetition rate, enabling tailored laser-matter interaction regimes [27,28]. It has recently been also recognized as potentially attractive excitation sources for LIBS due to their compactness, robustness, high repetition rate capability, and flexible pulse parameter control [30,161-163]. These features are particularly relevant for LIBS, where plasma formation, excitation efficiency, background emission, and analytical performance strongly depend on the temporal structure of the laser pulse and on pulse-to-pulse interactions.

In this work, the effects of temporal pulse engineering in fiber-laser-induced breakdown spectroscopy are systematically investigated in both single-pulse and multi-pulse excitation regimes, using a modern, ns-pulsed MOPA fiber laser source. In the single-shot configuration, LIBS performance is studied as a function of pulse duration, pulse energy, and pulse shape, with particular emphasis on the relative roles of the pulse head and pulse tail in plasma generation and emission efficiency. In the multi-pulse regime, double- and multi-pulse LIBS experiments are performed to examine the influence of interpulse delay, pulse energy balance, and consecutive pulse interactions at repetition rates extending into the MHz range for signal enhancement.

6.1. Background

Early demonstrations of fiber laser LIBS established that nanosecond fiber lasers can generate plasmas with low continuum background and useful analytical performance, even at relatively modest pulse energies [164]. Subsequent studies confirmed that analytically useful signals can be achieved on metallic samples [29,165,166]. These investigations however relied on fixed laser settings and did not exploit the unique pulse-shaping capabilities inherent to the MOPA architecture. Only a small number of reports have addressed how variations in pulse duration, pulse shape, and repetition rate influence plasma properties and spectral emission [167,168], leaving key questions unanswered regarding optimal pulse configurations and underlying interaction mechanisms.

One aspect that remains insufficiently understood is the role of extended nanosecond pulse durations and programmable temporal pulse profiles in single-shot LIBS. Unlike conventional short nanosecond pulses, long and structured pulses distribute energy over hundreds of nanoseconds or even microseconds, fundamentally altering plasma evolution, laser-plasma coupling, and background formation. In particular, the relative contributions of the initial high-power pulse head and the subsequent low-intensity pulse tail to plasma ignition and sustained emission have not been comprehensively examined. Understanding these effects is essential for identifying pulse configurations that maximize emission intensity while minimizing continuum background, especially under zero or minimal detector gating conditions.

In parallel, the high repetition rate capability of modern fiber lasers reaching hundreds of kilohertz or the megahertz regime, offers a unique platform for implementing double- and multi-pulse LIBS in just a coaxial geometry. While DP- and MP-LIBS are well known to enhance signal intensity and precision, most reported implementations rely on separate laser sources or interpulse delays comparable to the plasma lifetime [11,17,51,52,169]. In contrast, fiber lasers enable closely spaced pulses in trains with controlled interpulse delays and pulse energy ratios, opening new regimes where consecutive pulses interact primarily with a dynamically modified surface rather than with an existing plasma. The implications of such pulse sequences, particularly when using relatively long nanosecond pulses with low background emission, have not yet been systematically explored.

The present work addresses these gaps by providing a unified investigation of fiber laser-based LIBS, covering both single-pulse and multi-pulse performances. In the single-shot configuration, I examined the effects of pulse duration, pulse energy, and pulse shape over a wide range, with special emphasis on the distinct roles of the pulse head and pulse tail in plasma generation and emission efficiency. In the multi-pulse regime, I explored double- and multi-pulse LIBS using high repetition rate pulse trains, focusing on the influence of interpulse delay, pulse energy balance, and the number of consecutive pulses on signal enhancement and stability.

6.2. Experimental

A TruPulse Nano 5020 compact MOPA fiber laser with an emission wavelength of 1062 nm was employed. The general characteristics of this laser source is described in section 4 of this dissertation, therefore only the most relevant features are mentioned here. The laser provides 48 pre-programmed temporal pulse profiles with pulse durations ranging from 8 to 2000 ns, which results in waveform-dependent pulse energies. Apart from single pulses, bursts of pulses with repetition rates is adjustable from 1 kHz up to 4 MHz can also be released. As illustrated in **Fig. 32**, the temporal profiles of the applied laser waveforms are characterized by a pronounced initial intensity peak followed by an extended, lower-intensity tail. For pulse durations up to approximately 30 ns, the temporal profiles are fully symmetric, indicating that the rising and falling edges of the pulse are governed by the physical processes associated with the rapid release and depletion of stored energy in the gain medium. Beyond this time scale, the pulse shape becomes increasingly asymmetric while the leading edge remains steep, the trailing edge exhibits a gradual decay, reflecting slower, pump-limited emission processes.

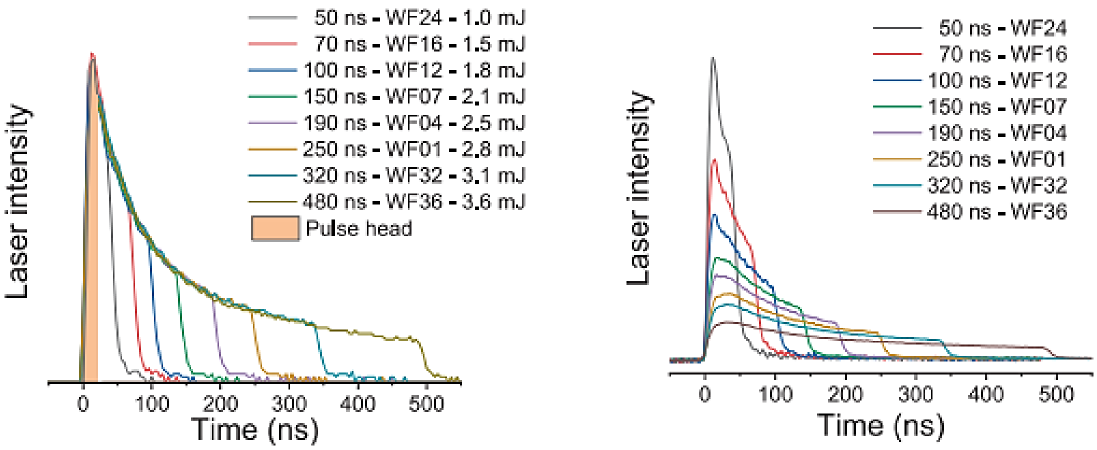

Figure 32. Temporal pulse profiles corresponding to the applied waveforms are shown for their maximum pulse energies (left) and for a fixed total pulse energy of 1 mJ (right). The shaded area in the left panel marks the pulse head region. Figure reproduced from own publication [P4].

Based on this, the first 30 ns of the laser pulse was defined as the pulse head, whereas the remaining part is referred to as the pulse tail. Accordingly, the energy contained within the initial 30 ns is defined as the pulse head energy, while the energy delivered during the subsequent, elongated portion of the pulse is defined as the pulse tail energy. Each contributing differently to plasma formation and excitation.

Fiber laser-based LIBS experiments were carried out with a gate delay of zero and 50 µs gate width. Spectrum collection was performed by an Echelle spectrometer in the range of 220 to 629 nm, with a resolving power around 10000. Double- and multi-pulse LIBS experiments were carried out in the co-axial mode. In some experiments, the J-200 LA/LIBS system was used, employing a 0.5 µs gate delay and 1 ms gate width. The pulse energy was set to 15 mJ with a 40 µm laser spot size. All LIBS measurements were performed under ambient air. Experiments were performed on silicon wafer substrates and stainless steel reference materials (BC/SS-CRM 401/2- and 405/2; BAS Ltd, UK).

Plasma temperatures were estimated from the recorded LIBS spectra using the Boltzmann plot method [170]. This method assumes that the populations of the excited atomic states follow a Boltzmann distribution, allowing the plasma temperature to be derived from the relative intensities of emission lines originating from different excitation energies. Excitation temperature calculations were performed only for silicon samples. Due to spectral overlap and interference, only three well-resolved Si I lines were suitable for this analysis (Si 263.13, 298.76 and 390.55 nm).

6.3. Single-pulse fiber laser LIBS performance

6.3.1. Plasma diagnostics

The plasma emission lifetime and temperature were characterized for a series of pulse shapes with varying durations and energies on a silicon sample. Please note that plasma emission lifetime, which characterizes the duration of light emission from the plasma is longer than plasma lifetime (during which the Debye plasma conditions are fulfilled). In all cases, the measured emission lifetimes remained in the microsecond range, with maximum values not exceeding approximately 3 µs. This is substantially shorter than the tens of microseconds typically reported for plasmas generated in conventional nanosecond LIBS using higher pulse energies [22], indicating that the lower-energy, long duration fiber laser pulses produce plasmas of reduced density and faster radiative decay.

As shown in **Fig. 33a**, the plasma emission lifetime increases monotonously with pulse energy for short pulses, which is expected due to the higher peak power and increased plasma excitation. For longer pulse durations, despite higher total pulse energies (up to 5 mJ), the plasma emission lifetime decreases, particularly for the 2000 ns pulse, where it drops below 2.5 µs. This suggests that the elongated pulse tail contributes less to sustaining emission and that the early pulse head is more critical for plasma generation and persistence. The short emission lifetimes observed also suggest that fast spectrometers with µs integration times are more suitable for collecting fiber laser-induced LIBS spectra. In terms of plasma temperature, **Fig. 33b** shows that the excitation temperature remains relatively constant at approximately 9000 ± 1000 K across all pulse shapes, energies and durations. These findings highlight the dominance of the pulse head in generating plasma emission and indicate that pulse tail energy primarily influences plasma persistence rather than excitation temperature. The obtained temperatures are consistent with previously reported values for plasmas generated by long nanosecond pulses and are significantly lower than those typically observed in classical LIBS experiments employing higher pulse energies and shorter pulse durations [37,171].

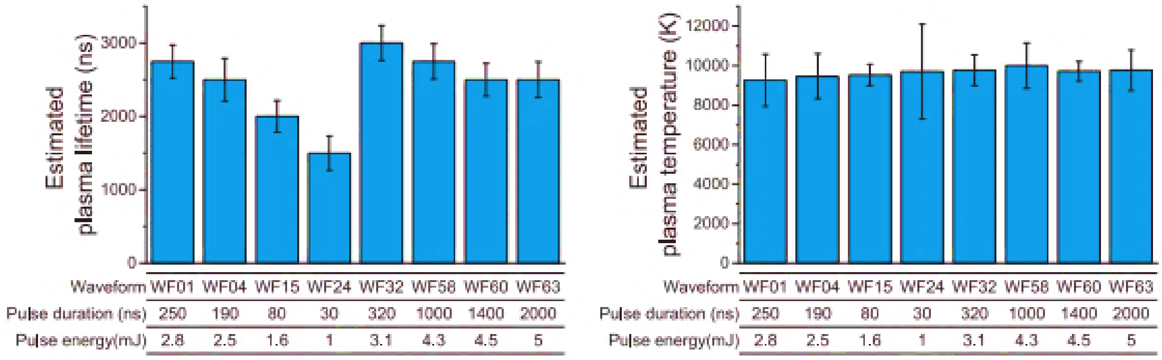

Figure 33. Plasma emission persistence times for various pulse shapes and durations (left) and the corresponding excitation temperatures determined by Boltzmann analysis (right) are shown. Error bars represent the standard deviation of the measurements Figure reproduced from own publication [P4].

Fig. 34 shows that at constant pulse energy, plasma emission strongly depends on pulse duration. Shorter pulses generate higher initial emission intensities and stronger plasma emission, whereas longer pulses result in weaker and more rapidly decaying emission. For the 1000 ns pulse, the total emission intensity decays to 1% of its initial value within approximately 800 ns, while for the 190 ns pulse this decay occurs after more than 1000 ns, indicating a longer plasma lifetime. This behavior is attributed to the higher irradiance of shorter pulses, which enhances ablation efficiency and the generation of excited species. In contrast, distributing the same energy over longer durations reduces peak power and limits the effectiveness of the pulse tail in sustaining plasma emission. These trends are consistent with the spectral results, where the Fe II 247.6 nm line intensity decreases monotonically with increasing pulse duration. Overall, the results confirm that plasma emission efficiency in fiber laser-based LIBS is governed primarily by pulse duration dependence rather than by the total pulse energy.

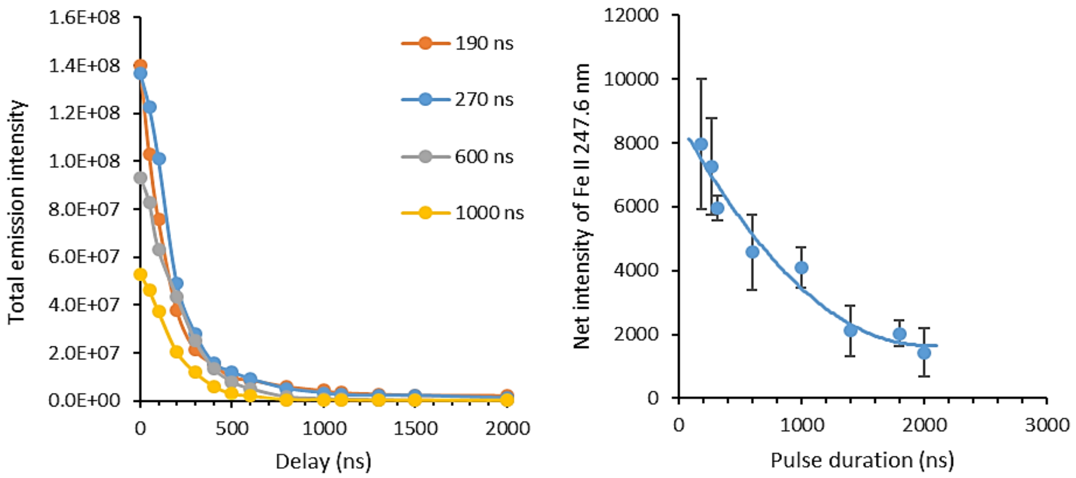

Figure 34. Temporal evolution of the total plasma emission intensity for pulse shapes of same energy (2.5 mJ) but different durations used for LIB plasma generation on a steel sample (left), and the corresponding intensity of an Fe emission line as a function of pulse duration (right). Figure reproduced from own publication [P4].

On the other hand, higher pulse energy results in higher spectral line intensities for pulses of the same duration, consistent with classical LIBS behavior (**Fig. 35**). At short and intermediate pulse durations, the line intensity exhibits a plateau, which can be attributed to reduced plasma shielding in long ns pulses [29]. For sufficiently long pulses, the irradiance becomes too low for effective ablation and excitation, leading to an overall decrease in emission intensity. The pulse-duration threshold beyond which this decrease occurs depends on pulse energy, appearing at approximately 190-200 ns for 1 mJ pulses and at 270-320 ns for 2-2.5 mJ pulses.

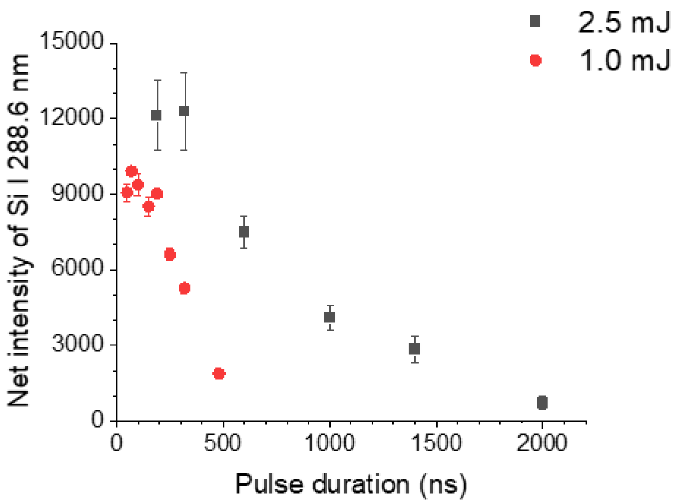

Figure 35. Effect of pulse duration on the intensity of the Si I 288.16 nm emission line for two different pulse energies (2.5 and 1.0 mJ) used for plasma generation on a silicon sample. Error bars indicate the standard deviation from ten replicate measurements. Figure reproduced from own publication [P4].

The above results indicate that extending the pulse duration beyond a certain limit does not further improve LIBS analytical signals. This observation suggests that not only the total pulse duration, but also the temporal distribution of energy within the pulse (pulse head and pulse tail), influences the emission intensities. To investigate this effect, experiments were performed in which the pulse head energy was kept constant, while the duration and energy of the pulse tail were systematically varied. The pulse tail length was adjusted between 0 and 1970 ns, corresponding to tail energies ranging from 0.0 to 4.4 mJ. Several pulse head energies were examined in the range of 0.15-0.58 mJ. The resulting net intensities of the Si I 288.16 nm emission line recorded from a silicon sample are shown in **Fig. 36**.

As shown in **Fig. 36a**, higher energies of the pulse tail leads to a pronounced increase in line intensity for all investigated pulse head energies. This demonstrates that the energy delivered in the pulse tail contributes effectively to plasma excitation and ablation. Notably, plasma formation and measurable emission could be achieved when a sufficiently energetic pulse tail was applied even in cases where the pulse head alone was too weak to efficiently ignite the plasma. Nevertheless, the energy of the pulse head has a dominant influence on the signal level, at identical pulse tail energies, higher pulse head energies consistently produce significantly stronger emission, indicating more efficient plasma ignition and improved coupling of the tail energy into the plasma. With further increase of the pulse tail energy, the emission intensity reaches a maximum at approximately 1.4-2 mJ tail energy, depending on the applied pulse head energy. Beyond this range, the signal either saturates or shows a slight decrease. This behavior indicates that, although the pulse tail can enhance the LIBS signal by sustaining ablation and excitation, there is a limit beyond which additional tail energy becomes inefficient due to reduced irradiance and weakened laser-plasma coupling in the expanding plume.

When the same data are plotted as a function of the total pulse duration (**Fig. 36b**), it becomes evident that signal stagnation occurs at pulse durations of approximately 250-320 ns for all investigated pulse head energies. The fact that this threshold duration is largely independent of pulse energy suggests that it is governed by plasma evolution dynamics rather than by the absolute energy delivered. After this time interval, the plasma has expanded sufficiently that further energy deposition does not lead to increased emission. Based on these results, it can be concluded that optimal single-pulse LIBS performance with this fiber laser source is achieved by employing the highest possible pulse head energy while limiting the total pulse duration to approximately 320 ns.

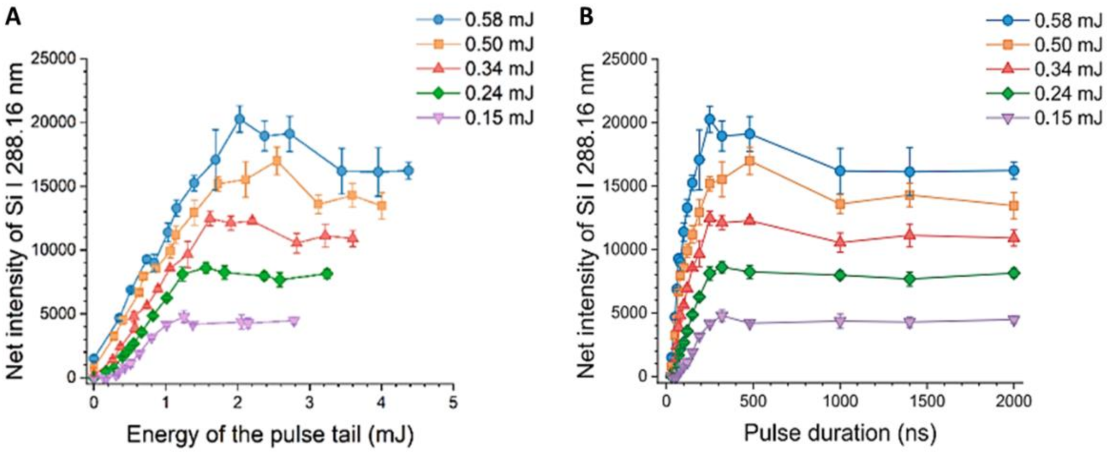

Figure 36. Net intensities of the examined Si emission line plotted as a function of pulse-tail energy (A) and total pulse duration (B) for plasma generated on a silicon sample. Error bars represent the standard deviation derived from three parallel measurements. Figure reproduced from own publication [P4].

6.3.2. Quantitative performance

I also performed a comparative assessment of the quantitative performance of the single-pulse fiber laser LIBS setup against the commercial ASI J-200 LIBS instrument, where the latter has a higher intensity laser source (higher pulse energy, shorter pulse duration). A stainless steel reference material series were used as samples. Calibration curves for Cr and Al exhibited similar linearity and signal scatter for both systems (**Fig. 37**), while LODs were comparable or even favouring the fiber laser system in three out of the five investigated elements (Mn, Cu, and V) as can be seen in **Table 3**.

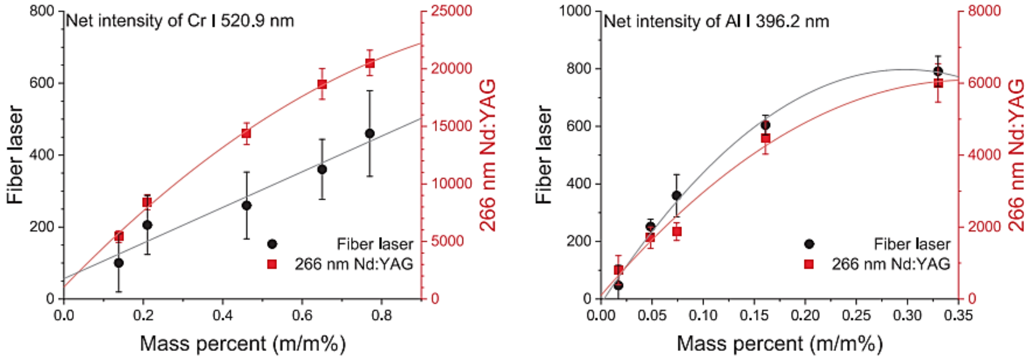

Figure 37. Calibration curves for a chromium and an aluminum emission line recorded in a stainless steel reference material series, using the fiber laser system and the commercial ASI J200 LIBS system. Figure reproduced from own publication [P4].

Element	Wavelength (nm)	Fiber laser basedLIBS system		Nd:YAG laser basedLIBS system	
		LOD (m/m%)	RMSE (m/m%)	LOD (m/m%)	RMSE (m/m%)
Mn	403.0	0.51	0.16	0.08	0.24
Cr	520.9	0.50	0.06	0.04	0.02
Cu	327.4	0.05	0.02	0.03	0.01
Al	396.2	0.04	0.04	0.04	0.04
V	413.2	0.17	0.02	0.28	0.07

Table 3. LOD values for selected elements measured in stainless steel. Reproduced from own publication [P4].

6.4. Multi-pulse fiber laser LIBS performance

As it was previously mentioned, this fiber laser can operate at such high pulse repetition rates (PRR, up to 4 MHz) that the interpulse delay in the pulse bursts falls into the microsecond or even sub-microsecond range. This makes it a potentially suitable laser source for coaxial double- or multi-pulse LIBS (DP-LIBS or MP-LIBS) signal enhancement schemes. It has to be considered however that due to the specialities of this source, the energy of pulses in a pulse train is not constant and depends strongly on the repetition rate and pulse duration, as shown in **Fig. 38a.** At low PRRs, the energy of consecutive pulses increases shot-to-shot until a stable value is reached (after approximately ten pulses), indicating a gradual establishment of steady-state gain conditions in the amplifier. As the PRR is increased, the stabilized pulse energy initially rises, reaching a waveform-dependent maximum. For example, the highest stabilized energy is observed at around 60 kHz PRR for the 190 ns duration waveform. At the same time, as it is shown in **Fig. 38b,** the stabilized pulse energy decreases beyond this PRR, as the pump laser can no longer replenish the gain medium sufficiently between pulses. Longer pulses exhibit higher stabilized energies because they interact with the gain medium for a longer time and extract stored energy more efficiently. However, longer pulses also deplete the gain more strongly and therefore reach their maximum stabilized energy at lower PRRs, beyond which pulse energy decreases due to insufficient gain recovery. At sufficiently high PRR, the pulse energies of all investigated waveforms converge toward low values. These results indicate that, for each pulse waveform, a specific PRR exists at which the pulse energy remains stable throughout the pulse train.

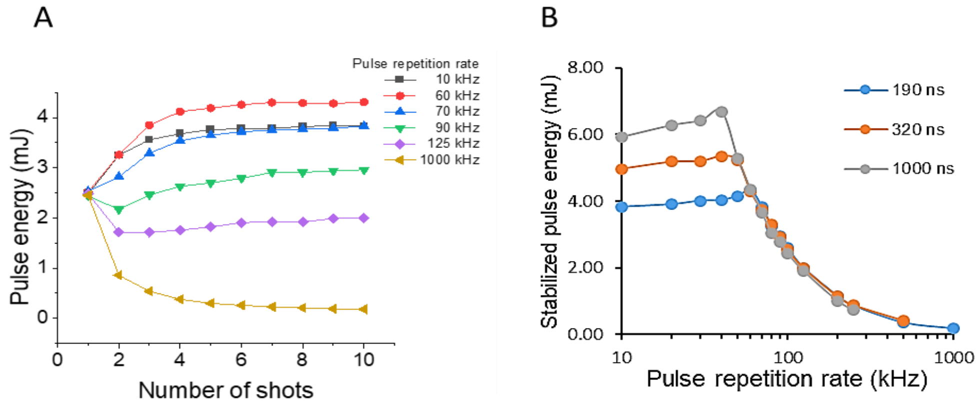

Figure 38. A) Energy of consecutive laser pulse trains (“burst mode”) for a pulse duration of 190 ns at different PRRs. B) Stabilized pulse energy as a function of PRR for different waveforms of various durations. Figure reproduced from own publication [P5].

6.4.1. LIBS using two consecutive laser pulses

The first DP-LIBS experiments using the fiber laser were performed on a silicon sample with laser pulses of 50 ns duration and an equal, 0.8 mJ energy. In the DP-LIBS configuration, the second laser pulse was applied with an interpulse delay of 10 µs relative to the first pulse. The detector gate delay was adjusted to zero when the Si analytical signal from the first pulse was recorded, and it was shifted to the arrival of the second laser pulse when the signal from second pulse was tested. As is shown in **Fig. 39**, the second pulse provides a substantially enhanced analytical signal. Most emission lines exhibit approximately a twofold increase in intensity in the DP-LIBS spectrum relative to the SP-LIBS case.

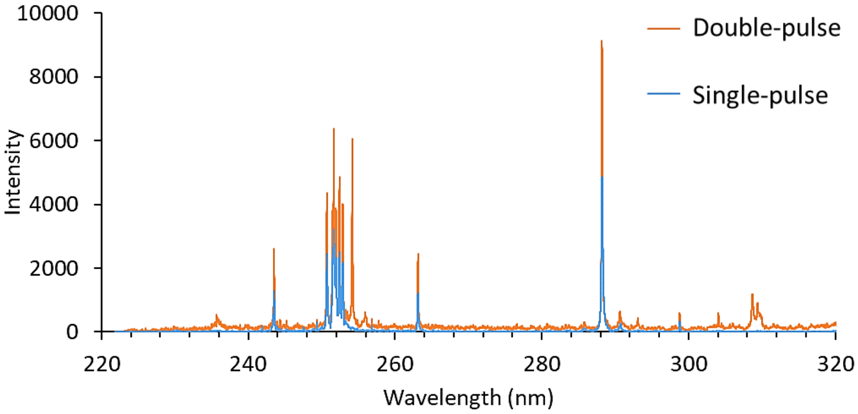

Figure 39. Comparison of single-pulse and double-pulse LIBS spectra acquired from a silicon sample using 50 ns laser pulses with 0.8 mJ pulse energy. In the DP configuration, the interpulse delay was set to 10 µs. Figure reproduced from own publication [P5].

The applied interpulse delay of 10 µs is significantly longer than the measured plasma emission lifetime. Consequently, direct laser-plasma interactions, such as plasma reheating by absorption of the second pulse, can be excluded. This implies that the observed signal enhancement does not originate from mechanisms commonly associated with short-delay coaxial DP-LIBS, where the second pulse couples directly into an existing plasma. Instead, the enhancement can be attributed to indirect processes initiated by the first pulse. These include thermal preconditioning of the sample surface through radiative and conductive heat transfer from the initial plasma, which lowers the effective ablation threshold for the second pulse. In addition, the second pulse contributes directly to material removal, as co-axial follow-up pulses are inherently ablative. Furthermore, the presence of a transient low-pressure region behind the shockwave generated by the first pulse can facilitate enhanced ablation during the arrival of the second pulse [11,18,169]. The plasma temperature calculations performed for both SP- and DP-LIBS plasmas achieved comparable excitation temperatures of 5750 ± 60 K. The absence of a measurable temperature increase in the DP-LIBS case further supports the conclusion that plasma reheating does not play a significant role under the applied experimental conditions. Instead, the enhanced emission intensity observed in **Fig. 39** is primarily a consequence of increased ablated mass and improved excitation efficiency resulting from surface preconditioning effects induced by the first pulse.

The effect of the duration of longer than usual interpulse delays were also tested. These effects can be seen in **Fig. 40**., where the decrease in emission intensity with increasing interpulse delay is due to the gradual disappearance of the first-pulse-induced enhancement mechanisms. As the delay increases, the plasma cools and expands, the heated surface layer relaxes, and the ablation crater stabilizes, leading to reduced coupling for the second pulse. However, because long-nanosecond fiber laser pulses produce relatively cold plasmas, the enhancement mechanism is dominated by surface modification rather than plasma reheating. This makes the DP-LIBS enhancement tolerant to timing, with noticeable benefits persisting even at delays as long as 100 µs.

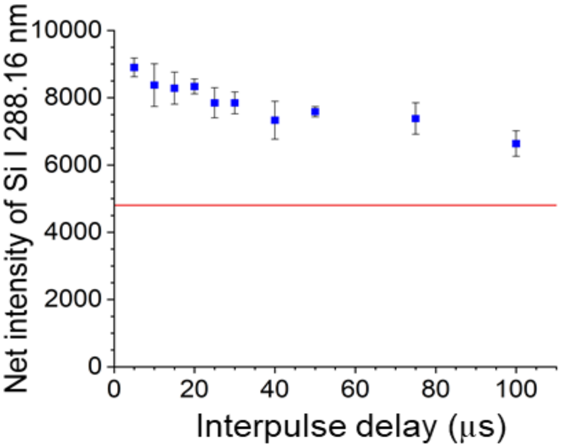

Figure 40. Silicon emission intensity by DP-LIBS recorded at the arrival of the second pulse as function of interpulse delay. The SP-LIBS signal is shown as a horizontal reference line. All pulses were 50 ns duration and 0.8 mJ pulse energy. Error bars indicate standard deviations from three measurements. Figure reproduced from own publication [P5].

As it was previously discussed, at fixed pulse energy, increasing pulse duration lowers SP-LIBS intensity because the laser irradiance decreases. In the next experiment I tested whether the same trend applies to DP-LIBS. The pulse energy was fixed at 0.6 mJ for both pulses and the interpulse delay at 10 µs; varying the duration of the second pulse from 50 to 320 ns. Thus, any changes in signal must originate from changes in pulse duration (irradiance). **Fig. 41** shows that increasing pulse duration results in a systematic decrease of both SP- and DP- LIBS intensities, reflecting the reduced irradiance and weaker plasma formation of longer pulses. Consequently, the highest absolute DP-LIBS signal is obtained for the shortest pulse duration (50 ns). The DP-to-SP signal enhancement factor remains approximately constant across most durations, with a maximum observed at 190 ns due to the faster decline of the SP signal relative to the DP signal. This demonstrates that optimization for maximum DP-LIBS enhancement does not necessarily coincide with optimization for maximum analytical signal intensity.

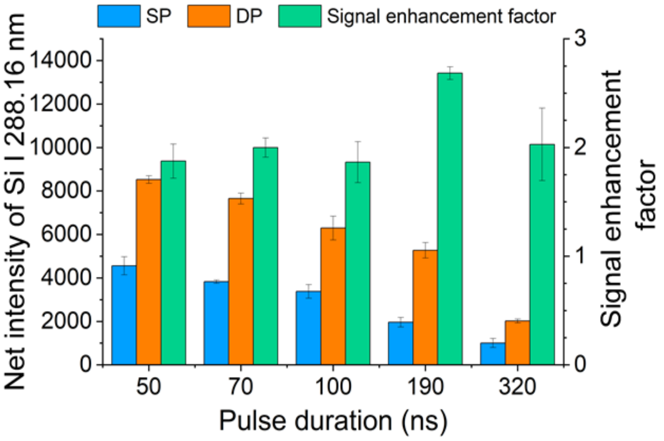

Figure 41. Silicon LIBS signal intensities generated by the first (SP) and second (DP) laser pulses (left axis), together with the corresponding DP-LIBS signal enhancement factor (right axis), measured for different pulse durations at a constant pulse energy of 0.6 mJ and an interpulse delay of 10 µs. Error bars indicate the standard deviation from three replicate measurements. Figure reproduced from own publication [P5].

Since the employed fiber laser allows independent control of the energies of consecutive pulses, the effect of varying the pulse energies in double-pulse bursts on the DP-LIBS signal was also investigated. I kept the pulse duration (100 ns) and interpulse delay (10 µs) constant. Two complementary experiments were carried out: *i*) **Fig. 42** the energy of the first pulse was varied from 0.5 to 1.8 mJ, while the second pulse energy was kept constant at 1.0 mJ; *ii*) **Fig. 43** the energy of the first pulse was fixed at 0.8 mJ, while the second pulse energy was varied from 0.7 to 1.8 mJ.

In **Fig. 42**, increasing the first pulse energy leads to only a modest increase in the DP-LIBS signal. Even when the energy of the first pulse is increased by more than a factor of three, the resulting signal enhancement at the second pulse is only roughly 10-15%. In contrast, **Fig. 43** reveals a strong and nearly linear dependence of the DP-LIBS signal on the energy of the second pulse. Increasing the second pulse energy by a factor of approximately three results in a nearly threefold increase in the LIBS signal. This indicates that, under these conditions, the primary role of the first pulse is to ablate material and precondition the sample surface, while the second pulse arrives after the plasma has decayed, interacts with a preheated, weakened surface and is therefore much more efficient at ablation and excitation.

Plasma temperature calculations showed no significant variation with pulse energy, remaining at approximately 5750 K, suggesting that the observed signal enhancement is mainly governed by ablation-related processes rather than plasma reheating. This is consistent with previous studies showing that noticeable plasma temperature increases require much larger energy differences between the two pulses than those applied here [172,173]. Also, the use of relatively long laser pulses used in this study further favor sample heating and ablation efficiency over plasma temperature elevation.

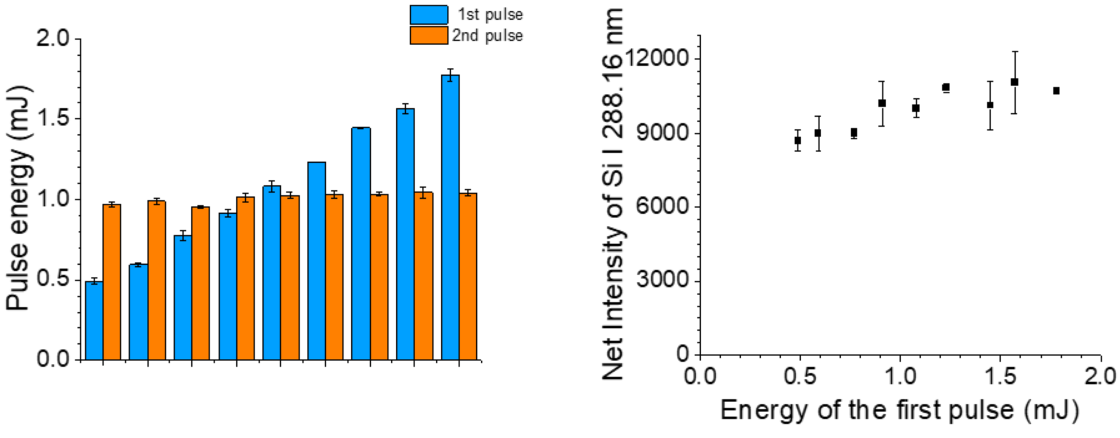

Figure 42. Energies of the first laser pulse applied during the investigation (left panel) and the corresponding Si DP-LIBS signal intensities recorded from the second pulse (right panel). Error bars indicate the standard deviation from three replicate measurements. Figure reproduced from own publication [P5].

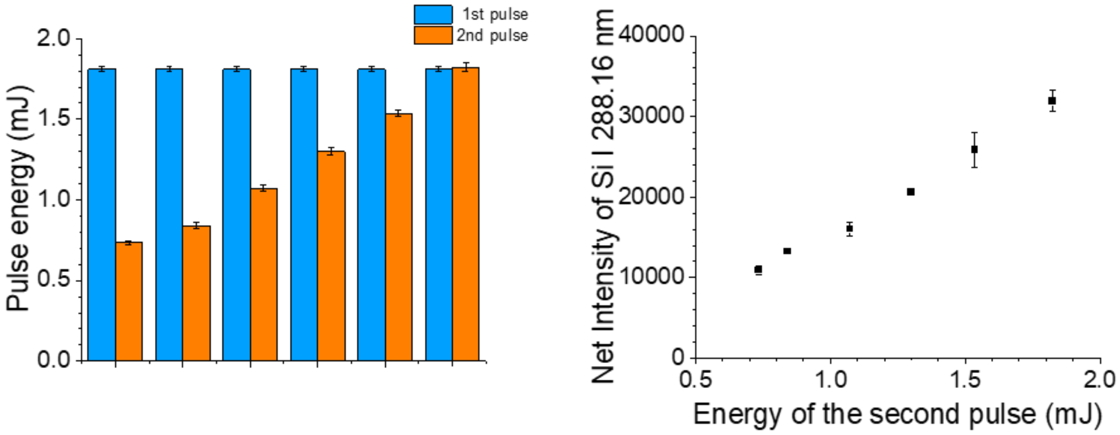

Figure 43. Energies of the second laser pulse applied during the investigation (left panel) and the corresponding Si DP-LIBS signal intensities recorded from the second pulse (right panel). Error bars indicate the standard deviation from three replicate measurements. Figure reproduced from own publication [P5].

I also evaluated whether DP-LIBS provides a real quantitative analytical advantage over SP-LIBS. To do this, certified stainless-steel reference materials with known concentrations of Cr, Ni, and Cu were analyzed and calibration curves were constructed for both SP and DP operation. Since the goal was to achieve the best signal, 320 ns pulse duration (WF32) was selected because it gave strong, stable emission. Also, since the second pulse energy was identified as the dominant factor in DP-LIBS signal enhancement, a 40 kHz repetition rate was chosen because it maximizes the energy of the second pulse. Long integration time was set for capturing emission from both plasmas. As an illustration, a calibration for chromium is shown in **Fig. 44**. DP-LIBS produced a much larger increase in signal intensity; the slope (sensitivity) is 4-5 times higher than that of SP-LIBS. This sensitivity enhancement resulted in significantly lower LODs for DP-LIBS. The LODs improved from 0.49% to 0.14% for Cr, from 0.04% to 0.02% for Al, and from 0.05% to 0.01% for Cu. These results demonstrate that, under optimized conditions, fiber laser-based DP-LIBS provides improved quantitative performance relative to SP operation.

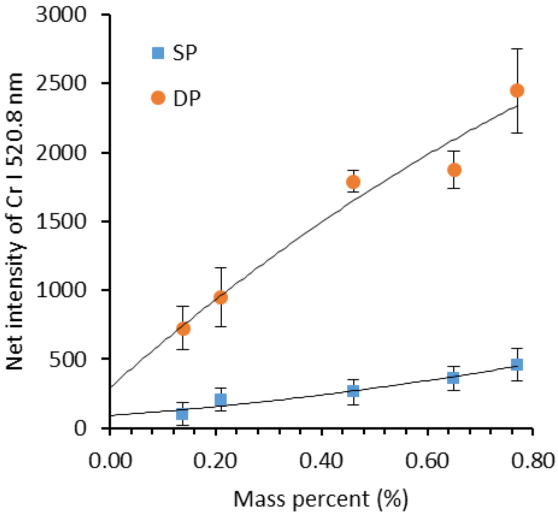

Figure 44. Calibration plot for the Cr I 520.8 nm emission line obtained using SP-LIBS and DP-LIBS. For the DP-LIBS measurements, the emission signals from both pulses were integrated. Figure reproduced from own publication [P5].

6.4.2. LIBS using more than two consecutive laser pulses

I also investigated whether applying more than two pulses further enhances the LIBS signal (MP-LIBS). Experimental conditions, such as pulse energy of 1 mJ with 50 ns duration and 10 µs interpulse delay were kept constant. According to **Fig. 45a**., MP-LIBS results showed that the second, third, and fourth laser pulses generate similarly enhanced plasma emission compared to SP-LIBS, due to interaction with a preconditioned surface that is already modified by previous ablation, resulting in improved and nearly identical coupling conditions. In contrast, the fifth pulse sees a surface that is either significantly cratered (causing defocusing) or is partially molten due to accumulated heat. Both effects reduce ablation efficiency, leading to the observed drop in LIBS intensity.

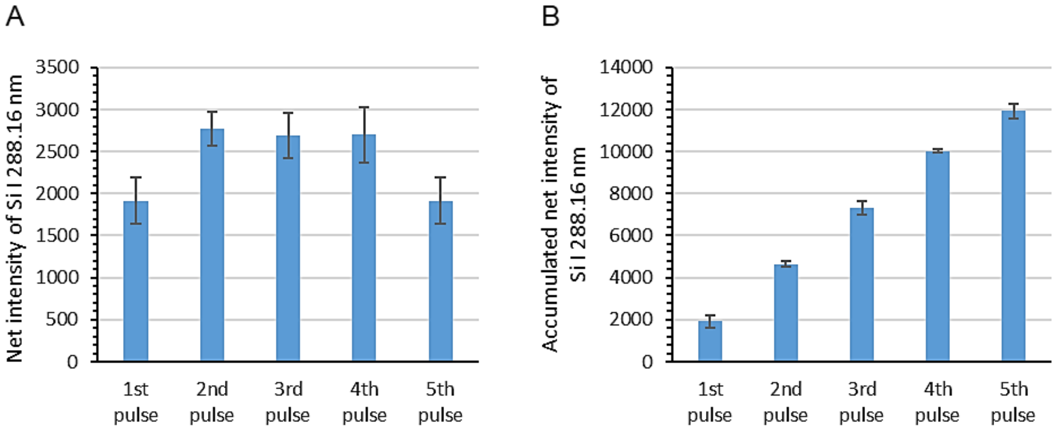

Figure 45. A) MP-LIBS silicon intensities generated by individual laser pulses within the burst and B) by the cumulative emission from all pulses. Using 50 ns laser pulses with 1 mJ pulse energy, 10 µs interpulse delay. Figure reproduced from own publication [P5].

As seen in **Fig. 45b**, when emission from multiple pulses is accumulated, the total LIBS signal increases monotonically with the pulse number without loss of repeatability, enabled by the low background emission characteristic of long duration fiber laser pulses [51,52]. This demonstrates that MP-LIBS with signal accumulation is an effective strategy for improving sensitivity in practical measurements.

7. PESTICIDE DETECTION USING LIBS AND MACHINE LEARNING

LIBS has become an important analytical technique in the agriculture and food sectors due to its capability for rapid, in situ, and on-line analysis. It has been applied to a wide range of agricultural products to assess elemental composition, which is a key indicator of food quality, nutritional value, authenticity, and safety [174]. Conventional elemental and food analysis techniques offer high sensitivity and reliability but require extensive sample preparation and are time-consuming; limiting their applicability for rapid screening and on-site analysis. In contrast, LIBS enables real-time, field-deployable measurements, making it well suited for fast screening applications; in particular, the detection and quantification of plant nutrients and heavy metals, pesticide residues, impurities and other pollutants, as well as the quality control of food derivatives, the identification of possible food adulteration and early plant disease diagnosis [175,176].

Variations in elemental composition, including the presence of trace elements and chemical contaminants, can significantly affect the quality, nutritional properties, and safety of agricultural products, with potential implications for human health. The integration of LIBS with chemometric methods further enhances data interpretation and classification performance, enabling reliable qualitative and quantitative analysis [177].

In this work I investigated the potential of LIBS for the detection/identification of organochlorine pesticide residues on tomato fruit surface in an effort to develop a fast screening methodology for e.g. the detection of the potential use of banned pesticides.

7.1. Background

Organochlorine pesticides (OCPs) remain a major analytical and toxicological concern due to their environmental persistence, high lipophilicity, and capacity for long-range environmental transport. Their long biological half-lives promote bioaccumulation in fatty tissues and biomagnification across food chains, leading to widespread exposure in humans and wildlife [178-181]. Many OCPs act as endocrine-disrupting chemicals causing reproductive and metabolic disorders. Neurotoxic, immunotoxic, and carcinogenic effects have also been reported [182-184]. These adverse impacts have resulted in strict regulations and bans on the use of several OCPs worldwide [185,186].

Reliable monitoring of OCP residues in food, environmental samples, and biological matrices is therefore essential but analytically challenging. Their determination typically requires extensive extraction and cleanup procedures to separate pesticides from lipids and other co-extracted organic matter [187]. Furthermore, the structural complexity of OCPs, including the presence of multiple congeners and stereoisomers with similar physicochemical properties, necessitates the use of advanced analytical instrumentation. HPLC or GC coupled with high-resolution or tandem mass spectrometry remains the standard approach, offering excellent sensitivity and selectivity but at the cost of lengthy analysis times, complex workflows, and laboratory-bound operation [188,189]. An additional challenge arises from the very low surface concentrations of OCPs on crops, often in the ng-pg cm^{-2} range, which makes their direct detection particularly difficult. Only a limited number of techniques, such as desorption/ionization mass spectrometry, direct analysis in real-time mass spectrometry, and surface-enhanced Raman spectroscopy, have demonstrated potential for surface-level detection [190-192]. However, strong sorption of hydrophobic pesticides to waxy plant cuticles, combined with surface heterogeneity, can limit desorption efficiency, reduce reproducibility, and compromise analytical reliability.

LIBS has recently attracted increasing attention for agricultural and food analysis, including pesticide analysis. Early works showed that pesticide treated and untreated samples could be discriminated at ppm-level concentrations using chemometric analysis [193]. Subsequent studies focused on monitoring characteristic spectral lines of pesticides (Cl, P, S) to detect and quantify residues on apples, leafy vegetables, and cereal crops [194-196]. The use of NE-LIBS for enhanced elemental mapping has been used to improve sensitivity and enabled quantitative analysis under controlled conditions [81].

Despite these advances, most reported approaches rely on the direct detection of a limited number of selected elements associated with specific pesticide formulations. This strategy may limit robustness and general applicability, particularly when dealing with structurally similar compounds, varying surface conditions, or complex background matrices. Moreover, relatively few studies have explored the systematic use of advanced machine learning techniques to extract and exploit the full spectral information content for pesticide identification. In this context, the present study was aimed at evaluating the potential of combining LIBS spectral data with machine learning (chemometric) algorithms for the rapid identification of five different organochlorine pesticides on tomato fruit surfaces, rather than relying solely on selected elemental lines.

7.2. Experimental

LIBS experiments were carried out on the J-200 LIBS instrument, in ambient air. LIBS parameters were optimized in order to obtain maximum atomic emission intensity of halogen spectral lines. Based on optimization experiments, a 40 µm laser focal spot diameter and 10 mJ pulse energy, as well as a 0.3 µs gate delay and 1 ms gate width were used.

Because the investigated pesticides are classified as moderately to highly hazardous by the European Food Safety Authority (EFSA) [197], all measurements were performed in a custom-made, closed ablation cell mounted in the instrument sample holder. The cell was designed to ensure safe operation while remaining compatible with the LIBS optical geometry, potential signal-enhancement, and routine laboratory use. It incorporates multiple cylindrical mini-wells, allowing several samples to be analyzed and enabling easy disassembly and cleaning between runs.

Design constraints were dictated by the instrument optics, since the J200 is not uniaxial with the laser beam, the wells could not be made too deep, otherwise the cavity walls would block plasma emission. However, excessively shallow wells would allow ablated material to contaminate the cell window and attenuate both the laser and plasma light. In addition, I employed to exploit spatial plasma confinement using shockwave reflection from rigid cavity walls to compress the plasma and enhance signal intensity, which requires a cavity depth of approximately 5 mm [55]. The final design therefore balanced optical accessibility, contamination control, safety, and the conditions necessary for effective plasma collection.

After optimization, the ablation cell was fabricated from aluminum alloy and designed as a three-part assembly consisting of a base, a removable insert containing the wells, and a top cover (**Fig. 46**). The insert holds eight cylindrical wells, each 8 mm in diameter and 5 mm deep, allowing multiple samples to be analyzed and enabling ease loading and cleaning. A 76.2×25.4 mm, 1 mm thick quartz microscope slide (Ted Pella Inc., USA) served as a top window, sealing all wells simultaneously. Individual wells were additionally sealed with o-rings (8 mm inner diameter, 1 mm thickness) positioned between the insert and the slide. The aluminum cover was secured to the base with six M3 countersunk screws, ensuring a tight, stable assembly. Between samples, the ablation cell assembly was cleaned with analytical trace quality water (MilliQ Elix 10/Synergy, Merck, USA) and analytical grade reagents, including Citranox solution (Alconox Inc., USA), isopropanol, and acetone (VWR Chemicals, USA).

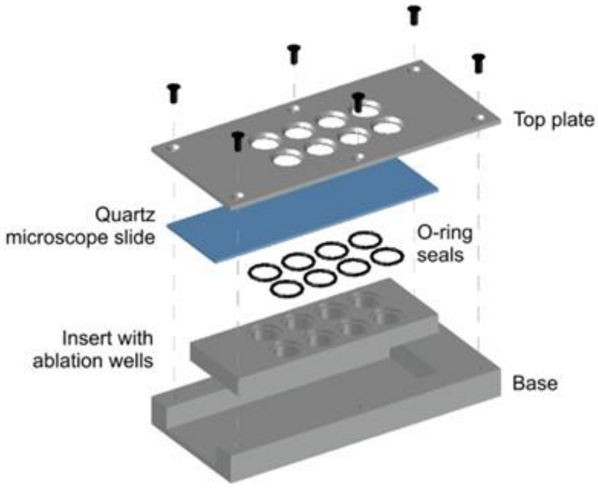

Figure 46. 3D representation of the custom closed ablation cell assembly designed for LIBS measurements. Figure reproduced from own publication [P6].

Pesticide analytical standards of acetamiprid ($C_{10}H_{11}ClN_4$), chlorpyrifos ($C_9H_{11}Cl_3NO_3PS$), λ-cyhalothrin ($C_{23}H_{19}ClF_3NO_3$), tebuconazole ($C_{16}H_{22}ClN_3O$), and tefluthrin ($C_{17}H_{14}ClF_7O_2$) were obtained from LabInstruments S.r.l. (Bari, Italy) with certified purities of 97.1–99.9%. Stock solutions (0.01, 0.1, and 1 m/v%) were prepared in absolute ethanol (VWR Chemicals, USA) and stored at 4 °C in amber glass vials.

Tomato fruits of *Solanum lycopersicum* L. (cv. “Money Maker”) were grown under controlled conditions at the Department of Plant Biology, without the application of pesticides that could interfere with the analysis. Seeds were germinated between moist filter papers in the dark at 24 °C for 4 days, after which seedlings were transferred to perlite and grown for 2 weeks. Plants were then cultivated hydroponically for 5 weeks. The nutrient solution (pH 5.8), prepared from analytical grade reagents, was renewed three times per week and contained: 2 mM $Ca(NO_3)_2$, 1 mM $MgSO_4$, 0.5 mM KH_2PO_4, 0.5 mM Na_2HPO_4, 0.5 mM KCl, 10^{-6} M $MnSO_4$, 5×10^{-7} M $ZnSO_4$, 10^{-7} M $CuSO_4$, 10^{-7} M $(NH_4)_6Mo_7O_{24}$, 10^{-7} M $AlCl_3$, 10^{-7} M $CoCl_2$,

10^{-5} M H^3BO^3, and 2 × 10^{-5} M Fe(III)-EDTA. Following hydroponic cultivation, plants were transferred to soil-filled pots and irrigated twice weekly with the same nutrient solution. Growth conditions were maintained at a 12/12 h light/dark cycle with LED illumination, temperatures of 24/22 °C (day/night), and relative humidity of 55-60%. Plants began producing fruits at approximately 20 weeks, and fully ripe fruits of uniform size and shape were selected for measurements.

Tomato fruits were washed with lab-water, air-dried, and only the outer skin (exocarp) was used for the experiments. Skins were peeled-off and cut into pieces sized to fit the ablation cell wells (ca. 0.5 cm^2). For experiments with fresh (“wet”) samples, peel pieces were spiked with 10 µL of pesticide solution and dried at room temperature under a clean hood. For dry samples, peels were first flat-pressed for 14 days in an object holder press (Kulzer GmbH, Germany) between filter paper sheets and polyethylene films to avoid cross-contamination. Before LIBS measurements, these sample were spiked with pesticide solutions and left to dry. In some experiments, dry pesticide residues on the fresh peels were collected and transferred to NPG substrates. Residues were swabbed from treated peels using an ethanol-moistened cotton swab and applied to a clean NPG disc. An additional 10 µL of ethanol was pipetted onto the swab and allowed to drip onto the substrate to ensure efficient transfer, after which the substrate was dried under a clean hood.

For experiments involving liquid sampling and transfer onto a substrate, Varapor-100 nanoporous glass (NPG) 99% SiO_2 discs (Advanced Glass & Ceramics Ltd., USA) were used as substrates, with a mean pore diameter of 10 nm, and 6.4 mm diameter size and 1 mm in thickness.

7.3. Optimization of measurements conditions

Prior to any LIBS measurements, it was necessary to identify which regions of the eight ablation wells allowed efficient plasma emission collection. Zinc sheets (8 mm diameter) were placed at the bottom of each well, and LIBS single-shots were performed on a 5 × 5 grid (1 mm spacing). The net intensity of the Zn I 636.2 nm line was used to generate “heat maps” of usable sampling areas (**Fig. 47**). The results indicated that all wells except No. 2 and 4 were suitable for single-shot measurements at their centers. However, to ensure consistent data reproducibility and accommodate a large number of spectra required, only wells No. 1, 3, 5, and 7 were used in subsequent experiments.

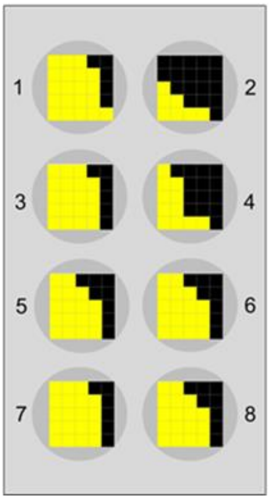

Figure 47. Heat map of the ablation well bottoms. Black areas correspond to regions where plasma emission cannot be effectively collected. Figure reproduced from own publication [P6].

The thermal and UV photolytic stability of many pesticides is limited, and their degradation pathways in water, soil, and edible plants have therefore been widely investigated [198-200]. The pesticides examined in this study have reported decomposition temperatures between 170 and 350 °C [201]. Because laser-induced plasma can impose significant thermal stress through radiation and heat conduction [11], care was taken to minimize heat-induced degradation during analysis. A spacing of 1 mm between successive LIBS measurement spots was adopted, representing the maximum practical distance while still allowing reliable data collection.

7.4. Characterization of pesticide LIBS spectra

LIBS measurements were first performed on the pure solid pesticides to characterize their spectral features and assess the feasibility of classification. A few milligrams of each compound were used, and 50 single-shot spectra were acquired from individual grains. This was made possible by the fact that each solid grain was larger than the 40 µm analytical spot size.

Representative spectra of acetamiprid, chlorpyrifos, λ-cyhalothrin, tebuconazole, and tefluthrin are shown in **Fig. 48**. The overall spectral patterns are similar, reflecting their comparable elemental composition (mostly C, H, O, N, and Cl). Subtle differences are evident in the relative intensities of selected lines and in the structure of the C_2 and CN molecular bands. Low-intensity P lines (231.54 and 253.39 nm) appear in chlorpyrifos, while F lines (685.60, 687.02, 690.25, and 690.98 nm) are observed in λ-cyhalothrin and tefluthrin. Chlorine is present in all spectra at 833.3 and 837.59 nm, whereas sulfur lines were not clearly detected in chlorpyrifos.

Detection of non-metallic elements by LIBS is generally more effective in the VUV region or via molecular emission enhancement strategies [202-204], so the weak lines observed here are expected. Additionally, relying on a single elemental line such as chlorine, as was earlier described in the background section [81,194], is unlikely to provide reliable discrimination, particularly in direct analysis of tomato surfaces, where naturally occurring chloride is abundant [205,206].

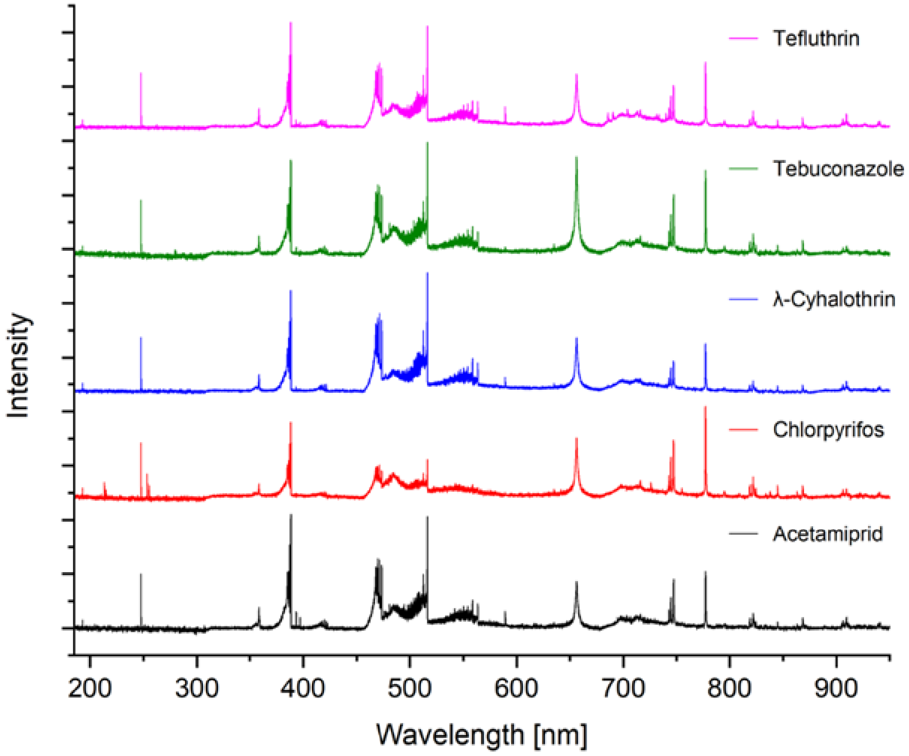

Figure 48. LIBS spectra of the pure solid pesticides measured in air.
Intensities are normalized to that of the C I 247.85 nm line. Figure reproduced from own publication [P6].

I also performed comparative classifications using LDA and RF on the LIBS spectra of the pure pesticides to evaluate whether the spectral information was sufficient for reliable discrimination, despite the visual similarity of the spectra in **Fig. 48**. Each model was trained 10 times using randomly selected subsets (70% of the data; 35 of 50 spectra per run). The average accuracy of RF training consistently achieved 100% accuracy across all runs, whereas for LDA it was 73.3 ± 1.5%. These results indicate that classification based on LIBS spectra is feasible and reasonably robust.

7.5. Classification based on direct measurements

One approach evaluated for pesticide detection involved LIBS measurements taken directly on tomato peels spiked with pesticide solutions, without sampling (the sampling-based strategy is discussed in the next section). Because moisture is known to adversely affect LIBS signal intensities [207], experiments were conducted on both dried peels and fresh peels (with its natural water content) in order to test the effect.

Spectra were collected from peels treated at three concentrations (1, 0.1, and 0.01 m/v%), acquiring 50 single-shot spectra per treatment. These concentrations reflect typical on-field application levels on crops [208-211]. Chemometric analysis was performed on the complete dataset (without preprocessing) using LDA, CT, and RF classifiers. For each pesticide, 35 spectra were randomly selected as the training set, and the procedure was repeated ten times with new random selections. Confusion matrices were generated for each run, and overall model accuracies were calculated as the mean of classification accuracies across pesticides and concentrations. Mean values and standard deviations were then determined to assess repeatability. The resulting discrimination performance is presented in **Fig. 49**.

For both fresh and dried peels, LDA achieved ca. 50% accuracy, which is reasonable given its restriction to linear decision boundaries in low-dimensional space. CT performed noticeably better, achieving mean accuracies near 80% across all concentrations. RF provided the highest performance, correctly classifying nearly all spectra (100%) regardless of peel condition or concentration. Standard deviations across repetitions were small, indicating good repeatability of the classification workflow. The very high RF performance likely reflects two factors. First, training was conducted at the level of individual laser shots spectra originating from the same treated peel, meaning many spectra were highly similar, facilitating pattern recognition [212]. Second, in high-dimensional LIBS datasets (thousands of variables with relatively few samples), RF can achieve very high training accuracy and may be prone to overfitting when validation is not performed exhaustively [213].

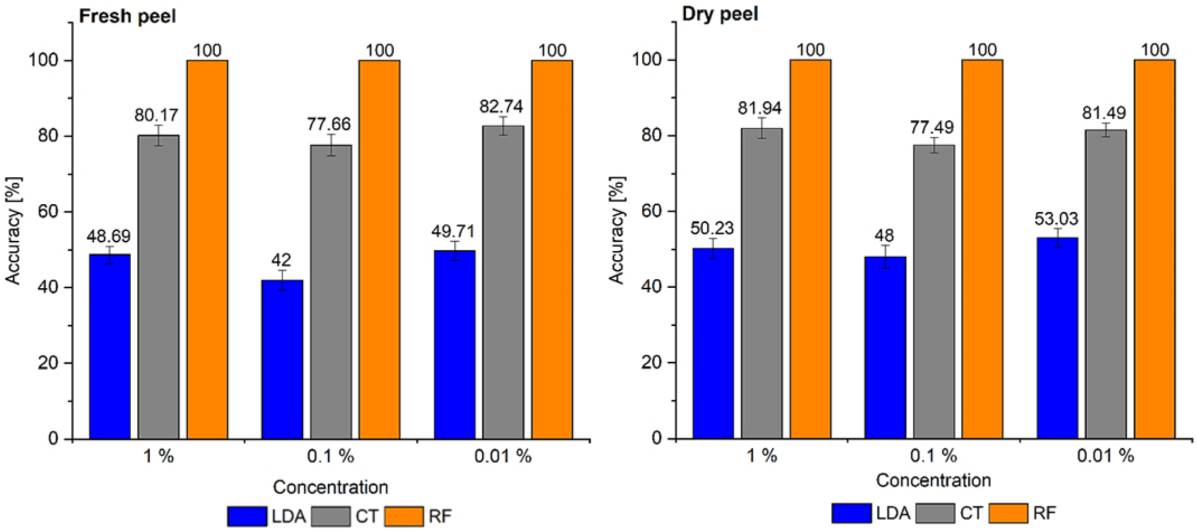

Figure 49. Comparison of training performance across classifiers for the fresh peel (left panel) and dry peel (right panel). Bars show average accuracy over 10 runs; error bars indicate repeatability. Figure reproduced from own publication [P6].

According to the RF variable-importance analysis, the predictors that contributed most to classification were emission lines of Na, K, Ca, Mg, and Al. These elements most likely originated from impurities, the tomato peel matrix, or occasional penetration into the ablation-well surface. Thus, higher accuracies obtained earlier do not fully reflect intrinsic classification performance, as they may depend partly on pesticide purity or matrix differences rather than molecular characteristics.

To minimize such matrix effects, spectra were pre-processed in the next evaluation step. Polynomial background correction was applied, and strong emission lines associated with Na, K, Ca, Mg, and Al (from the NIST database), as well as lines present in blank tomato peels, were masked. Feature selection was then conducted using RF variable importance to identify informative wavelengths [94]. Five-fold cross-validation was performed on the training set while varying the number of retained features (10-60), achieving training accuracies of 59-82% and cross-validation accuracies of 51-54%. As a compromise between model complexity and performance, the top 50 wavelengths were selected. Among the RF-selected predictors, the most frequent features corresponded to C, P, O, H, and Cl emission lines, as well as C_2 and CN molecular bands (**Table 4**), with small wavelength shifts between fresh and dry peels due to matrix effects. This confirms that masking effectively removed contributions from common contaminants while retaining chemically meaningful predictors. For each repetition, RF importance was recalculated on the respective training subset [213]; the 50 selected wavelengths were extracted, and LDA and RF models were fitted and evaluated on independent test spectra. For CT, separate feature selection was omitted because trees inherently perform variable selection, and preliminary testing showed no benefit from further restriction. All calculations followed the procedure described previously. The resulting classification performance is presented in **Fig. 50**.

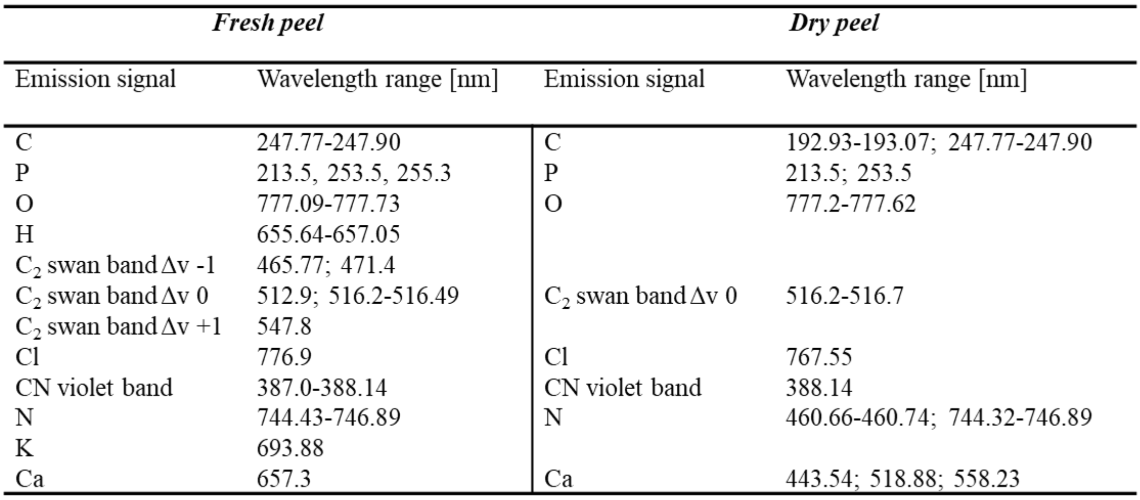

Fresh peel		***Dry peel***	
Emission signal	Wavelength range [nm]	Emission signal	Wavelength range [nm]
C	247.77-247.90	C	192.93-193.07; 247.77-247.90
P	213.5, 253.5, 255.3	P	213.5; 253.5
O	777.09-777.73	O	777.2-777.62
H	655.64-657.05		
C_2 swan band Δv -1	465.77; 471.4		
C_2 swan band Δv 0	512.9; 516.2-516.49	C_2 swan band Δv 0	516.2-516.7
C_2 swan band Δv +1	547.8		
Cl	776.9	Cl	767.55
CN violet band	387.0-388.14	CN violet band	388.14
N	744.43-746.89	N	460.66-460.74; 744.32-746.89
K	693.88		
Ca	657.3	Ca	443.54; 518.88; 558.23

Table 4. Discriminative emission features among the top-50 RF-selected wavelengths for the fresh and dry tomato peels used for the chemometric models. Figure reproduced from own publication [P6].

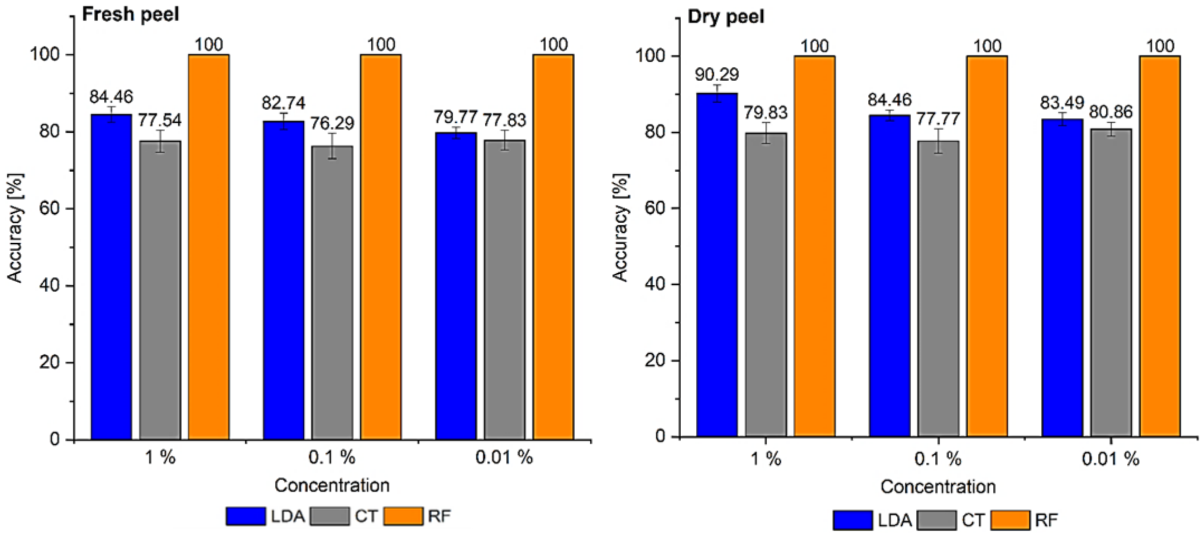

Fig. 50. Overall training accuracies (mean of 10 runs) and repeatability (error bars) of the classifiers for the fresh peel (left panel) and dry peel (right panel) applied to the top 50 RF-selected features. Figure reproduced from own publication [P6].

For the fresh peels, LDA and CT achieved accuracies of ~75-80% across all concentrations, while RF classified all spectra correctly (100%). For the dry peels, LDA and CT performed slightly better (upper-70% to low-80% range), and RF again achieved perfect discrimination. The limited concentration dependence and small error bars indicate that the selected wavelengths retain pesticide-specific information that remains stable despite drying and dilution of the residues.

Although RF-based feature selection reduced the dataset to the 50 most informative wavelengths, RF still reached 100% training accuracy. This agrees with previous observations that RF may overfit in high-dimensional, small-sample contexts, even after variable selection, and that reliable performance assessment requires strict nested validation [214,215]. Therefore, LDA and CT likely provide more realistic estimates of achievable discrimination under the present conditions. Generated confusion matrices for LDA and CT (**Tables 5-8**) show diagonal values predominantly in the mid to high 80% range, with little dependence on concentration. Across models, cyhalothrin shows the lowest correct-classification rate, whereas tefluthrin and chlorpyrifos are generally the most consistently identified.

Table 5. Confusion matrices for **LDA** classification on the training set on **fresh tomato peel**, containing data for the average accuracy (%) and repeatability from 10 repeated calculations for all samples with randomly selected spectra. Numbers in the diagonal are the percentages of correctly classified spectra. Table reproduced from own publication [P6].

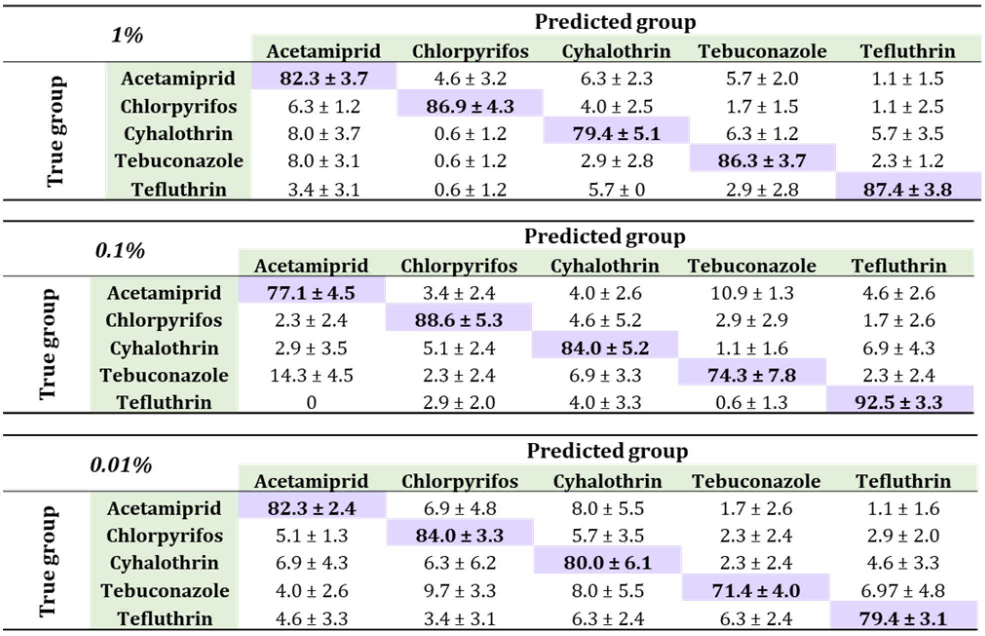

	1%	**Predicted group**				
		Acetamiprid	**Chlorpyrifos**	**Cyhalothrin**	**Tebuconazole**	**Tefluthrin**
True group	**Acetamiprid**	**82.3 ± 3.7**	4.6 ± 3.2	6.3 ± 2.3	5.7 ± 2.0	1.1 ± 1.5
	Chlorpyrifos	6.3 ± 1.2	**86.9 ± 4.3**	4.0 ± 2.5	1.7 ± 1.5	1.1 ± 2.5
	Cyhalothrin	8.0 ± 3.7	0.6 ± 1.2	**79.4 ± 5.1**	6.3 ± 1.2	5.7 ± 3.5
	Tebuconazole	8.0 ± 3.1	0.6 ± 1.2	2.9 ± 2.8	**86.3 ± 3.7**	2.3 ± 1.2
	Tefluthrin	3.4 ± 3.1	0.6 ± 1.2	5.7 ± 0	2.9 ± 2.8	**87.4 ± 3.8**

	0.1%	**Predicted group**				
		Acetamiprid	**Chlorpyrifos**	**Cyhalothrin**	**Tebuconazole**	**Tefluthrin**
True group	**Acetamiprid**	**77.1 ± 4.5**	3.4 ± 2.4	4.0 ± 2.6	10.9 ± 1.3	4.6 ± 2.6
	Chlorpyrifos	2.3 ± 2.4	**88.6 ± 5.3**	4.6 ± 5.2	2.9 ± 2.9	1.7 ± 2.6
	Cyhalothrin	2.9 ± 3.5	5.1 ± 2.4	**84.0 ± 5.2**	1.1 ± 1.6	6.9 ± 4.3
	Tebuconazole	14.3 ± 4.5	2.3 ± 2.4	6.9 ± 3.3	**74.3 ± 7.8**	2.3 ± 2.4
	Tefluthrin	0	2.9 ± 2.0	4.0 ± 3.3	0.6 ± 1.3	**92.5 ± 3.3**

	0.01%	**Predicted group**				
		Acetamiprid	**Chlorpyrifos**	**Cyhalothrin**	**Tebuconazole**	**Tefluthrin**
True group	**Acetamiprid**	**82.3 ± 2.4**	6.9 ± 4.8	8.0 ± 5.5	1.7 ± 2.6	1.1 ± 1.6
	Chlorpyrifos	5.1 ± 1.3	**84.0 ± 3.3**	5.7 ± 3.5	2.3 ± 2.4	2.9 ± 2.0
	Cyhalothrin	6.9 ± 4.3	6.3 ± 6.2	**80.0 ± 6.1**	2.3 ± 2.4	4.6 ± 3.3
	Tebuconazole	4.0 ± 2.6	9.7 ± 3.3	8.0 ± 5.5	**71.4 ± 4.0**	6.97 ± 4.8
	Tefluthrin	4.6 ± 3.3	3.4 ± 3.1	6.3 ± 2.4	6.3 ± 2.4	**79.4 ± 3.1**

Table 6. Confusion matrices for **CT** classification on the training set on **fresh tomato peel**, containing data for the average accuracy (%) and repeatability from 10 repeated calculations for all samples with randomly selected spectra. Numbers in the diagonal are the percentages of correctly classified spectra. Table reproduced from own publication [P6].

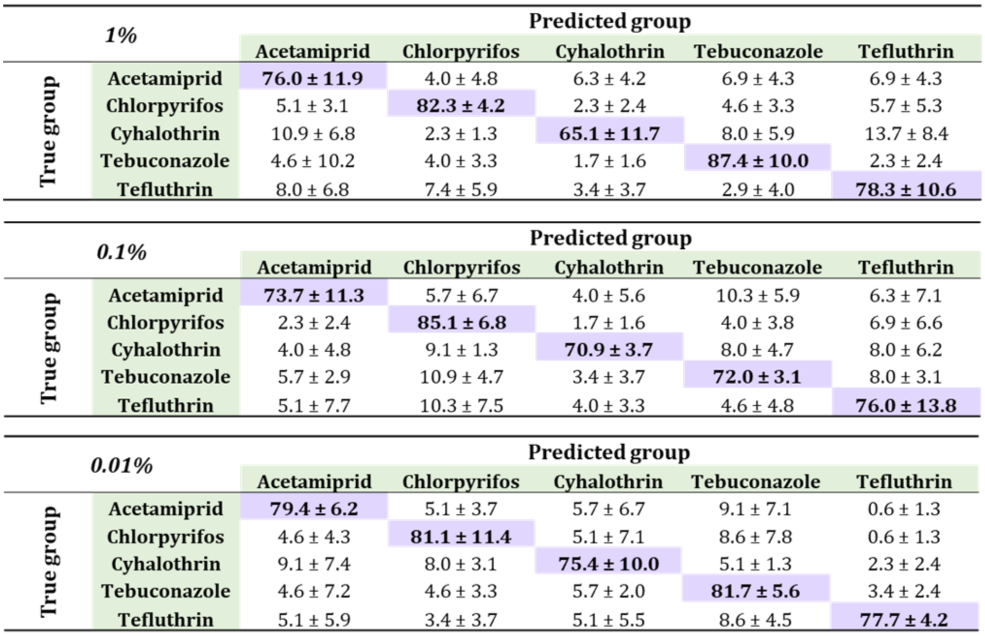

	1%	**Predicted group**				
		Acetamiprid	**Chlorpyrifos**	**Cyhalothrin**	**Tebuconazole**	**Tefluthrin**
True group	**Acetamiprid**	**76.0 ± 11.9**	4.0 ± 4.8	6.3 ± 4.2	6.9 ± 4.3	6.9 ± 4.3
	Chlorpyrifos	5.1 ± 3.1	**82.3 ± 4.2**	2.3 ± 2.4	4.6 ± 3.3	5.7 ± 5.3
	Cyhalothrin	10.9 ± 6.8	2.3 ± 1.3	**65.1 ± 11.7**	8.0 ± 5.9	13.7 ± 8.4
	Tebuconazole	4.6 ± 10.2	4.0 ± 3.3	1.7 ± 1.6	**87.4 ± 10.0**	2.3 ± 2.4
	Tefluthrin	8.0 ± 6.8	7.4 ± 5.9	3.4 ± 3.7	2.9 ± 4.0	**78.3 ± 10.6**

	0.1%	**Predicted group**				
		Acetamiprid	**Chlorpyrifos**	**Cyhalothrin**	**Tebuconazole**	**Tefluthrin**
True group	**Acetamiprid**	**73.7 ± 11.3**	5.7 ± 6.7	4.0 ± 5.6	10.3 ± 5.9	6.3 ± 7.1
	Chlorpyrifos	2.3 ± 2.4	**85.1 ± 6.8**	1.7 ± 1.6	4.0 ± 3.8	6.9 ± 6.6
	Cyhalothrin	4.0 ± 4.8	9.1 ± 1.3	**70.9 ± 3.7**	8.0 ± 4.7	8.0 ± 6.2
	Tebuconazole	5.7 ± 2.9	10.9 ± 4.7	3.4 ± 3.7	**72.0 ± 3.1**	8.0 ± 3.1
	Tefluthrin	5.1 ± 7.7	10.3 ± 7.5	4.0 ± 3.3	4.6 ± 4.8	**76.0 ± 13.8**

	0.01%	**Predicted group**				
		Acetamiprid	**Chlorpyrifos**	**Cyhalothrin**	**Tebuconazole**	**Tefluthrin**
True group	**Acetamiprid**	**79.4 ± 6.2**	5.1 ± 3.7	5.7 ± 6.7	9.1 ± 7.1	0.6 ± 1.3
	Chlorpyrifos	4.6 ± 4.3	**81.1 ± 11.4**	5.1 ± 7.1	8.6 ± 7.8	0.6 ± 1.3
	Cyhalothrin	9.1 ± 7.4	8.0 ± 3.1	**75.4 ± 10.0**	5.1 ± 1.3	2.3 ± 2.4
	Tebuconazole	4.6 ± 7.2	4.6 ± 3.3	5.7 ± 2.0	**81.7 ± 5.6**	3.4 ± 2.4
	Tefluthrin	5.1 ± 5.9	3.4 ± 3.7	5.1 ± 5.5	8.6 ± 4.5	**77.7 ± 4.2**

Table 7. Confusion matrices for **LDA** classification on the training set on **dry tomato peel**, containing data for the average accuracy (%) and repeatability from 10 repeated calculations for all samples with randomly selected spectra. Numbers in the diagonal are the percentages of correctly classified spectra. Table reproduced from own publication [P6].

1%		**Predicted group**				
		Acetamiprid	**Chlorpyrifos**	**Cyhalothrin**	**Tebuconazole**	**Tefluthrin**
True group	**Acetamiprid**	**85.1 ± 3.7**	0.6 ± 1.3	0.6 ± 1.3	11.4 ± 4.5	2.3 ± 2.4
	Chlorpyrifos	5.1 ± 2.4	**90.3 ± 2.6**	0	3.4 ± 2.4	1.1 ± 1.6
	Cyhalothrin	0.6 ± 1.3	0	**89.7 ± 2.6**	5.7 ± 3.5	4.0 ± 1.6
	Tebuconazole	7.4 ± 4.3	1.1 ± 2.6	2.9 ± 3.5	**86.3 ± 8.9**	2.3 ± 3.7
	Tefluthrin	0	1.1 ± 1.6	2.9 ± 2.0	0	**96.0 ± 2.6**

0.1%		**Predicted group**				
		Acetamiprid	**Chlorpyrifos**	**Cyhalothrin**	**Tebuconazole**	**Tefluthrin**
True group	**Acetamiprid**	**83.4 ± 3.1**	7.4 ± 2.6	1.7 ± 1.6	5.1 ± 2.4	2.3 ± 2.4
	Chlorpyrifos	0.6 ± 1.3	**85.1 ± 4.7**	0.6 ± 1.3	8.0 ± 2.4	5.7 ± 2.9
	Cyhalothrin	2.3 ± 1.3	7.4 ± 3.3	**84.0 ± 1.6**	5.7 ± 2.0	0.6 ± 1.3
	Tebuconazole	2.3 ± 1.3	12.0 ± 1.3	5.1 ± 3.1	**78.9 ± 5.6**	1.7 ± 2.6
	Tefluthrin	0	6.3 ± 4.7	1.1 ± 1.6	0.6 ± 1.3	**92.0 ± 4.2**

0.01%		**Predicted group**				
		Acetamiprid	**Chlorpyrifos**	**Cyhalothrin**	**Tebuconazole**	**Tefluthrin**
True group	**Acetamiprid**	**97.1 ± 2.0**	1.1 ± 1.6	1.1 ± 1.6	0	0.6 ± 1.3
	Chlorpyrifos	0	**74.9 ± 6.2**	9.1 ± 3.1	13.1 ± 4.3	2.9 ± 2.0
	Cyhalothrin	4.6 ± 1.6	8.6 ± 3.5	**77.1 ± 4.5**	5.7 ± 2.9	4.0 ± 2.6
	Tebuconazole	0	17.1 ± 3.5	9.1 ± 3.1	**72.6 ± 6.6**	1.1 ± 1.6
	Tefluthrin	0	2.9 ± 2.0	4.0 ± 1.6	1.7 ± 1.6	**91.4 ± 2.0**

Table 8. Confusion matrices for **CT** classification on the training set on **dry tomato peel**, containing data for the average accuracy (%) and repeatability from 10 repeated calculations for all samples with randomly selected spectra. Numbers in the diagonal are the percentages of correctly classified spectra. Table reproduced from own publication [P6].

1%		**Predicted group**				
		Acetamiprid	**Chlorpyrifos**	**Cyhalothrin**	**Tebuconazole**	**Tefluthrin**
True group	**Acetamiprid**	**78.9 ± 3.8**	0.6 ± 1.3	12.0 ± 4.7	7.4 ± 4.3	1.1 ± 1.6
	Chlorpyrifos	10.3 ± 3.8	**73.1 ± 16.0**	6.3 ± 7.7	8.6 ± 8.3	1.7 ± 3.8
	Cyhalothrin	9.1 ± 5.5	0.6 ± 1.3	**80.0 ± 7.3**	6.9 ± 4.3	3.4 ± 2.4
	Tebuconazole	9.1 ± 5.5	6.3 ± 5.9	5.1 ± 5.5	**74.9 ± 5.1**	4.6 ± 3.3
	Tefluthrin	5.1 ± 5.9	2.3 ± 2.4	4.0 ± 2.6	0	**88.6 ± 3.5**

0.1%		**Predicted group**				
		Acetamiprid	**Chlorpyrifos**	**Cyhalothrin**	**Tebuconazole**	**Tefluthrin**
True group	**Acetamiprid**	**81.1 ± 9.6**	8.0 ± 8.9	3.4 ± 3.7	4.6 ± 4.8	2.9 ± 2.0
	Chlorpyrifos	7.4 ± 11.4	**76.0± 13.6**	5.7 ± 5.3	5.1 ± 6.2	5.7 ± 4.5
	Cyhalothrin	3.4 ± 3.1	10.9 ± 10.2	**74.9 ± 13.6**	6.9 ± 6.6	4.0 ± 3.3
	Tebuconazole	9.7 ± 7.7	8.0 ± 5.5	4.0 ± 3.3	**76.6 ± 10.2**	1.7 ± 2.6
	Tefluthrin	2.9 ± 2.0	9.1 ± 7.4	0.6 ± 1.3	5.7 ± 6.1	**81.7 ± 5.2**

0.01%		**Predicted group**				
		Acetamiprid	**Chlorpyrifos**	**Cyhalothrin**	**Tebuconazole**	**Tefluthrin**
True group	**Acetamiprid**	**88.0 ± 9.8**	0	1.7 ± 2.6	5.7 ± 6.7	4.6 ± 4.3
	Chlorpyrifos	1.7 ± 2.6	**73.1 ± 3.3**	6.3 ± 4.2	9.7 ± 5.9	9.1 ± 5.5
	Cyhalothrin	6.9 ± 2.6	5.7 ± 2.9	**75.4 ± 7.2**	5.7 ± 2.0	6.3 ± 8.7
	Tebuconazole	8.0 ± 4.7	6.9 ± 4.3	5.1 ± 3.7	**77.1 ± 8.1**	2.9 ± 2.9
	Tefluthrin	1.1 ± 1.6	4.0 ± 2.6	4.0 ± 3.3	4.6 ± 4.8	**86.3 ± 4.7**

7.6. Classification by measurements based on sampling

A more convenient approach for performing the pesticide LIBS analysis would be avoiding the need to pick and peel tomato samples. Therefore, I also investigated a sampling-based strategy in which pesticide residues were transferred from the fruit surface onto a substrate before LIBS analysis. Nanoporous glass (NPG) disks were selected because they effectively absorb and dry microliter-scale droplets, producing laterally uniform deposits. The penetration depth of the liquid (hundreds of micrometers) greatly exceeds the LIBS ablation depth (a few micrometers), enabling repeated single-shot measurements with similar sensitivity. NPG therefore provides a practical way for analyzing solution residues such as pesticides [216].

Pesticide residues from fresh peels treated with 1 m/v% pesticide solutions were collected by the cotton-swab transfer method and deposited onto NPG disks. 28 single-shot spectra were then recorded per sample at a grid with 1 mm spacing between spots. Spectra were pre-processed using polynomial background correction, and emission lines present in blank NPG spectra were masked. LDA, CT, and RF models were first trained on LIBS spectra from pesticide solutions deposited directly on NPG (training set). The transferred residue spectra were then classified as an independent prediction set. The results are shown in **Fig. 51**.

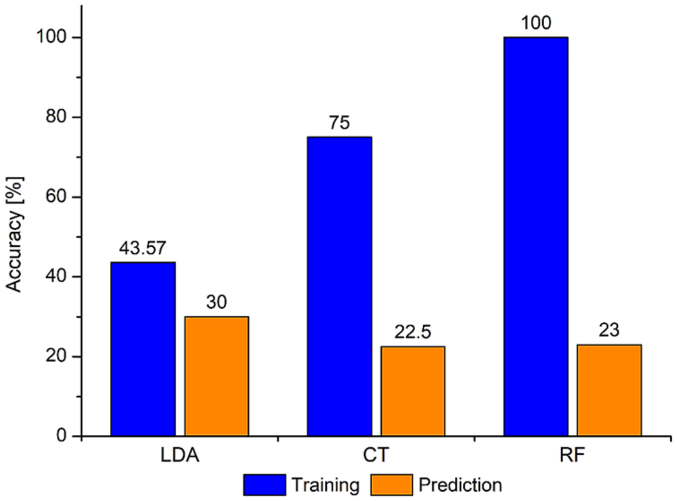

Fig. 51. Classification accuracies of models trained on solution spectra and tested on residues transferred from tomato peels to NPG. Models were trained using 1 m/v% pesticide solutions. Figure reproduced from own publication [P6].

Classifiers trained on NPG substrates performed moderately well; CT outperformed LDA, while RF again fitted the training set completely. However, accuracies decreased sharply when applied to the prediction set. The most likely explanation is loss of analyte during sampling, because the cotton swab may retain a substantial fraction of the residue. Additional factors may include transfer of cotton fibers, which could attenuate the signal, and the possible co-transfer of waxy peel components that interfere with the spectra. Overall, the sampling-based approach did not provide the accuracy or reliability required for robust classification.

8. SUMMARY

During my doctoral research, I focused on advanced laser-induced breakdown spectroscopy (LIBS) by improving its sensitivity, spatial resolution, mapping capability, and analytical reliability. My work encompassed methodological development and instrumental innovation for both fundamental and application studies.

A central line of research addressed how plasmonic nanoparticles can be used to boost LIBS signal intensity through localized surface plasmon resonance. I demonstrated that if a proper nanoparticle deposition technique is employed then NE-LIBS mapping is a viable and analytically advantageous approach. I found that out of the three tested deposition techniques the sputter-coating of the solid sample surface with a thin gold layer followed by a thermal treatment that converts the layer into nanoparticles, is a practical and well-controllable NE-LIBS sample preparation approach. This approach offered three advantages: good control of nanoparticle size and density, good reproducibility, and compatibility with analytical mapping. I systematically optimized deposition conditions and studied the influence of laser fluence, spot size, wavelength, and detector gating on the achievable signal enhancement. The results showed that enhancement factors of 25-30 can be achieved, and that the most critical parameters are laser fluence and gate delay. I also demonstrated that a spatial resolution of 100-200 µm can be achieved for elemental mapping. Finally, I applied the optimized NE-LIBS method for hyperspectral mapping. Its usefulness was successfully demonstrated in two qualitative analytical applications involving sample types of practical importance (granite rocks, paints). The results confirm that NE-LIBS can be a practical and powerful strategy to increase analytical sensitivity and improve spatial discrimination.

A second focus was developing LIBS as a quantitative mapping tool for nanocomposite thin films. Results show that LIBS elemental mapping provides reliable and practical analysis for assessing the lateral distribution of nanoparticles in polymer nanocomposite thin films, with 100 µm spatial resolution. Through optimization of laser parameters and a detailed study of ablation behavior I demonstrated that, when using a 266 nm laser wavelength and laser pulse energies of approximately 10 mJ, the method is suitable for polystyrene films up to ~450 nm thick and for surface gold concentration between 3 and 700 $ng \cdot mm^{-2}$. Patterned films containing nanoparticle gradients were mapped successfully, and the technique also enabled extraction of particle number distribution data when particle size was known. Since LIBS mapping is rapid, applicable to large areas, and compatible with a wide range of nanoparticle compositions, the approach represents a broadly usable tool for nanocomposite film characterization.

Another contribution involved exploring new laser sources for LIBS. I experimentally demonstrated that a master oscillator power amplifier (MOPA) fiber laser, capable of tunable pulse shapes and very high repetition rates are highly suitable for LIBS. By investigating time- and wavelength-resolved plasma emission, and signal-to-noise behavior, I showed that pulse shapes concentrating most energy at the pulse head provide the best analytical performance. Multi-pulse LIBS produced particularly strong enhancements, even when using interpulse delays up to 100 µs, the second pulse always generated significantly stronger emission than a single-pulse. Demonstrations on steel samples confirmed good analytical performance for Cu, Ni, and Cr detection. These findings reveal that pulsed fiber lasers as promising alternatives to conventional solid-state LIBS lasers.

Finally, I addressed the challenge of identifying organochlorine pesticides on the surface of agricultural products. Using LIBS combined with machine learning data evaluation (LDA, CT, RF) for the detection of pesticide residues on the surface of tomato fruits in an effort to develop a fast screening methodology. I showed that several hazardous pesticides can be detected from the surface of tomato fruits at concentrations as low as 100 ppm. Both direct surface analysis and indirect sampling approaches were compared, and a closed ablation cell was developed to ensure safe testing conditions. It was found that the application of spectral masking and advanced feature selection approaches are necessary to make the classification reliable of training the machine learners for common contaminants in the pesticides. Classification based on direct LIBS analysis, directly on tomato peels, proved to be significantly more reliable than the indirect analysis (transferring residues from the tomato surface). Across all concentration levels and for all machine learning models tested, the classification performance remained consistently high, with accuracies ranging from 77% to 100%. Among the algorithms, RF performed the best; however, the instances of 100% accuracy were likely indicative of overfitting. The accuracies achieved using LDA and CT, were within the 77-90% range, which appear to be more representative of realistic model performance. The results indicate that qualitative discrimination analysis using LIBS data is a promising candidate for the fast and reliable detection of hazardous pesticide residues on crops.

Together, these results show how LIBS performance can be systematically enhanced through nanoparticle-assisted plasmonic amplification, advanced laser technology, optimized mapping strategies, and modern data analysis tools. The methods developed here broaden the applicability of LIBS to areas ranging from nanomaterials research and geochemistry to industrial coatings and food safety monitoring.

9. REFERENCES

[1] Brech, F. J. a. S. Optical microemission stimulated by a ruby maser. *AppliedSpectroscopy* **1962**, *2* (16), 59.

[2] Runge, E. F.; Minck, R. W.; Bryan. Spectrochemical analysis using a pulsed laser source. *Spectrochimica Acta* **1964**, *20* (4), 733–736.

[3] Winefordner, J. D.; Gornushkin, I. B.; Correll, T.; Gibb, E.; Smith, B. W.; Omenetto, N. Comparing several atomic spectrometric methods to the super stars: special emphasis on laser induced breakdown spectrometry, LIBS, a future super star. *Journal of Analytical Atomic Spectrometry* **2004**, *19* (9), 1061.

[4] Galbács, G. A critical review of recent progress in analytical laser-induced breakdown spectroscopy. *Analytical and Bioanalytical Chemistry* **2015**, *407* (25), 7537–7562.

[5] Cremers, D. A.; Radziemski, L. J. *Handbook of Laser-Induced Breakdown Spectroscopy*; John Wiley & Sons, **2013**.

[6] Singh, J. P.; Thakur, S. N. *Laser-Induced Breakdown Spectroscopy*; Elsevier Science, 2020.

[7] Miziolek, A. W.; Palleschi, V.; Schechter, I. *Laser induced breakdown spectroscopy*; Cambridge University Press, **2006**.

[8] Gornushkin, I. B.; Smith, B. W.; Nasajpour, H.; Winefordner, J. D. Identification of solid materials by correlation analysis using a microscopic laser-induced plasma spectrometer. *Analytical Chemistry* **1999**, *71* (22), 5157–5164.

[9] Tognoni, E.; Cristoforetti, G. [INVITED] Signal and noise in laser induced breakdown spectroscopy: An introductory review. *Optics & Laser Technology* **2015**, *79*, 164–172.

[10] De Giacomo, A.; Alrifai, R.; Gardette, V.; Salajková, Z.; Dell’Aglio, M. Nanoparticle enhanced laser ablation and consequent effects on laser induced plasma optical emission. *Spectrochimica Acta Part B Atomic Spectroscopy* **2020**, *166*, 105794.

[11] Galbács, G.; Jedlinszki, N.; Herrera, K.; Omenetto, N.; Smith, B. W.; Winefordner, J. A study of ablation, spatial, and temporal characteristics of laser-induced plasmas generated by multiple collinear pulses. *Applied Spectroscopy* **2010**, *64* (2), 161–172.

[12] Li, Y.; Tian, D.; Ding, Y.; Yang, G.; Liu, K.; Wang, C.; Han, X. A review of laser-induced breakdown spectroscopy signal enhancement. *Applied Spectroscopy Reviews* **2017**, *53* (1), 1–35.

[13] Hoehse, M.; Mory, D.; Florek, S.; Weritz, F.; Gornushkin, I.; Panne, U. A combined laser-induced breakdown and Raman spectroscopy Echelle system for elemental and molecular microanalysis. *Spectrochimica Acta Part B Atomic Spectroscopy* **2009**, *64* (11–12), 1219–1227.

[14] Gajarska, Z.; Brunnbauer, L.; Lohninger, H.; Limbeck, A. Identification of 20 polymer types by means of laser-induced breakdown spectroscopy (LIBS) and chemometrics. *Analytical and Bioanalytical Chemistry* **2021**, *413* (26), 6581–6594.

[15] Galbács, G. *Laser-Induced Breakdown Spectroscopy in Biological, Forensic and Materials sciences;* Springer Cham, **2025**.

[16] Pasquini, C.; Cortez, J.; Silva, L. M. C.; Gonzaga, F. B. Laser induced breakdown spectroscopy. *Journal of the Brazilian Chemical Society* **2007**, *18* (3), 463–512.

[17] Singh, V. K.; Tripathi, D. K.; Deguchi, Y.; Wang, Z. *Laser Induced Breakdown Spectroscopy (LIBS): Concepts, Instrumentation, Data Analysis and Applications, 2 Volume Set*; John Wiley & Sons, 2023.

[18] Musazzi, S.; Perini, U. *Laser-Induced Breakdown Spectroscopy: Theory and Applications*; Springer, **2014**.

[19] Hahn, D. W.; Omenetto, N. Laser-induced breakdown spectroscopy (LIBS), Part I: Review of basic diagnostics and plasma—particle interactions: still-challenging issues within the analytical plasma community. *Applied Spectroscopy* **2010**, *64* (12), 335A-336A.

[20] Borduchi, L. C. L.; Milori, D. M. B. P.; Villas-Boas, P. R. Study of the effects of detection times in laser-induced breakdown spectroscopy and missed variation of plasma parameters with gate width. *Spectrochimica Acta Part B Atomic Spectroscopy* **2022**, *191*, 106409.

[21] Svelto, O. *Principles of lasers*; Springer, **2009**.

[22] Noll, R. *Laser-Induced Breakdown Spectroscopy: Fundamentals and Applications*; Springer, **2012**.

[23] Paschotta, R. Birefringent Tuners. *RP Photonics Encyclopedia*; 2007.https://doi.org/10.61835/q9c (accessed 2025-10-18).

[24] Demırbas, U. Off-surface optic axis birefringent filters for smooth tuning of broadband lasers. *Applied Optics* **2017**, *56* (28), 7815.

[25] Koechner, W. *Solid-State Laser Engineering*; 2006.

[26] Diehl, R. *High-Power Diode Lasers: Fundamentals, Technology, Applications*; Springer, 2010.

[27] Alvarez-Chavez, J. A.; Offerhaus, H. L.; Nilsson, J.; Turner, P. W.; Clarkson, W. A.; Richardson, D. J. High-energy, high-power ytterbium-doped Q-switched fiber laser. *Optics Letters* **2000**, *25* (1), 37.

[28] Himeno, K. *Basics and features of high-power fiber laser*; 44; Fujikura Technical Review, 2015. https://www.fujikura.co.jp/en/research/technical-report/no044.html (accessed 2025-10-18).

[29] Gravel, J.-F. Y.; Doucet, F. R.; Bouchard, P.; Sabsabi, M. Evaluation of a compact high power pulsed fiber laser source for laser-induced breakdown spectroscopy. *Journal of Analytical Atomic Spectrometry* **2011**, *26* (7), 1354.

[30] Richardson, D. J.; Nilsson, J.; Clarkson, W. A. High power fiber lasers: current status and future perspectives [Invited]. *Journal of the Optical Society of America B* **2010**, *27* (11), B63.

[31] Terada, Y.; Nakai, M.; Oba, Y. *High-power pulsed fiber lasers and their evolution*; 44; Fujikura Technical Review, 2015. https://www.fujikura.co.jp/en/research/technical-report/no044.html (accessed 2025-10-18).

[32] Capela, D.; Manso, M.; Lopes, T.; Cavaco, R.; Teixeira, J.; Jorge, P. a. S.; Silva, N.; Guimarães, D. Fiber laser LIBS as a sensing tool for chemical mapping of heritage tiles. *26th International Conference on Optical Fiber Sensors* **2025**, 492.

[33] Shabanov, S. V.; Gornushkin, I. B.; Winefordner, J. B. Radiation from asymmetric laser-induced plasmas collected by a lens or optical fiber. *Applied Optics* **2008**, *47* (11), 1745.

[34] Redoglio, D.; Perini, U.; Musazzi, S. *LIBS collection optics: Comparative analysis of different mirror-based configurations*; 2014 Fotonica AEIT Italian Conference on Photonics Technologies: Italy, 2014; pp 1–4.

[35] Tamura, K.; Ohba, H.; Saeki, M.; Taguchi, T.; Lim, H. H.; Taira, T.; Wakaida, I. Development of a laser-induced breakdown spectroscopy system using a ceramic

micro-laser for fiber-optic remote analysis.
Journal of Nuclear Science and Technology **2020**, *57* (10), 1189–1198.

[36] Saeki, M.; Iwanade, A.; Ito, C.; Wakaida, I.; Thornton, B.; Sakka, T.; Ohba, H. Development of a fiber-coupled laser-induced breakdown spectroscopy instrument for analysis of underwater debris in a nuclear reactor core.
Journal of Nuclear Science and Technology **2014**, *51* (7–8), 930–938.

[37] Hahn, D. W.; Omenetto, N. Laser-induced breakdown spectroscopy (LIBS), Part II: Review of instrumental and methodological approaches to material analysis and applications to different fields. *Applied Spectroscopy* **2012**, *66* (4), 347–419.

[38] Thorne, A.; Litzén, U.; Johansson, S. *Spectrophysics: Principles and Applications*; Springer Science & Business Media, 1999.

[39] Wu, S.; Wang, T.; Huang, C.; Gu, J.; Yu, L.; Xue, H.; Shen, Y. Advanced optical design of Czerny–Turner spectrometer with high flux and low aberration in broadband. *Applied Optics* **2022**, *61* (11), 3077.

[40] Huang, C.; Xia, G.; Jin, S.; Hu, M.; Wu, S.; Xing, J. Denoising analysis of compact CCD-based spectrometer. *Optik* **2017**, *157*, 693–706.

[41] Detalle, V.; Héon, R.; Sabsabi, M.; St-Onge, L. An evaluation of a commercial Échelle spectrometer with intensified charge-coupled device detector for materials analysis by laser-induced plasma spectroscopy.
Spectrochimica Acta Part B Atomic Spectroscopy **2001**,*56*(6),1011–1025.

[42] Hui, R. *Introduction to Fiber-Optic communications*; Academic Press, 2019.

[43] Janesick, J. R.; Elliott, T.; Collins, S.; Blouke, M. M.; Freeman, J. Scientific Charge-Coupled devices. *Optical Engineering* **1987**, *26* (8).

[44] Florek, S.; Haisch, C.; Okruss, M.; Becker-Ross, H. A new, versatile echelle spectrometer relevant to laser induced plasma applications.
Spectrochimica Acta Part B Atomic Spectroscopy **2001**, *56* (6), 1027–1034.

[45] Fossum, E. R. CMOS Image Sensors: Electronic Camera-on-a-chip. *IEEE Transactions on Electron Devices* **1997**, *44* (10), 1689–1698.

[46] Sabsabi, M.; Héon, R.; St-Onge, L. Critical evaluation of gated CCD detectors for laser-induced breakdown spectroscopy analysis.
Spectrochimica Acta Part B Atomic Spectroscopy **2005**, *60* (7–8), 1211–1216.

[47] Becker-Ross, H.; Florek, S. V. Echelle spectrometers and charge-coupled devices. *Spectrochimica Acta Part B Atomic Spectroscopy* **1997**, *52* (9–10), 1367–1375.

[48] Cremers, D. A.; Chinni, R. C. Laser-induced breakdown spectroscopy—capabilities and limitations. *Applied Spectroscopy Reviews* **2009**, *44* (6), 457–506.

[49] Fortes, F. J.; Moros, J.; Lucena, P.; Cabalín, L. M.; Laserna, J. J. Laser-induced breakdown spectroscopy. *Analytical Chemistry* **2012**, *85* (2), 640–669.

[50] St-Onge, L.; Detalle, V.; Sabsabi, M. Enhanced laser-induced breakdown spectroscopy using the combination of fourth-harmonic and fundamental Nd:YAG laser pulses. *Spectrochimica Acta Part B Atomic Spectroscopy* **2002**, *57* (1), 121–135.

[51] Galbács, G.; Budavári, V.; Geretovszky, Z. Multi-pulse laser-induced plasma spectroscopy using a single laser source and a compact spectrometer.
Journal of Analytical Atomic Spectrometry **2005**, *20* (9), 974.

[52] Jedlinszki, N.; Galbács, G. An evaluation of the analytical performance of collinear multi-pulse laser induced breakdown spectroscopy. *Microchemical Journal* **2010**, *97* (2), 255–263.

[53] Effenberger, A.; Scott, J. Effect of atmospheric conditions on LIBS spectra. *Sensors* **2010**, *10* (5), 4907–4925.

[54] Wang, Y.; Chen, A.; Sui, L.; Li, S.; Liu, D.; Wang, X.; Jiang, Y.; Huang, X.; Jin, M. Persistence of atomic spectral line on laser-induced Cu plasma with spatial confinement. *Physics of Plasmas* **2016**, *23* (11).

[55] Li, X.; Yang, Z.; Wu, J.; Wei, W.; Qiu, Y.; Jia, S.; Qiu, A. Spatial confinement in laser-induced breakdown spectroscopy. *Journal of Physics D Applied Physics* **2016**, *50* (1), 015203.

[56] Yin, H.; Hou, Z.; Yuan, T.; Wang, Z.; Ni, W.; Li, Z. Application of spatial confinement for gas analysis using laser-induced breakdown spectroscopy to improve signal stability. *Journal of Analytical Atomic Spectrometry* **2015**, *30* (4), 922–928.

[57] Hao, Z.; Guo, L.; Li, C.; Shen, M.; Zou, X.; Li, X.; Lu, Y.; Zeng, X. Correction: Sensitivity improvement in the detection of V and Mn elements in steel using laser-induced breakdown spectroscopy with ring-magnet confinement. *Journal of Analytical Atomic Spectrometry* **2020**, *35* (7), 1503.

[58] Zhou, W.; Li, K.; Li, X.; Qian, H.; Shao, J.; Fang, X.; Xie, P.; Liu, W. Development of a nanosecond discharge-enhanced laser plasma spectroscopy. *Optics Letters* **2011**, *36* (15), 2961.

[59] Vajtai, R. *Springer Handbook of Nanomaterials*; Springer, 2013.

[60] Kelly, K. L.; Coronado, E.; Zhao, L. L.; Schatz, G. C. The optical properties of metal nanoparticles: the influence of size, shape, and dielectric environment. *The Journal of Physical Chemistry B* **2002**, *107* (3), 668–677.

[61] Willets, K. A.; Van Duyne, R. P. Localized surface plasmon resonance spectroscopy and sensing. *Annual Review of Physical Chemistry* **2006**, *58* (1), 267–297.

[62] Alzoubi, F. Y.; Ahmad, A. A.; Aljarrah, I. A.; Migdadi, A. B.; Al-Bataineh, Q. M. Localize surface plasmon resonance of silver nanoparticles using Mie theory. *Journal of Materials Science Materials in Electronics* **2023**, *34* (32).

[63] Amendola, V.; Pilot, R.; Frasconi, M.; Maragò, O. M.; Iatì, M. A. Surface plasmon resonance in gold nanoparticles: a review. *Journal of Physics Condensed Matter* **2017**, *29* (20), 203002.

[64] Haus, J. W. *Fundamentals and applications of Nanophotonics*; Woodhead Publishing, 2016.

[65] Pelton, M.; Bryant, G. W. *Introduction to Metal-Nanoparticle Plasmonics*; Wiley, 2013.

[66] Palásti, D. J.; Albrycht, P.; Janovszky, P.; Paszkowska, K.; Geretovszky, Z.; Galbács, G. Nanoparticle enhanced laser induced breakdown spectroscopy of liquid samples by using modified surface-enhanced Raman scattering substrates. *Spectrochimica Acta Part B Atomic Spectroscopy* **2020**, *166*, 105793.

[67] Sultangaziyev, A.; Bukasov, R. Review: Applications of surface-enhanced fluorescence (SEF) spectroscopy in bio-detection and biosensing. *Sensing and Bio-Sensing Research* **2020**, *30*, 100382.

[68] De Giacomo, A.; Gaudiuso, R.; Koral, C.; Dell'Aglio, M.; De Pascale, O. Nanoparticle-enhanced laser-induced breakdown spectroscopy of metallic samples. *Analytical Chemistry* **2013**, *85* (21), 10180–10187.

[69] Davletshin, Y. R.; Kumaradas, J. C. The role of morphology and coupling of gold nanoparticles in optical breakdown during picosecond pulse exposures. *Beilstein Journal of Nanotechnology* **2016**, *7*, 869–880.

[70] Halas, N. J.; Lal, S.; Chang, W.-S.; Link, S.; Nordlander, P. Plasmons in strongly coupled metallic nanostructures. *Chemical Reviews* **2011**, *111* (6), 3913–3961.

[71] Jain, P. K.; El-Sayed, M. A. Plasmonic coupling in noble metal nanostructures. *Chemical Physics Letters* **2010**, *487* (4–6), 153–164.

[72] Dell'Aglio, M.; Alrifai, R.; De Giacomo, A. Nanoparticle enhanced laser induced breakdown spectroscopy (NELIBS), a first review. *Spectrochimica Acta Part B Atomic Spectroscopy* **2018**, *148*, 105–112.

[73] Kinnan, M. K.; Chumanov, G. Plasmon coupling in two-dimensional arrays of silver nanoparticles: II. Effect of the particle size and interparticle distance. *The Journal of Physical Chemistry C* **2010**, *114* (16), 7496–7501.

[74] Nordlander, P.; Oubre, C.; Prodan, E.; Li, K.; Stockman, M. I. Plasmon hybridization in nanoparticle dimers. *Nano Letters* **2004**, *4* (5), 899–903.

[75] De Giacomo, A.; Gaudiuso, R.; Koral, C.; Dell'Aglio, M.; De Pascale, O. Nanoparticle enhanced laser induced breakdown spectroscopy: Effect of nanoparticles deposited on sample surface on laser ablation and plasma emission. *Spectrochimica Acta Part B Atomic Spectroscopy* **2014**, *98*, 19–27.

[76] De Giacomo, A.; Dell'Aglio, M.; Gaudiuso, R.; Koral, C.; Valenza, G. Perspective on the use of nanoparticles to improve LIBS analytical performance: nanoparticle enhanced laser induced breakdown spectroscopy (NELIBS). *Journal of Analytical Atomic Spectrometry* **2016**, *31* (8), 1566–1573.

[77] Salajková, Z.; Gardette, V.; Kaiser, J.; Dell'Aglio, M.; De Giacomo, A. Effect of spherical gold nanoparticles size on nanoparticle enhanced laser induced breakdown spectroscopy. *Spectrochimica Acta Part B Atomic Spectroscopy* **2021**, *179*, 106105.

[78] Nordlander, P.; Prodan, E. Plasmon hybridization in nanoparticles near metallic surfaces. *Nano Letters* **2004**, *4* (11), 2209–2213.

[79] De Giacomo, A.; Koral, C.; Valenza, G.; Gaudiuso, R.; Dell'Aglio, M. Nanoparticle enhanced laser-induced breakdown spectroscopy for microdrop analysis at subppm level. *Analytical Chemistry* **2016**, *88* (10), 5251–5257.

[80] Ohta, T.; Ito, M.; Kotani, T.; Hattori, T. Emission enhancement of laser-induced breakdown spectroscopy by localized surface plasmon resonance for analyzing plant nutrients. *Applied Spectroscopy* **2009**, *63* (5), 555–558.

[81] Zhao, X.; Zhao, C.; Du, X.; Dong, D. Detecting and mapping harmful chemicals in fruit and vegetables using nanoparticle-enhanced laser-induced breakdown spectroscopy. *Scientific Reports* **2019**, *9* (1).

[82] Koral, C.; Dell'Aglio, M.; Gaudiuso, R.; Alrifai, R.; Torelli, M.; De Giacomo, A. Nanoparticle-enhanced laser induced breakdown spectroscopy for the noninvasive analysis of transparent samples and gemstones. *Talanta* **2018**, *182*, 253–258.

[83] Torrione, P.; Collins, L. M.; Morton, K. D. Multivariate analysis, chemometrics, and machine learning in laser spectroscopy. In *Elsevier eBooks*; **2014**; pp 125–164.

[84] Pretsch, E.; Wilkins, C. L. Use and abuse of chemometrics. *TrAC Trends in Analytical Chemistry* **2006**, *25* (11), 1045.

[85] Geladi, P. Chemometrics in spectroscopy. Part 1. Classical chemometrics. *Spectrochimica Acta Part B Atomic Spectroscopy* **2003**, *58* (5), 767–782.

[86] Defernez, M.; Kemsley, E. K. The use and misuse of chemometrics for treating classification problems. *TrAC Trends in Analytical Chemistry* **1997**, *16* (4), 216–221.

[87] Palleschi, V. *Chemometrics and Numerical Methods in LIBS*; John Wiley & Sons, 2022.

[88] Brunnbauer, L.; Gajarska, Z.; Lohninger, H.; Limbeck, A. A critical review of recent trends in sample classification using laser-induced breakdown spectroscopy (LIBS). *TrAC Trends in Analytical Chemistry* **2022**, *159*, 116859.

[89] Gornushkin, I. B.; Eagan, P. E.; Novikov, A. B.; Smith, B. W.; Winefordner, J. D. Automatic correction of continuum background in laser-induced breakdown and Raman spectrometry. *Applied Spectroscopy* **2003**, *57* (2), 197–207.

[90] Eilers, P. H. C. A perfect smoother. *Analytical Chemistry* **2003**, *75* (14), 3631–3636.

[91] Zorov, N. B.; Gorbatenko, A. A.; Labutin, T. A.; Popov, A. M. A review of normalization techniques in analytical atomic spectrometry with laser sampling: From single to multivariate correction. *Spectrochimica Acta Part B Atomic Spectroscopy* **2010**, *65* (8), 642–657.

[92] Guezenoc, J.; Gallet-Budynek, A.; Bousquet, B. Critical review and advices on spectral-based normalization methods for LIBS quantitative analysis. *Spectrochimica Acta Part B Atomic Spectroscopy* **2019**, *160*, 105688.

[93] Pořízka, P.; Klus, J.; Hrdlička, A.; Vrábel, J.; Škarková, P.; Prochazka, D.; Novotný, J.; Novotný, K.; Kaiser, J. Impact of laser-induced breakdown spectroscopy data normalization on multivariate classification accuracy. *Journal of Analytical Atomic Spectrometry* **2016**, *32* (2), 277–288.

[94] Varmuza, K.; Filzmoser, P. *Introduction to multivariate statistical analysis in Chemometrics*; CRC Press, **2010**.

[95] Brereton, R. G. *Applied Chemometrics for scientists*; John Wiley & Sons, 2007.

[96] Wehrens, R. *Chemometrics with R: Multivariate Data Analysis in the Natural and Life Sciences*; Springer, 2020.

[97] Pořízka, P.; Klus, J.; Képeš, E.; Prochazka, D.; Hahn, D. W.; Kaiser, J. On the utilization of principal component analysis in laser-induced breakdown spectroscopy data analysis, a review. *Spectrochimica Acta Part B Atomic Spectroscopy* **2018**, *148*, 65–82.

[98] Lohninger, H.; Ofner, J. Multisensor hyperspectral imaging as a versatile tool for image-based chemical structure determination. *Spectrosc. Eur.* **2014**, *26* (5), 6–10.

[99] Moncayo, S.; Manzoor, S.; Navarro-Villoslada, F.; Caceres, J. O. Evaluation of supervised chemometric methods for sample classification by laser induced breakdown spectroscopy. *Chemometrics and Intelligent Laboratory Systems* **2015**, *146*, 354–364.

[100] Breiman, L. Random Forests. *Machine Learning* **2001**, *45* (1), 5–32.

[101] Jolivet, L.; Leprince, M.; Moncayo, S.; Sorbier, L.; Lienemann, C. -p.; Motto-Ros, V. Review of the recent advances and applications of LIBS-based imaging. *Spectrochimica Acta Part B Atomic Spectroscopy* **2018**, *151*, 41–53.

[102] Limbeck, A.; Brunnbauer, L.; Lohninger, H.; Pořízka, P.; Modlitbová, P.; Kaiser, J.; Janovszky, P.; Kéri, A.; Galbács, G. Methodology and applications of elemental mapping by laser induced breakdown spectroscopy. *Analytica Chimica Acta* **2020**, *1147*, 72–98.

[103] Janovszky, P.; Kéri, A.; Palásti, D. J.; Brunnbauer, L.; Domoki, F.; Limbeck, A.; Galbács, G. Quantitative elemental mapping of biological tissues by laser-induced breakdown spectroscopy using matrix recognition. *Scientific Reports* **2023**, *13* (1), 10089.

[104] Modlitbová, P.; Pořízka, P.; Kaiser, J. Laser-induced breakdown spectroscopy as a promising tool in the elemental bioimaging of plant tissues. *TrAC Trends in Analytical Chemistry* **2019**, *122*, 115729.

[105] Reynaud, E.; Gauthier, C.; Perez, J. Nanophases in polymers. *Revue De Métallurgie* **1999**, *96* (2), 169–176.

[106] Fu, S.; Sun, Z.; Huang, P.; Li, Y.; Hu, N. Some basic aspects of polymer nanocomposites: A critical review. *Nano Materials Science* **2019**, *1* (1), 2–30.

[107] Darwish, M. S. A.; Mostafa, M. H.; Al-Harbi, L. M. Polymeric nanocomposites for environmental and industrial applications. *International Journal of Molecular Sciences* **2022**, *23* (3), 1023.

[108] Sarfraz, J.; Gulin-Sarfraz, T.; Nilsen-Nygaard, J.; Pettersen, M. K. Nanocomposites for food packaging applications: An overview. *Nanomaterials* **2020**, *11* (1), 10.

[109] Chowdhury, M. I. S.; Autul, Y. S.; Rahman, S.; Hoque, M. E. Polymer nanocomposites for automotive applications. In *Elsevier eBooks*; 2022; pp 267–317.

[110] Kumar, A.; Kumar, N. Advances in transparent polymer nanocomposites and their applications: A comprehensive review. *Polymer-Plastics Technology and Materials* **2022**, *61* (9), 937–974.

[111] Tajik, S.; Beitollahi, H.; Nejad, F. G.; Dourandish, Z.; Khalilzadeh, M. A.; Jang, H.; Venditti, R. A.; Varma, R. S.; Shokouhimehr, M. Recent developments in polymer nanocomposite-based electrochemical sensors for detecting environmental pollutants. *Industrial & Engineering Chemistry Research* **2021**, *60* (3), 1112–1136.

[112] Bi, Y.; Li, Z.; Wang, N.; Zhang, L. Preparation and characterization of UV/thermal dual-curable polyurethane acrylate adhesive for inertial confinement fusion experiment. *International Journal of Adhesion and Adhesives* **2015**, *66*, 9–14.

[113] Tosca, M.; Molloy, D.; McNamee, A.; Pleskunov, P.; Protsak, M.; Biliak, K.; Nikitin, D.; Kousal, J.; Krtouš, Z.; Hanyková, L.; Hanuš, J.; Biederman, H.; Foster, T.; Nersisyan, G.; Martin, P.; Ho, C.; Macková, A.; Mikšová, R.; Borghesi, M.; Kar, S.; Istokskaia, V.; Levy, Y.; Picciotto, A.; Giuffrida, L.; Margarone, D.; Choukourov, A. Plasma polymers as targets for laser-driven proton-boron fusion. *Frontiers in Physics* **2023**, *11*.

[114] Biró, T. S.; Kroó, N.; Csernai, L. P.; Veres, M.; Aladi, M.; Papp, I.; Kedves, M. Á.; Kámán, J.; Szokol, Á. N. N.; Holomb, R.; Rigó, I.; Bonyár, A.; Borók, A.; Zangana, S.; Kovács, R.; Tarpataki, N.; Csete, M.; Szenes, A.; Vass, D.; Tóth, E.; Galbács, G.; Szalóki, M. With Nanoplasmonics towards fusion. *Universe* **2023**, *9* (5), 233.

[115] Kroó, N.; Aladi, M.; Kedves, M.; Ráczkevi, B.; Kumari, A.; Rácz, P.; Veres, M.; Galbács, G.; Csernai, L. P.; Biró, T. S. Monitoring of nanoplasmonics-assisted deuterium production in a polymer seeded with resonant Au nanorods using in situ femtosecond laser induced breakdown spectroscopy. *Scientific Reports* **2024**, *14* (1), 18288.

[116] Bonyár, A.; Szalóki, M.; Borók, A.; Rigó, I.; Kámán, J.; Zangana, S.; Veres, M.; Rácz, P.; Aladi, M.; Kedves, M.; Szokol, Á.; Petrik, P.; Fogarassy, Z.; Molnár, K.; Csete, M.; Szenes, A.; Tóth, E.; Vas, D.; Papp, I.; Galbács, G.; Csernai, L.; Biró, T.; Kroó, N. The effect of femtosecond laser irradiation and plasmon field on the degree of conversion of a UDMA-TEGDMA copolymer nanocomposite doped with gold nanorods. *International Journal of Molecular Sciences* **2022**, *23* (21), 13575.

[117] Palásti, D. J.; Urbán, O.; Casian-Plaza, F. A.; Kámán, J.; Rigó, I.; Szalóki, M.; Bonyár, A.; Chinh, N. Q.; Galbács, Z.; Veres, M.; Galbács, G. Improving the mechanical, spectroscopic and laser ablation characteristics of UDMA-MMA copolymers using a titanocene photoinitiator. *Polymer Testing* **2024**, *139*, 108565.

[118] Vakhrushev, A. V.; Haghi, A. K. *Composite Materials Engineering: Modeling and Technology*; Apple Academic Press, 2021.

[119] Batool, M.; Haider, M. N.; Javed, T. Applications of spectroscopic techniques for characterization of polymer nanocomposite: a review.

Journal of Inorganic and Organometallic Polymers and Materials **2022**, *32* (12), 4478–4503.

[120] Palleschi, V. Avoiding misunderstanding self-absorption in laser-induced breakdown spectroscopy (LIBS) analysis. *Spectroscopy* **2022**, 60–62.

[121] Kanrar, B.; Sanyal, K.; Misra, N. L.; Aggarwal, S. K. Improvements in energy dispersive X-ray fluorescence detection limits with thin specimens deposited on thin transparent adhesive tape supports. *Spectrochimica Acta Part B Atomic Spectroscopy* **2014**, *101*, 130–133.

[122] Adams, F.; Vekemans, B.; Silversmit, G.; De Samber, B.; Vincze, L. Microscopic x-ray fluorescence analysis with synchrotron radiation sources. In *Handbook of Nuclear Chemistry*; 2011; pp 1737–1759.

[123] Cárdenas-Escudero, J.; Gardette, V.; Villalonga, A.; Sánchez, A.; Villalonga, R.; Motto-Ros, V.; Galán-Madruga, D.; Cáceres, J. O. A chemically functionalized glass support for gold and silver metallic nanoparticle analysis with LIBS. *Journal of Analytical Atomic Spectrometry* **2024**, *39* (3), 962–973.

[124] Modlitbová, P.; Farka, Z.; Pastucha, M.; Pořízka, P.; Novotný, K.; Skládal, P.; Kaiser, J. Laser-induced breakdown spectroscopy as a novel readout method for nanoparticle-based immunoassays. *Microchimica Acta* **2019**, *186* (9), 629.

[125] Mao, X.; Russo, R. E. Invited paper observation of plasma shielding by measuring transmitted and reflected laser pulse temporal profiles. *Applied Physics A* **1996**, *64* (1), 1–6.

[126] Rehman, Z. U.; Raza, A.; Qayyum, H.; Ullah, S.; Mahmood, S.; Qayyum, A. Characterization of laser-induced shock waves generated during infrared laser ablation of copper by the optical beam deflection method. *Applied Optics* **2022**, *61* (29), 8606.

[127] Wang, Y.; Liu, C.; Li, C. Evolution of ns pulsed laser induced shock wave on aluminum surface by numerical simulation. *Results in Physics* **2021**, *22*, 103920.

[128] Ravi-Kumar, S.; Lies, B.; Lyu, H.; Qin, H. Laser ablation of polymers: A review. *Procedia Manufacturing* **2019**, *34*, 316–327.

[129] Fardel, R.; Nagel, M.; Lippert, T.; Nüesch, F.; Wokaun, A.; Luk'yanchuk, B. S. Influence of thermal diffusion on the laser ablation of thin polymer films. *Applied Physics A* **2007**, *90* (4), 661–667.

[130] Lippert, T. Interaction of photons with polymers: From surface modification to ablation. *Plasma Processes and Polymers* **2005**, *2* (7), 525–546.

[131] Deegan, R. D.; Bakajin, O.; Dupont, T. F.; Huber, G.; Nagel, S. R.; Witten, T. A. Contact line deposits in an evaporating drop. *Physical Review. E, Statistical Physics, Plasmas, Fluids, and Related Interdisciplinary Topics* **2000**, *62* (1), 756–765.

[132] Deegan, R. D.; Bakajin, O.; Dupont, T. F.; Huber, G.; Nagel, S. R.; Witten, T. A. Capillary flow as the cause of ring stains from dried liquid drops. *Nature* **1997**, *389* (6653), 827–829.

[133] Limbeck, A.; Brunnbauer, L.; Lohninger, H.; Pořízka, P.; Modlitbová, P.; Kaiser, J.; Janovszky, P.; Kéri, A.; Galbács, G. Methodology and applications of elemental mapping by laser induced breakdown spectroscopy. *Analytica Chimica Acta* **2020**, *1147*, 72–98.

[134] Khedr, A. A.; Sliem, M. A.; Abdel-Harith, M. Gold nanoparticle-enhanced laser-induced breakdown spectroscopy and three-dimensional contour imaging of an aluminum alloy. *Applied Spectroscopy* **2020**, *75* (5), 565–573.

[135] Villy, L. P.; Kohut, A.; Kéri, A.; Bélteki, Á.; Radnóczi, G.; Fogarassy, Z.; Radnóczi, G. Z.; Galbács, G.; Geretovszky, Z. Continuous spark plasma synthesis of Au/Co binary nanoparticles with tunable properties. *Scientific Reports* **2022**, *12* (1), 18560.

[136] Kohut, A.; Villy, L. P.; Kéri, A.; Bélteki, Á.; Megyeri, D.; Hopp, B.; Galbács, G.; Geretovszky, Z. Full range tuning of the composition of Au/Ag binary nanoparticles by spark discharge generation. *Scientific Reports* **2021**, *11* (1), 5117.

[137] Bonyár, A.; Csarnovics, I.; Veres, M.; Himics, L.; Csik, A.; Kámán, J.; Balázs, L.; Kökényesi, S. Investigation of the performance of thermally generated gold nanoislands for LSPR and SERS applications. *Sensors and Actuators B Chemical* **2017**, *255*, 433–439.

[138] Rukosuyev, M. V.; Barannyk, O.; Oshkai, P.; Jun, M. B. G. Design and application of nanoparticle coating system with decoupled spray generation and deposition control. *Journal of Coatings Technology and Research* **2016**, *13* (5), 769–779.

[139] Serrano, A.; De La Fuente, O. R.; García, M. A. Extended and localized surface plasmons in annealed Au films on glass substrates. *Journal of Applied Physics* **2010**, *108* (7).

[140] Sherbini, A. M. E.; Parigger, C. G. Nano-material size dependent laser-plasma thresholds. *Spectrochimica Acta Part B Atomic Spectroscopy* **2016**, *124*, 79–81.

[141] Jain, P. K.; Lee, K. S.; El-Sayed, I. H.; El-Sayed, M. A. Calculated absorption and scattering properties of gold nanoparticles of different size, shape, and composition: applications in biological imaging and biomedicine. *The Journal of Physical Chemistry B* **2006**, *110* (14), 7238–7248.

[142] Keldysh, L. V. Ionization in the field of a strong electromagnetic wave. In *World Scientific eBooks*; 2023; pp 56–63.

[143] *3rd Raw Materials Scoreboard: European Innovation Partnership on Raw Materials*; Publications Office of the European Union, 2021.https://data.europa.eu/doi/10.2873/567799. (accessed 2025-12-08).

[144] Janovszky, P.; Jancsek, K.; Palásti, D. J.; Kopniczky, J.; Hopp, B.; Tóth, T. M.; Galbács, G. Classification of minerals and the assessment of lithium and beryllium content in granitoid rocks by laser-induced breakdown spectroscopy. *Journal of Analytical Atomic Spectrometry* **2021**, *36* (4), 813–823.

[145] Jancsek, K.; Janovszky, P.; Galbács, G.; Tóth, T. M. Granite alteration as the origin of high lithium content of groundwater in southeast Hungary. *Applied Geochemistry* **2023**, *149*, 105570.

[146] Brunnbauer, L.; Larisegger, S.; Lohninger, H.; Nelhiebel, M.; Limbeck, A. Spatially resolved polymer classification using laser induced breakdown spectroscopy (LIBS) and multivariate statistics. *Talanta* **2019**, *209*, 120572.

[147] El-Saeid, R. H.; Abdel-Salam, Z.; Pagnotta, S.; Palleschi, V.; Harith, M. A. Classification of sedimentary and igneous rocks by laser induced breakdown spectroscopy and nanoparticle-enhanced laser induced breakdown spectroscopy combined with principal component analysis and graph theory. *Spectrochimica Acta Part B Atomic Spectroscopy* **2019**, *158*, 105622.

[148] Kondak, S.; Janovszky, P.; Szőllősi, R.; Molnár, Á.; Oláh, D.; Adedokun, O. P.; Dimitrakopoulos, P. G.; Rónavári, A.; Kónya, Z.; Erdei, L.; Galbács, G.; Kolbert, Z. Nickel oxide nanoparticles induce cell wall modifications, root anatomical changes, and nitrosative signaling in ecotypes of Ni hyperaccumulator Odontarrhena lesbiaca. *Environmental Pollution* **2023**, *341*, 122874.

[149] Molnár, A.; Kondak, S.; Benkő, P.; Janovszky, P.; Kovács, K.; Szőllősi, R.; Gondor, O. K.; Oláh, D.; Gémes, K.; Galbács, G.; Janda, T.; Kolbert, Z. Limited Zn supply affects nutrient distribution, carbon metabolism and causes nitro-oxidative stress in sensitive Brassica napus. *Environmental and Experimental Botany* **2022**, *202*, 105032.

[150] Modlitbová, P.; Pořízka, P.; Střítežská, S.; Zezulka, Š.; Kummerová, M.; Novotný, K.; Kaiser, J. Detail investigation of toxicity, bioaccumulation, and translocation of Cd-based quantum dots and Cd salt in white mustard. *Chemosphere* **2020**, *251*, 126174.

[151] Noulas, C.; Tziouvalekas, M.; Karyotis, T. Zinc in soils, water and food crops. *Journal of Trace Elements in Medicine and Biology* **2018**, *49*, 252–260.

[152] Cabot, C.; Martos, S.; Llugany, M.; Gallego, B.; Tolrà, R.; Poschenrieder, C. A role for zinc in plant defense against pathogens and herbivores. *Frontiers in Plant Science* **2019**, *10*, 1171.

[153] Zeng, H.; Wu, H.; Yan, F.; Yi, K.; Zhu, Y. Molecular regulation of zinc deficiency responses in plants. *Journal of Plant Physiology* **2021**, *261*, 153419.

[154] Jantzi, S. C.; Motto-Ros, V.; Trichard, F.; Markushin, Y.; Melikechi, N.; De Giacomo, A. Sample treatment and preparation for laser-induced breakdown spectroscopy. *Spectrochimica Acta Part B Atomic Spectroscopy* **2015**, *115*, 52–63.

[155] Krajcarová, L.; Novotný, K.; Kummerová, M.; Dubová, J.; Gloser, V.; Kaiser, J. Mapping of the spatial distribution of silver nanoparticles in root tissues of Vicia faba by laser-induced breakdown spectroscopy (LIBS). *Talanta* **2017**, *173*, 28–35.

[156] Zhao, C.; Dong, D.; Du, X.; Zheng, W. In-Field, in situ, and in vivo 3-Dimensional elemental mapping for plant tissue and soil analysis using Laser-Induced Breakdown spectroscopy. *Sensors* **2016**, *16* (10), 1764.

[157] Szőllősi, R.; Molnár, Á.; Janovszky, P.; Kéri, A.; Galbács, G.; Dernovics, M.; Kolbert, Z. Selenate triggers diverse oxidative responses in Astragalus species with diverse selenium tolerance and hyperaccumulation capacity. *Plant Physiology and Biochemistry* **2023**, *202*, 107976.

[158] Gierenz, G.; Karmann, W. *Adhesives and adhesive tapes*; 2001.

[159] Daimon, T.; Kawai, K.; Kamoto, T. Use of a Technovit 7200 VLC to facilitate integrated determination of aluminum by light and electron microscopy. *Biotechnic & Histochemistry* **2000**, *75* (1), 27–32.

[160] *Technovit 7200*. Kulzer Technik. https://kulzer-technik.com/en-kt/en-kt/products/technovit-7200.html (accessed 2025-12-29).

[161] Zervas, M. N.; Codemard, C. A. High power fiber lasers: A review. *IEEE Journal of Selected Topics in Quantum Electronics* **2014**, *20* (5), 219–241.

[162] Nemova, G. Brief review of recent developments in fiber lasers. *Applied Sciences* **2024**, *14* (6), 2323.

[163] Zuo, J.; Lin, X. High-Power Laser Systems (Laser Photonics rev. 16(5)/2022). *Laser & Photonics Review* **2022**, *16* (5).

[164] Baudelet, M.; Willis, C. C. C.; Shah, L.; Richardson, M. Laser-induced breakdown spectroscopy of copper with a 2 μm thulium fiber laser. *Optics Express* **2010**, *18* (8), 7905.

[165] Zeng, Q.; Guo, L.; Li, X.; Shen, M.; Zhu, Y.; Li, J.; Yang, X.; Li, K.; Duan, J.; Zeng, X.; Lu, Y. Quantitative analyses of Mn, V, and Si elements in steels using a portable laser-induced breakdown spectroscopy system based on a fiber laser. *Journal of Analytical Atomic Spectrometry* **2016**, *31* (3), 767–772.

[166] Guo, L.-B.; Cheng, X.; Tang, Y.; Tang, S.-S.; Hao, Z.-Q.; Li, X.-Y.; Lu, Y.-F.; Zeng, X.-Y. Improvement of spectral intensity and resolution with fiber laser for on-stream slurry analysis in laser-induced breakdown spectroscopy. *Spectrochimica Acta Part B Atomic Spectroscopy* **2018**, *152*, 38–43.

[167] Xu, Z.; Xu, B.; Peng, X.; Qin, Y.; Yan, X.; Liao, X.; Zhang, N.; Lai, Q.; Li, J.; Zhang, Q. Laser-ablation dependence of fiber-laser-based laser-induced breakdown spectroscopy for determining Cu, Mg, and Mn elements in aluminum alloys. *Journal of Analytical Atomic Spectrometry* **2021**, *36* (11), 2501–2508.

[168] Riedel, J.; Hufgard, J.; You, Y. LIBS at high duty-cycles: effect of repetition rate and temporal width on the excitation laser pulses. *Frontiers in Physics* **2023**, *11*.

[169] Rizwan, M.; Afgan, M. S.; Saleem, S.; Kou, K.; Hou, Z.; Wang, Z. Double pulse laser-induced breakdown spectroscopy (DP-LIBS): A comprehensive technique review. *Spectrochimica Acta Part B Atomic Spectroscopy* **2025**, *227*, 107168.

[170] Aragón, C.; Aguilera, J. A. Characterization of laser induced plasmas by optical emission spectroscopy: A review of experiments and methods. *Spectrochimica Acta Part B Atomic Spectroscopy* **2008**, *63* (9), 893–916.

[171] Elnasharty, I. Y.; Doucet, F. R.; Gravel, J.-F. Y.; Bouchard, P.; Sabsabi, M. Double-pulse LIBS combining short and long nanosecond pulses in the microjoule range. *Journal of Analytical Atomic Spectrometry* **2014**, *29* (9), 1660–1666.

[172] Asamoah, E.; Hongbing, Y. Influence of laser energy on the electron temperature of a laser-induced Mg plasma. *Applied Physics B* **2016**, *123* (1).

[173] Yao, S.; Zhang, J.; Gao, X.; Zhao, S.; Lin, J. The effect of pulse energy on plasma characteristics of femtosecond filament assisted ablation of soil. *Optics Communications* **2018**, *425*, 152–156.

[174] Wang, L.; Tolok, G.; Fu, Y.; Xu, L.; Li, L.; Gao, H.; Zhou, Y. Application and research progress of laser-induced breakdown spectroscopy in agricultural product inspection. *ACS Omega* **2024**, *9* (23), 24203–24218.

[175] Sezer, B.; Bilge, G.; Boyaci, I. H. Capabilities and limitations of LIBS in food analysis. *TrAC Trends in Analytical Chemistry* **2017**, *97*, 345–353.

[176] Senesi, G. S.; Cabral, J.; Menegatti, C. R.; Marangoni, B.; Nicolodelli, G. Recent advances and future trends in LIBS applications to agricultural materials and their food derivatives: An overview of developments in the last decade (2010–2019). Part II. Crop plants and their food derivatives. *TrAC Trends in Analytical Chemistry* **2019**, *118*, 453–469.

[177] Markiewicz-Keszycka, M.; Cama-Moncunill, X.; Casado-Gavalda, M. P.; Dixit, Y.; Cama-Moncunill, R.; Cullen, P. J.; Sullivan, C. Laser-induced breakdown spectroscopy (LIBS) for food analysis: A review. *Trends in Food Science & Technology* **2017**, *65*, 80–93.

[178] Taiwo, A. M. A review of environmental and health effects of organochlorine pesticide residues in Africa. *Chemosphere* **2019**, *220*, 1126–1140.

[179] Ashesh, A.; Singh, S.; Devi, N. L.; Yadav, I. C. Organochlorine pesticides in multi-environmental matrices of India: A comprehensive review on characteristics, occurrence, and analytical methods. *Microchemical Journal* **2022**, *177*, 107306.

[180] Chandra, R.; Sharpanabharathi, N.; Prusty, B. A. K.; Azeez, P. A.; Kurakalva, R. M. Organochlorine pesticide residues in plants and their possible ecotoxicological and agri food impacts. *Scientific Reports* **2021**, *11* (1), 17841.

[181] Jayaraj, R.; Megha, P.; Sreedev, P. Review Article. Organochlorine pesticides, their toxic effects on living organisms and their fate in the environment. *Interdisciplinary Toxicology* **2016**, *9* (3–4), 90–100.

[182] Martyniuk, C. J.; Mehinto, A. C.; Denslow, N. D. Organochlorine pesticides: Agrochemicals with potent endocrine-disrupting properties in fish. *Molecular and Cellular Endocrinology* **2020**, *507*, 110764.

[183] Xu, Y.; Su, Y.; Cai, S.; Yao, Y.; Chen, X. Environmental and occupational exposure to organochlorine pesticides associated with Parkinson's disease risk: A systematic review and meta-analysis based on epidemiological evidence. *Public Health* **2024**, *237*, 374–386.

[184] Cestonaro, L. V.; Macedo, S. M. D.; Piton, Y. V.; Garcia, S. C.; Arbo, M. D. Toxic effects of pesticides on cellular and humoral immunity: an overview. *Immunopharmacology and Immunotoxicology* **2022**, *44* (6), 816–831.

[185] Keswani, C.; Dilnashin, H.; Birla, H.; Roy, P.; Tyagi, R. K.; Singh, D.; Rajput, V. D.; Minkina, T.; Singh, S. P. Global footprints of organochlorine pesticides: a pan-global survey. *Environmental Geochemistry and Health* **2021**, *44* (1), 149–177.

[186] Li, M.; Wang, R.; Su, C.; Li, J.; Wu, Z. Temporal trends of exposure to organochlorine pesticides in the United States: A population study from 2005 to 2016. *International Journal of Environmental Research and Public Health* **2022**, *19* (7), 3862.

[187] Munjanja, B. K.; Nomngongo, P. N.; Mketo, N. Organochlorine pesticides in vegetable oils: An overview of occurrence, toxicity, and chromatographic determination in the past twenty-two years (2000–2022). *Critical Reviews in Food Science and Nutrition* **2023**, *64* (28), 10204–10220.

[188] Leyva-Morales, J. B.; Cabrera, R.; De Jesús Bastidas-Bastidas, P.; Valenzuela-Quintanar, A. I.; Pérez-Camarillo, J. P.; González-Mendoza, V. M.; Perea-Domínguez, X. P.; Márquez-Pacheco, H.; Amillano-Cisneros, J. M.; Badilla-Medina, C. N.; Ontíveros-García, L. A.; Cruz-Acevedo, E. Validation and application of liquid chromatography coupled with tandem mass spectrometry method for the analysis of glyphosate, aminomethylphosphonic acid (AMPA), and glufosinate in soil. *Agriculture* **2023**, *13* (6), 1131.

[189] Wondimu, K. T.; Geletu, A. K. Residue analysis of selected organophosphorus and organochlorine pesticides in commercial tomato fruits by gas chromatography mass spectrometry. *Heliyon* **2023**, *9* (3), e14121.

[190] Beneito-Cambra, M.; Gilbert-López, B.; Moreno-González, D.; Bouza, M.; Franzke, J.; García-Reyes, J. F.; Molina-Díaz, A. Ambient (desorption/ionization) mass spectrometry methods for pesticide testing in food: A review. *Analytical Methods* **2020**, *12* (40), 4831–4852.

[191] Xu, L.; El-Aty, A. M. A.; Eun, J.-B.; Shim, J.-H.; Zhao, J.; Lei, X.; Gao, S.; She, Y.; Jin, F.; Wang, J.; Jin, M.; Hammock, B. D. Recent advances in rapid detection techniques for pesticide residue: A review. *Journal of Agricultural and Food Chemistry* **2022**, *70* (41), 13093–13117.

[192] Xu, M.-L.; Gao, Y.; Han, X. X.; Zhao, B. Detection of pesticide residues in food using surface-enhanced RAMAN spectroscopy: A review. *Journal of Agricultural and Food Chemistry* **2017**, *65* (32), 6719–6726.

[193] Kim, G.; Kwak, J.; Choi, J.; Park, K. Detection of nutrient elements and contamination by pesticides in spinach and rice samples using laser-induced breakdown spectroscopy (LIBS). *Journal of Agricultural and Food Chemistry* **2011**, *60* (3), 718–724.

[194] Ma, F.; Dong, D. A measurement method on pesticide residues of apple surface based on laser-induced breakdown spectroscopy. *Food Analytical Methods* **2014**, *7* (9), 1858–1865.

[195] Du, X.; Dong, D.; Zhao, X.; Jiao, L.; Han, P.; Lang, Y. Detection of pesticide residues on fruit surfaces using laser induced breakdown spectroscopy. *RSC Advances* **2015**, *5* (97), 79956–79963.

[196] Martino, L. J.; Angelo, C. a. D. Quantification of dimethoate and chlorpyrifos residues in green leafy vegetables by laser-induced breakdown spectroscopy. *Spectrochimica Acta Part B Atomic Spectroscopy* **2022**, *195*, 106485.

[197] Cabrera, L. C.; Di Piazza, G.; Dujardin, B.; Marchese, E.; Pastor, P. M. The 2022 European Union report on pesticide residues in food. *EFSA Journal* **2024**, *22* (4), e8753.

[198] Burrows, H. D.; L, M. C.; Santaballa, J. A.; Steenken, S. Reaction pathways and mechanisms of photodegradation of pesticides. *Journal of Photochemistry and Photobiology B Biology* **2002**, *67* (2), 71–108.

[199] Gupta, S.; Gajbhiye, V. T.; Gupta, R. K. Effect of light on the degradation of two neonicotinoids viz acetamiprid and thiacloprid in soil. *Bulletin of Environmental Contamination and Toxicology* **2008**, *81* (2), 185–189.

[200] Katagi, T. Photodegradation of pesticides on plant and soil surfaces. *Reviews of Environmental Contamination and Toxicology* **2004**, *182*, 1–78.

[201] L'Yvonnet, P.; Vial, G.; Sarda, X.; Duboisset, A.; Carbonnier, B.; Parinet, J.; Dubocq, F. Thermal degradation of pesticide active substances: Prioritisation list. *Food Chemistry Advances* **2023**, *2*, 100327.

[202] Asimellis, G.; Hamilton, S.; Giannoudakos, A.; Kompitsas, M. Controlled inert gas environment for enhanced chlorine and fluorine detection in the visible and near-infrared by laser-induced breakdown spectroscopy. *Spectrochimica Acta Part B Atomic Spectroscopy* **2005**, *60* (7–8), 1132–1139.

[203] Gaft, M.; Nagli, L.; Eliezer, N.; Groisman, Y.; Forni, O. Elemental analysis of halogens using molecular emission by laser-induced breakdown spectroscopy in air. *Spectrochimica Acta Part B Atomic Spectroscopy* **2014**, *98*, 39–47.

[204] Xu, F.; Ma, S.; Zhao, C.; Dong, D. Application of molecular emissions in laser-induced breakdown spectroscopy: A review. *Frontiers in Physics* **2022**, *10*.

[205] Ali, M. Y.; Sina, A. A. I.; Khandker, S. S.; Neesa, L.; Tanvir, E. M.; Kabir, A.; Khalil, M. I.; Gan, S. H. Nutritional composition and bioactive compounds in tomatoes and their impact on human health and disease: a review. *Foods* **2020**, *10* (1), 45.

[206] Ramesh, K.; Paul, V.; Pandey, R. Dynamics of mineral nutrients in tomato (Solanum lycopersicum L.) fruits during ripening: part II—off the plant. *Plant Physiology Reports* **2021**, *26* (2), 284–300.

[207] Chen, M.; Yuan, T.; Hou, Z.; Wang, Z.; Wang, Y. Effects of moisture content on coal analysis using laser-induced breakdown spectroscopy. *Spectrochimica Acta Part B Atomic Spectroscopy* **2015**, *112*, 23–33.

[208] Lang, J.; Barták, M.; Hájek, J.; Staňková, E.; Trnková, K. Effects of foliar application of a lambda-cyhalothrin insecticide on photosynthetic characteristics of a fodder plant Malva moschata. *Agronomy* **2024**, *14* (12), 2818.

[209] Svoboda, J.; Pech, P.; Heneberg, P. Low concentrations of acetamiprid, deltamethrin, and sulfoxaflor, three commonly used insecticides, adversely affect ant queen survival and egg laying. *Scientific Reports* **2023**, *13* (1), 14893.

[210] Wang, L.; Qin, Z.; Li, X.; Yang, J.; Xin, M. Persistence behavior of chlorpyrifos and biological toxicity mechanism to cucumbers under greenhouse conditions. *Ecotoxicology and Environmental Safety* **2022**, *242*, 113894.

[211] Rial-Otero, R.; Arias-Estévez, M.; López-Periago, E.; Cancho-Grande, B.; Simal-Gándara, J. Variation in concentrations of the fungicides tebuconazole and dichlofluanid following successive applications to greenhouse-grown lettuces. *Journal of Agricultural and Food Chemistry* **2005**, *53* (11), 4471–4475.

[212] Zhang, T.; Tang, H.; Li, H. Chemometrics in laser-induced breakdown spectroscopy. *Journal of Chemometrics* **2018**, *32* (11).

[213] Demircioğlu, A. Measuring the bias of incorrect application of feature selection when using cross-validation in radiomics. *Insights Into Imaging* **2021**, *12* (1), 172.

[214] Halabaku, E.; Bytyçi, E. Overfitting in machine learning: A comparative analysis of decision trees and random forests. *Intelligent Automation & Soft Computing* **2024**, *39* (6), 987–1006.

[215] Labory, J.; Njomgue-Fotso, E.; Bottini, S. Benchmarking feature selection and feature extraction methods to improve the performances of machine-learning algorithms for patient classification using metabolomics biomedical data. *Computational and Structural Biotechnology Journal* **2024**, *23*, 1274–1287.

[216] Kajner, G.; Galbács, G. Exploring the use of nanoporous glass substrates for the quantitative trace microanalysis of aqueous samples by surface-enhanced laser-induced breakdown spectroscopy. *Analytical Chemistry* **2025**, *97* (23), 12000–12004.

10. PUBLICATIONS

Journal publications forming the basis of the dissertation:

[P1] **Casian-Plaza, F. A.**; Janovszky, P. M.; Palásti, D. J.; Kohut, A.; Geretovszky, Zs.; Kopniczky, J.; Schubert, F.; Živković, S.; Galbács, Z.; Galbács, G. Comparison of three nanoparticle deposition techniques potentially applicable to elemental mapping by nanoparticle-enhanced laser-induced breakdown spectroscopy.
Applied Surface Science **2024**, *657*, 159844.

[P2] **Casian-Plaza, F. A.**; Palásti, D. J.; Schubert, F.; Galbács, G. Optimization of nanoparticle-enhanced laser-induced breakdown spectroscopy for the hyperspectral chemical mapping of solid samples. *Analytica Chimica Acta* **2024**, *1330*, 343269.

[P3] **Casian-Plaza, F. A.**; Urbán, O.; Bélteki, Á.; Aladi, M.; Kedves, M.; Bonyár, A.; Kopniczky, J.; Veres, M.; Galbács, G. Quantitative characterization of the lateral distribution of gold nanoparticles in polystyrene nanocomposite thin films by laser-induced breakdown spectroscopy elemental mapping.
Applied Surface Science **2025**, 700, 163276.

[P4] Palásti, D. J.; **Casian-Plaza, F.A.**; Bélteki, Á.; Kohut, A.; Makkos, L.; Galbács, G. Single-shot laser-induced breakdown spectroscopy using various duration pulses generated by a compact master oscillator power amplifier fiber laser.
Optics & Laser Technology **2025**, *192*, 114120.

[P5] Palásti, D. J.; **Casian-Plaza, F.A.**; Bélteki, Á.; Kohut, A.; Makkos, L.; B. Hopp; Galbács, G., Multi-pulse laser-induced breakdown spectroscopy signal enhancement using a MHz-repetition-rate pulsed fiber laser source.
Spectrochimica Acta Part B Atomic Spectroscopy **2026**, *submitted for publication*.

[P6] **Casian-Plaza, F.A.**; Bodó, B.; Palásti, D.; Lakatos, L.; Kolbert, Zs.; Galbács, G. Detection of organochlorine pesticide residues on tomato fruits by machine learning evaluation of laser-induced breakdown spectroscopy data.
Food Chemistry **2026**, *submitted for publication*.

Additional journal publications:

[P7] Palásti, D. J.; Urbán, O.; **Casian-Plaza, F. A.**; Kámán, J.; Rigó, I.; Szalóki, M.; Bonyár, A.; Chinh, N. Q.; Galbács, Z.; Veres, M.; Galbács, G. Improving the mechanical, spectroscopic and laser ablation characteristics of UDMA-MMA copolymers using a titanocene photoinitiator. *Polymer Testing* **2024**, *139*, 108565.

[P8] Palásti, D. J.; Villy, L.; Leits, B.; Kéri, A.; Kohut, A.; Bélteki, Á.; Kajner, G.; **Casian-Plaza, F.A.**; Kovács-Széles, É.; Ajtai, T.; Veres, M.; Geretovszky, Z.; Galbács, G. Detection and characterization of mono- and bimetallic nanoparticles produced by electrical discharge plasma generators using laser-induced breakdown spectroscopy. *Spectrochimica Acta Part B Atomic Spectroscopy* **2023**, *209*, 106804.

[P9] Jancsek, K.; **Casian-Plaza, F.A**.; Galbács, G.; Tóth, Tivadar M.; Laser-induced breakdown spectroscopy (LIBS) reveals lithium content in mórágy granite formation. *Geologica Carpathica* **2025**, *under revision.*

[P10] Kondak, S.; Kondak, D.; Bodor, T.; Fejes, G.; Rónavári, A; Kónya, Z.; Szőllősi, R.; Kukri, A.; Gyenesei, A.; Urbán, P; Kun, J.; Gracheva, M.; Solti, A.; Pál, M.; Szalai, G.; Domonkos, I.; Szögi, T.; **Casian-Plaza, F.A**.; Galbács, G.; Kolbert, Z. Size-dependent zinc delivery and nanozyme-mediated stress alleviation by ZnO nanoparticles in zinc deficient tomato.
Environmental Science & Technology **2026**, *submitted for publication*.

11. ACKNOWLEDGEMENTS

I would like to thank my supervisor, Prof. Dr. Galbács G., for opening me the doors of his research group and trusting my abilities and skills, which allowed me to acquire new ones and improve others in my scientific and professional field. I am grateful to him and admire his enormous potential and competitiveness as a person, and with his valuable help we were able to obtain satisfactory results throughout this journey. I also thank D.J. Palásti for his tremendous help in various areas, especially in LIBS experiments, from which I learned a great deal, and for his knowledge in chemometrics. Furthermore, I thank Á. Bélteki for his cleverness and immense technical and engineering support when needed, and for his great sense of humor.

I also thank all other members of our group, O. Urbán, Gy. Kajner, A.R. Rwegasira, B. Bodó and my former colleague P.M. Janovszky; for their ideas, help, suggestions, and excellent camaraderie.

On the other hand, I also thank other researchers and professors at our University, with whom we collaborated to carry out the projects leading to my dissertation. Specifically, I thank J. Kopniczky and B. Hopp for the skills I could acquire in the use of profilometry and SEM. I would like to thank Z. Kónya and Á. Kukovecz for allowing me the use of the magnetron sputtering instrument. I would also like to thank A. Kohut and Zs. Geretovszky for their collaborative work with the SDG. I also thank Cs. Janáky for the access to the spin-coater and A. Bonyár for his assistance in fabricating thin film nanocomposite samples.

I would also like to thank M. Tóth, F. Schubert, and K. Jancsek from the Department of Geology for their collaborative geological work and for providing me with access to their good optical microscopes. Additionally, I would like to thank S. Kondak and Zs. Kolbert for their cooperation on biological topics, and L. Makkos for providing access to the fiber laser source.

I especially thank the Secretariat of Science, Humanities, Technology and Innovation (SECIHTI) of the Mexican government for fully funding my doctoral studies throughout this period, a process which was not easy to apply for.

And last but not least, I am deeply grateful to my parents, family, and loved ones, despite the distance. Thank you for your honourable and unconditional support, demands, and advices, which enabled me to achieve professional and personal success.